REPUBLIC OF TURKIYE

YILDIZ TECHNICAL UNIVERSITY

GRADUATE SCHOOL OF SCIENCE AND ENGINEERING

DESIGN, SYNTHESIS AND CHARACTERIZATION OF FUNCTIONAL GLASS-CERAMIC COATINGS FOR ANTI-FOULING SURFACE APPLICATIONS

Sinan DALOĞLU

MASTER OF SCIENCE THESIS

Department of Metallurgical and Materials Engineering

Material Program

Supervisor

Assoc. Prof. Dr. Buğra ÇİÇEK

March, 2023

REPUBLIC OF TURKEY

YILDIZ TECHNICAL UNIVERSITY

GRADUATE SCHOOL OF SCIENCE AND ENGINEERING

DESIGN, SYNTHESIS AND CHARACTERIZATION OF FUNCTIONAL GLASS-CERAMIC COATINGS FOR ANTI-FOULING SURFACE APPLICATIONS

A thesis submitted by Sinan DALOĞLU in partial fulfillment of the requirements for the degree of MASTER OF SCIENCE is approved by the committee on 08.03.2023 in Department of Metallurgical and Materials Engineering, Material Program.

Assoc. Prof. Dr. Buğra ÇİÇEK
Yıldız Technical University
Advisor

Approved By the Examining Committee

Assoc. Prof. Dr. Buğra ÇİÇEK, Advisor
Yildiz Technical University _____

Assoc. Prof. Dr. Metin GENÇTEN
Yildiz Technical University _____

Assoc. Prof. Dr. Ergün KELEŞOĞLU
Turkish-German University _____

I hereby declare that I have obtained the required legal permissions during data collection and exploitation procedures, that I have made the in-text citations and cited the references properly, that I haven't falsified and/or fabricated research data and results of the study and that I have abided by the principles of the scientific research and ethics during my Thesis Study under the title of Design, Synthesis And Characterization of Functional Glass-Ceramic Coatings For Anti-Fouling Surface Applications supervised by my supervisor, Assoc. Prof. Dr. Buğra ÇİÇEK. In the case of a discovery of false statement, I am to acknowledge any legal consequence.

Sinan DALOĞLU

Dedicated to my family

and my friends

ACKNOWLEDGEMENTS

I would like to extend my heartfelt and eternal gratitude to my respected advisor, Assoc. Prof. Dr. Buğra ÇİÇEK, who re-motivated me when I had reached the point of giving up my profession and who always supported me throughout the project.

I will always remember with gratitude the support and friendship of my dear friend Nurullah ÇÖPOĞLU, PhD. Candidate, and I thank him for the guidance he provided me.

I would like to thank also to the valuable members of the Akcoat Advanced Chemical Coating Materials Co.'s Enamel Solutions Research & Developments Department, especially Mr. Tamer CENGİZ and Mr. Murat KAYA, for providing me with unique knowledge and experiences.

I would like to express my gratitude to all of my colleagues in the Advanced Ceramic Research Group and to our mentor, Dr. Oğuz KARAAHMET, who guided us towards the correct path.

Above all, I extend my gratitude to my beloved family and to my valued friends, who are as dear to me as family, for loving and supporting me through all circumstances.

Sinan DALOĞLU

TABLE OF CONTENTS

LIST OF SYMBOLS viii
LIST OF ABBREVIATIONS xi
LIST OF FIGURES xiii
LIST OF TABLES xvi
ABSTRACT xvii
ÖZET xix
1 INTRODUCTION 1
1.1 Literature Review 1
1.2 Objective of the Thesis....3
1.3 Hypothesis....3
2 BIOFOULING 5
2.1 Industrial Fouling 6
2.1.1 Chemical reaction fouling....6
2.1.2 Corrosion fouling 7
2.1.3 Ice-cold fouling: 7
2.1.4 Precipitation fouling 8
2.1.5 Particle fouling....9
2.2 Industrial Biofouling....10
2.2.1 Fluid Flow....10
2.2.2 Mass Transfer....14
2.2.3 Heat Transfer 19
2.3 Marine Biofouling 22
2.4 Conclusion....23
3 ANTIFOULING 24
3.1 Antifouling 24
3.2 Antifouling Methods' History....24
3.3 Modern Approaches....25
3.3.1 Heavy metals....25
3.3.2 Booster biocides approach....26
3.3.3 Foul release coatings 26
3.3.4 A biomimetics approach....27
4 GLASS-CERAMICS 29

4.1 Definition of Glass-Ceramics 29
4.2 Properties of Glass-Ceramics 30
4.3 Formation of Glass-Ceramics 31
4.3.1 Pressing 31
4.3.2 Casting 31
4.3.3 Spinning 31
4.3.4 Rolling 31
4.3.5 Float process 31
4.3.6 Direct forming or reforming of glass-ceramics 31
4.4 Application Areas of Glass-Ceramics 31
5 GLASS-CERAMIC COATINGS **34**
5.1 Glass-Ceramic Coating on Metal Substrates 34
5.2 Chemical Contents and Their Objectives of Glass-Ceramic Coatings 35
5.2.1 Fluxes 38
5.2.2 Refractories 38
5.2.3 Adhesion Agents 38
5.2.4 Opacifiers 40
5.2.5 Color Agents 40
5.3 Properties of Glass-Ceramic Coatings 40
5.3.1 Thermal Properties 40
5.3.2 Physical and Mechanical Properties 45
5.3.3 Chemical Properties 46
5.4 The Usage Areas of Glass-Ceramic Coatings 48
5.5 Application Methods 48
5.5.1 Spraying Method 48
5.5.2 Dipping Method 49
5.5.3 Electrophoresis Method 49
5.5.4 Flow Coating 49
5.5.5 Thermal Spray Method 50
EXPERIMENTAL PROCEDURE **52**
6.1 Materials 53
6.2 Precursor Glass Preparation 53
6.3 Precursor Glass's Characterization 53
6.3.1 Chemical Analysis 53
6.3.2 Crystalline Structure Analysis 54

6.3.3 Thermal Analysis 54
6.4 Preparation of the Glass-Ceramic Coated Samples 54
6.5 The Characterization of Glass-Ceramic Coatings 56
6.5.1 Microstructural Analysis 56
6.5.2 Crystalline Structure Analysis 56
6.5.3 Chemical Characterization 56
6.5.4 Thickness Measurement 56
6.5.5 Adhesion Capability Evaluation 57
6.5.6 Chemical Durability's Evaluation 57
6.5.7 Color Measurement 57
6.5.8 Gloss Measurement 57
6.5.9 Contact Angle and Surface Tension Analysis 58
6.6 The Evaluation of Glass-Ceramic Coating's Antifouling Performance 58
6.6.1 Microstructural Analysis after Antifouling test 59
6.6.2 Surface Cleaning Procedure after Antifouling Test 59
RESULTS & DISCUSSION **60**
7.1 The Results of Precursor Glass Characterization 60
7.1.1 XRF Analysis 60
7.1.2 XRD Analysis 61
7.1.3 Thermal Analysis 62
7.2 The Results of Glass-Ceramic Coating Characterization 69
7.2.1 Microstructural Analysis 69
7.2.2 Crystalline Structure Analysis 72
7.2.3 IR Analysis 76
7.2.4 Thickness Measurement 78
7.2.5 The Evaluation of the Adhesion Quality 79
7.2.6 The Evaluation of the Chemical Durability 79
7.2.7 Color Measurement 80
7.2.8 Gloss Measurement 80
7.2.9 Contact Angle and Surface Tension Measurement 81
7.3 The Evaluation of Antifouling Performance 82
7.3.1 The Result of Microstructural Analysis 87
7.4 Conclusions and Recommendation 104
REFERENCES **108**
PUBLICATIONS FROM THE THESIS **119**

LIST OF SYMBOLS

N_A	A is Diffusing through Fluid B
g	Accelaration of Gravity
atm	Atmospheric Pressure
at. %	Atomic Percent
A	Area
°C	Celcius Degree
cm	Centimeter
cm^2	Centimeter Square
cm^3	Centimeter Cube
C_A	Concentration of A at a Distance x
x	Dividing Wall's Thickness
E	Eddy Diffusion
ρ	Fluid Density
v	Fluid Velocity
μ	Fluid Viscosity
F	Friction Factor
GPa	Gigapascal
g	Gram
ΔH	Height Loss
K	Kelvin
Kg	Kilogram
kJ	Kilojoule

kV	Kilovoltage
L	Length
L	Lightness – Darkness in Color Values
α	Linear Thermal Expansion Coefficient
Mpa	Megapascal
m	Meter
m^3	Meter Cube
m^2	Meter Square
μm	Micrometer
μΩ	Microohms
mg	Miligram
ml	Mililiter
D	Molecular Diffusivity of A through B
N	Newton
Pa	Pascal
a	Redness – Greeness in Color Values
Re	Reynolds Number
sec	Second
R	Shear Stress
c	Specific Heat
T_n	Temperatures of Surfaces
P	Tensile Strength
λ	Thermal Conductivity Coefficient
K	Thermal Shock
Q	Transferred Heat

D	Tube Diameter
β	Volume Thermal Expansion Coefficient
wt%	Weight Percent
b	Yellowness – Blueness in Color Values

LIST OF ABBREVIATIONS

AF	Antifouling
DIN	Deutsche Institut für Normung
DTA	Differential Thermal Analysis
DSC	Diffrential Scanning Calorimetry
EDS	Energy-Dispersive X-Ray Spectroscopy
EN	European Norm
EPS	Extracellular Polymeric Screte
FRCs	Foul Release Coatings
IEI	International Enamellers xiaintenan
ISO	International Organization for Standardization
MBT	Monobutyltin
POESTA	Powder Electrostatic Application
RTU	Ready to Use
RT	Room Temperature
SEM	Scanning Electron Microscopy
SPC	Self-Polishing Copolymer
D65	Standard Illuminant
VEA	Vitreous Enamel Association
XRD	X-Ray Diffraction
XRF	X-Ray Fluorescence
TGA	Thermogravimetric Analysis
TG-DTA	Thermogravimetric – Differential Thermal Analysis
TBT	Tribuyltin

UK	United Kingdom
VOC	Volatile Organic Compound

LIST OF FIGURES

Figure 1.1 Illustration of the biofouling stages in the marine environment.....2

Figure 2.1 **a)**Biofouling in a tubular heat exchanger's plate, and **b)** Biofouling on a ship hull 6

Figure 2.3 Corrosion-creating oxides in a heat exchanger's tubes. 7

Figure 2.4 Products of polymers that are icing in a heat exchanger. 8

Figure 2.5 Salt precipitation in the heat exchanger's tubes. 9

Figure 2.6 Buildup of solid particles in a tubular heat exchanger's plate. 10

Figure 2.7 Illustration of the biofouling circuit.....11

Figure 2.8 Laminar flow's velocity profile in a tube.....12

Figure 2.9 Turbulent flow's velocity profile in a tube. 12

Figure 2.10 Demonstration of the forces acting on an attaching particle on a surface. 15

Figure 2.11 A theoretical curve of biofilm growth on a solid surface. 16

Figure 2.12 Growth curve with local operational circumstances adjusted. 17

Figure 2.13 The fluid velocity effect on biofilm thickness.....17

Figure 2.14 The result of removing microorganisms from a flowing stream. 18

Figure 2.15 The result of removing nutrients from a flowing stream. 18

Figure 2.16 The variation in biofilm mass on a surface under various nutrient concentrations. 19

Figure 2.17 The impact of temperature fluctuation on a biofilm's thickness of *Escherichia coli*.....20

Figure 2.18 Temperature dispersion along the surface of the fouled heat exchanger. 21

Figure 3.1 The illustration of the important antifouling generation with the timeline. 25

Figure 4.1 **a)** fully glass / amorphous structure, **b)** amorphous structure with nuclei, **c)** beginning crystallization in an amorphous structure, and **d)** devitrified amorphous structure.....29

Figure 4.2 The impact of temperature on crystal development and nucleation in glasses. 30

Figure 5.1 Ellingham Diagram.....39

Figure 5.2 Viscosity – Temperature curve for a theoretical glass.....44

Figure 5.3 Electrophoresis Coating Method. 49

Figure 5.4 Glass-Ceramic Powder Charging in Corona Discharge.....51

Figure 6.1 The flow chart of experimental process.....52

Figure 7.1 XRD analysis's result of precursor glasses. 62

Figure 7.2 The shape images of precursor glasses with additives at different theis characteristic temperatures. 63

Figure 7.3 Heating microscopy curve of samples. 65
Figure 7.4 The TG – DTA curves of TiBPG. 68
Figure 7.5 The TG – DTA curves of APG. 68
Figure 7.6 The TG – DTA curves of ARPG 69
Figure 7.7 Cross-sectional area of gTiBGCC. 70
Figure 7.8 Cross-sectional area of AGCC. 71
Figure 7.9 Cross-sectional area of ARGCC. 71
Figure 7.10 Crystalline analysis of TiBGCC. 72
Figure 7.11 Crystalline analysis of AGCC. 74
Figure 7.12 Crystalline analysis of ARGCC. 75
Figure 7.13 The FT-IR analysis result of TiBGCC. 76
Figure 7.14 The IR analysis result of AGCC 77
Figure 7.15 The IR analysis result of ARGCC. 78
Figure 7.16 The images taken from TiBGCC's surface before and after antifouling test, and after cleaning procedure. (ones on left are before antifouling test, ones on middle are after antifouling test, ones on right are after cleaning procedure.) 88
Figure 7.17 The surface on which the EDS analysis was performed before AF test. 89
Figure 7.18 The image showing areas where EDS analysis was performed after AF test. 90
Figure 7.19 The surface on which the EDS analysis was performed after cleaning procedure 91
Figure 7.20 EDS mapping analysis from TiBGCC's cross -sectional area before antifouling test., ... 92
Figure 7.21 EDS mapping analysis from TiBGCC's cross-sectional area after cleaning procedure 93
Figure 7.22 The images taken from AGCC's surface before and after antifouling test, and after cleaning procedure. (ones on left are before antifouling test, ones on middle are after antifouling test, ones on right are after cleaning procedure.) 93
Figure 7.23 The surface on which the EDS analysis was performed before AF test 94
Figure 7.24 The image showing areas where EDS analysis was performed after AF test 95
Figure 7.25 The surface on which the EDS analysis was performed after cleaning procedure 97
Figure 7.26 EDS mapping analysis from AGCC's cross-sectional area before antifouling test 98
Figure 7.27 EDS mapping analysis from AGCC's cross-sectional area after cleaning procedure. 98
Figure 7.28 The images taken from AGCC's surface before and after antifouling test, and after cleaning procedure. (ones on left are before antifouling test, ones on middle are after antifouling test, ones on right are after cleaning

procedure.)....99

Figure 7.29 The surface on which the EDS analysis was performed before AF test. 99

Figure 7.30 The image showing areas where EDS analysis was performed after AF test.... 101

Figure 7.31 The surface on which the EDS analysis was performed after cleaning procedure....102

Figure 7.32 EDS mapping analysis from ARGCC's cross-sectional area before antifouling test....103

Figure 7.33 EDS mapping analysis from ARGCC's cross-sectional area after cleaning procedure....104

LIST OF TABLES

Table 4.1 The list of some glass-ceramic systems, and main crystals, properties, and application areas of them.....32

Table 5.1 The functions of minerals and oxides, used in glass-ceramic coatings.....35

Table 5.2 The classification of oxides in the glass structure according to their functions.....37

Table 5.3 Cubical thermal expansion coefficients of some glass-ceramic coatings and some metals.....41

Table 6.1 The table of milling formula, contents' ratio in % weight, milling time, and size of milled intermediate product of coating.....55

Table 7.1 The XRF analysis results of TiBPG, APG, ARPG. 60

Table 7.2 The Cubical Thermal Expansion Coefficient of steel substrate and glass – ceramic coatings.....66

Table 7.3 Coating thicknesses of TiBGCC, AGCC, and ARGCC.....78

Table 7.4 The results of adhesion evaluations of TiBGCC, AGCC, and ARGCC. 79

Table 7.5 The resistance performance of TiBGCC, AGCC, and ARGCC against to cold citric acid.....80

Table 7.6 The color values of glass-ceramic coatings. 80

Table 7.7 Gloss measurement of glass-ceramic coating.....81

Table 7.8 Contact angle and surface tension values of glass-ceramic coatings. 81

Table 7.9 Barnacle attachment ratio in numerical on the glass-ceramic coatings' surfaces.....85

Table 7.10 The result of EDS analysis the surface given in **Fig. 7.17** 89

Table 7.11 The results of EDS analysis of Area-1 and Area-2 given in **Fig. 7.18**.....90

Table 7.12 The result of EDS analysis the cleaned surface given in **Fig. 7.19.**.....91

Table 7.13 The result of EDS analysis the before AF test given in **Fig 7.23**. 94

Table 7.14 The results of EDS analysis of Area-1 and Area-2 given in **Fig. 7.24**.....96

Table 7.15 The result of EDS analysis the cleaned surface given in **Fig. 7.25**.....97

Table 7.16 The result of EDS analysis the before AF test given in **Fig 7.29**. 100

Table 7.17 The results of EDS analysis of Area-1 and Area-2 given in **Fig. 7.30**.....101

Table 7.18 The result of EDS analysis the cleaned surface given in **Fig. 7.31**.....102

ABSTRACT

Design, Synthesis and Characterization of Functional Glass-Ceramic Coatings For Anti-Fouling Surface Applications

Sinan DALOĞLU

Department of Metallurgical and Materials Engineering

Master of Science Thesis

Supervisor: Assoc. Prof. Dr. Buğra ÇİÇEK

The problem of biological fouling on surfaces exposed to fluid flow has been a significant issue in industrial water treatment and navigation since the development of these technologies. Biofouling, the accumulation of microorganisms on surfaces, can have negative effects on engineering properties and energy efficiency. Factors that affect biofouling include fluid-substrate interactions, fluid flow velocity, microorganism content, nutrient levels, temperature, and solar radiation intensity. While industrial surfaces are primarily affected by fluid velocity, nutrient and organism ratios, temperature, and marine surfaces also consider factors such as solar radiation, depth, organism species, and density. Many systems have been employed to protect surfaces, but these often involve the use of toxic chemicals, which can have harmful effects on the environment and human safety.

Biofouling is generally categorized into four stages: the formation of a conditioning layer by adherence of organic compounds, the adherence of primary colonizers (bacteria, yeasts, and diatoms), the secondary colonizers (protozoa, fungi, and macroalgae), and ternary colonizers (invertebrate larvaes). However, depending on the situation, this process may not always occur in order.

This study aimed to design and evaluate an environmentally friendly glass-ceramic coating as an alternative to traditional antifouling coatings or paints, which can cause harm to marine, river and lake environments and affect human safety. In this study, a TiO2-based precursor glass (TiBPG), an adhesive coat precursor glass (APG), and an alkaline resistant precursor glass (ARPG) were evaluated for their antifouling properties as glass-ceramic coatings. The precursor glass batches were melted at 1350 °C for 45 min before being quenched and were applied using a wet spray application method. The coatings were analyzed using various techniques, including XRF, XRD, heating microscopy, TG-DTA, and dilatometric analyses. The surfaces were also evaluated for structural phase, color, gloss, acid resistance, impact resistance, contact angle, and surface tension properties.

In addition, the coatings were tested using a rapid antifouling method and characterized before and after the test using SEM and EDS. The results showed that the TiBGCC and AGCC had a lower density of barnacles compared to the negative reference and the ARGCC. The barnacle density was calculated for each coating, with the TiBGCC showing a density of 73.9 barnacles/cm^2, the AGCC showing 68.9 barnacles/cm^2, and the ARGCC showing 88.7 barnacles/cm^2. The deviation between the replicates of the panels was found to be negligible, indicating that the outcome was evaluable. Overall, the results showed that the TiBGCC coating has superior antifouling properties compared to the other coatings evaluated.

This study found that these coatings have strong potential as an environmentally friendly and long-service life antifouling solution. However, further research is needed to optimize the coatings for different industrial applications and marine ecosystems. Future studies should also focus on the long-term effectiveness of these coatings, and explore other types of antifouling coatings that incorporate glass-ceramic materials. Overall, this study provides a starting point for the development of more efficient solutions for preventing biofouling.

Keywords: marine biofouling, industrial biofouling, antifouling coating, environmentally friendly coatings , glass-ceramic coating

ÖZET

Kirlenme Önleyici Yüzey Uygulamaları İçin Fonksiyonel Cam-Seramik Kaplamaların Tasarımı, Sentezi ve Karakterizasyonu

Sinan DALOĞLU

Metalurji ve Malzeme Mühendisliği Departmanı

Yüksek Lisans Tezi

Danışman: Doç. Dr. Buğra ÇİÇEK

Bir akış hızına sahip sıvı ile temasta olan yüzeylerdeki biyolojik kirlenme, endüstriyel su arıtma ve deniz taşımacılığında önemli bir sorun olmuştur. Biyokirlenme, yüzeylerde mikroorganizmaların birikmesi, mühendislik özellikleri ve enerji verimliliği üzerinde olumsuz etkilere sahiptir. Biyokirlenmeyi etkileyen faktörler arasında sıvı-substrat etkileşimleri, sıvı akış hızı, mikroorganizma içeriği, besin seviyeleri, sıcaklık ve güneş radyasyonu yoğunluğu yer almaktadır. Endüstriyel yüzeyler öncelikle sıvı hızı, sıvının sağladığı besin, sıvını taşıdığı organizma oranları ve sıcaklıktan etkilenmektedir. İkincil etkiler ise güneş radyasyonu, derinlik ve organizma tür çeşitliliğidir. Yüzeyleri korumak için birçok yöntem kullanılmıştır, ancak bunlar genellikle çevre ve insan güvenliği üzerinde zararlı etkileri olabilecek toksik kimyasalların kullanımını içermektedir.

Biyolojik kirlenme genel olarak dört aşamaya ayrılır: bileşiklerin tutunmasıyla bir koşullandırma tabakasının oluşumu, birincil kolonizörlerin (bakteriler, mayalar ve diyatomlar), ikincil kolonizörlerin (protozoa, mantarlar ve makroalgler) ve üçlü kolonizörlerin (omurgasız larvalar) yapışması. Ancak bazı koşullarda süreç her zaman bu sıra ile gerçekleşmemektedir.

Bu çalışma, deniz, nehir ve göl ortamlarına zarar verebilen ve insan güvenliğini etkileyebilen geleneksel antifouling kaplama veya boyalara alternatif olarak çevre dostu

bir cam-seramik kaplama tasarlamayı ve değerlendirmeyi amaçlamıştır. Bu çalışmada, cam-seramik kaplamalar olarak TiO2 bazlı (TiBPG), astar kaplama (APG) ve alkali dirençli (ARPG) kirlenme önleyici özellikleri açısından değerlendirilmiştir. Fritler, suya dökülme işlemi öncesinde 1350 °C'de 45 dakika ergitilmiştir ve sulu sprey uygulama yöntemi kullanılarak kaplanmıştır. Kaplamalar, XRF, XRD, ısı mikroskobu, TG-DTA ve dilatometrik analizler dahil olmak üzere çeşitli teknikler kullanılarak analiz edilmiştir. Yüzeyler ayrıca yapısal faz, renk, parlaklık, asit direnci, darbe direnci, temas açısı ve yüzey gerilimi özellikleri açısından değerlendirilmiştir.

Ek olarak, kaplamalar hızlı bir zehirli boya yöntemi kullanılarak test edilmiştir ve testten önce ve sonra SEM ve EDS kullanılarak karakterize edilmiştir. Sonuçlar, TiBGCC ve AGCC'nin, negatif referans ve ARGCC'ye kıyasla daha düşük midye yoğunluğuna sahip olduğunu göstermiştir. Midye yoğunluğu her kaplama için hesaplanmıştır; TiBGCC 73.9 midye/cm^2, AGCC 68.9 midye/cm2 ve ARGCC 88.7 midye/cm2 yoğunluk göstermiştir. Genel olarak sonuçlar, TiBGCC kaplamanın, değerlendirilen diğer kaplamalara kıyasla üstün kirlenme önleyici özelliklere sahip olduğunu göstermiştir.

Bu çalışma, bu kaplamaların çevre dostu ve uzun ömürlü çürüme önleyici bir çözüm olarak güçlü bir potansiyele sahip olduğunu bulmuştur. Ancak, farklı endüstriyel uygulamalar ve deniz ekosistemleri için kaplamaları optimize etmek için daha fazla araştırmaya ihtiyaç vardır. Gelecekteki çalışmalar ayrıca bu kaplamaların uzun vadeli etkinliğine odaklanmalı ve cam-seramik malzemeleri içeren diğer çürüme önleyici kaplama türlerini keşfetmelidir. Genel olarak, bu çalışma biyolojik kirlenmeyi önlemek için daha verimli çözümlerin geliştirilmesi için bir başlangıç noktası sağlamaktadır

Anahtar Kelimeler: deniz biyolojik kirlenmesi, endüstriyel biyolojik kirlenme, kirlenme önleyici (zehirli) kaplamalar, çevre dostu kaplamalar, cam-seramik kaplamalar.

1
INTRODUCTION

1.1 Literature Review

With beginning of the navigation and subsequently development of industrial water treatment applications, biological fouling has been a vital problem for all surfaces which exposed to fluid flow due to its negative effects on engineering properties, in particularly energy efficiency. Biofouling ratio is affected by fluid-substrate interactions, fluid flow velocity, the microorganisms content of fluid, the nutrients abundance of fluid, the temperature, the solar radiation intensity. Whilst the factors of biofouling observed in industrial surfaces are limited with fluid velocity, nutrient and organism ratios carried by fluid and temperature, the marine biofouling also affected by more factors such as solar radiation, depth, organism species variety and density, etc. Flow fluid contact surfaces require to be protected for the aims of low energy consumption with high service-life. There are many different systems has been employed, generally based on toxic release to fluid, such as chlorine in industrial applications and orgonatin and its derivative in marine applications. However, the utilization of these components have been prohibited because of their hazardous effects on marine, river, lakes environmental, subsequently on human safety through food chain. Also, developed new methods are under constant surveillance by governments or local governments due to possibility of their harmful impacts on the environment.

Biofouling is generally categorized in 4 consecutive stages, given in **Fig.1.1**:

- Occurrence of conditioning layer by adherence of organic compounds, (lipids, proteins, etc.),
- Adherence of primary colonizers, including bacteria, yeasts, and diatoms, subsequently occurrence of biofilm.
- Secondary colonizers, comprising the spores of protozoa, fungi, and macroalgae,
- Ternary colonizers, intervebrate larvaes.

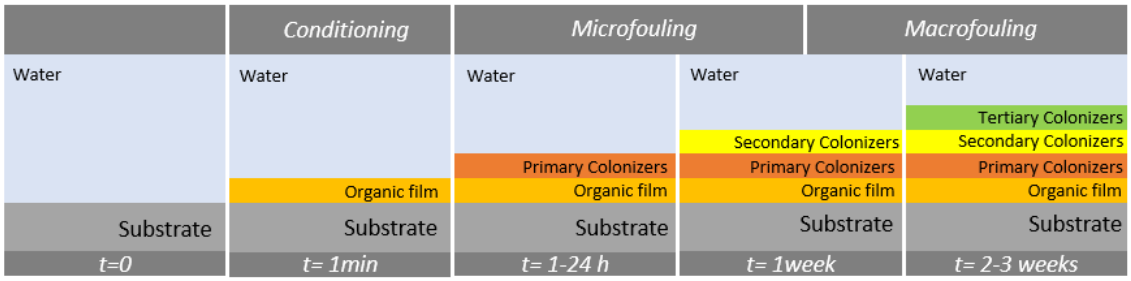


Figure 1.1 Illustration of the biofouling stages in the marine environment.

However, depending on the situation, this defined biofouling procedure might not take place in order. For instance, macropollutants will act more aggressively to attach to the surface in surroundings with few or no solid substrates and will do so without waiting for the establishment of biofilms.

The literature has been researched for the presence of utilization the glass, the ceramic, and the glass-ceramics in antifouling coating applications. In order to create a protective ceramic layer against fly ashes, Nguyen et al. [1] sintered a ternary glass (K_2O-Al_2O_3-SiO_2) with minor oxide concentrations at 800 °C for 24 hours over a steel substrate. For three months, it was planned to examine the variations in electrical conductivity between boilers with and without ceramic coating. The findings of this study showed that ceramic coated surfaces had superior electric conductivity than non-coated surfaces by over 100%, resulting in greater energy efficiency due to their anti-fouling protection against industrial dust. In an other study by Wang et al. [2], 15CrMo steel was coated with a composite ceramic coating that was made of ultrafine hexagonal boron nitride and graphite powders. The coating was applied at 550 °C for 6 hours. The goal of this study was to evaluate the antifouling capabilities of ceramic coatings against coal with a high-sodium content that fouls heat exchangers. The results showed that after five fouling cycles, the ceramic coated surface had indicated 0% fouling whereas the non-coated surface had revealed 21.9% fouling.

Glass-ceramic coatings are comprehend 5 main stages

- Formulation and batch preparation,
- Vitrification, including the melting and quenching processes,
- Powder preparation, including milling and sieving,
- Application,
- Devitrification, including the heat-treatment.

Glass-ceramic coatings are consists of glass-former, modifier, stabilizer, and promoter, see **Table 5.2**. These coatings have a wide utilization in engineering products such as kitchen utensils, pipelines, home appliances, boilers because of their superior properties of chemical resistance, mechanical strength, and thermal durability.

In this study, a TiO_2-based precursor glass (TiBPG), an adhesive coat precursor glass (APG), and alkaline resistant precursor glass (ARPG) were designed to evaluate in terms of antifouling performances of the glass-ceramic coatings. The raw materials of precursor glasses and additives were supplied from Akcoat Advanced Chemical Coating Materials Co. The batches of designed formulas were melted at 1350 ℃ for 45 min, subsequently quenched. Whilst the TiBPG was obtained by 2 coat – 2 fire methodology, the AGCC and ARGCC was obtained by 1 coat – 1 fire methodology. All precursor glasses were applied by wet spray application. Before application, produced precursor glasses were milled with additives and sieved. The AGCC also used for ground coat of TiBGCC to provide superior adhesion property. The ground coat was devitrified at 860 °C for 6 min, then cooled to room temperature. Following, TiBPG was applied on ground coat and pre-heated at 550 ℃ for 6 min and devitrified at 860 ℃ for 6 min, in respectively. Also, APG and ARPG were fired at 550 ℃ and subsequently crystallized at 860 ℃ for 6 min. Produced precursor glasses were analyzed by utilizing XRF, XRD, heating microscopy, TG-DTA, and dilatometric analyses. The obtained surfaces were further anaylzed in terms of structural phase, color, gloss, acid resistance, impact resistance, contact angle and surface tension properties. Glass-ceramic coatings were further tested with a rapid antifouling method and they were characterized before and after antifouling test by using SEM, EDS.

1.2 Objective of the Thesis

Useage of antifouling coatings or paints to provide a protection against biofouling creates hazardous damage to the marine, river and lack environment and subsequently affects the human safety. This thesis aims to create an alternative antifouling coating with environmental friendly behavior by designing a glass-ceramic coating.

1.3 Hypothesis

This study provides a significant contrubition to the literature as it serves as the basis for being inorganic coating attempts in terms of protection against to biological fouling. Also, in this thesis, the common points of biological fouling's occurrence process

between industrial and marine environments were discussed. Our hypothesis is that glass-ceramic coating systems could be employed and developed against biological contamination owing to their superior properies, especially relatively non-stick, chemical durability, long service-life and environmental friendly. Designed precursor glass and glass-ceramic coating will be examined for engineering performances and it will be evaluated whether it shows antifouling behavior.

2
BIOFOULING

Biofouling is an undesired accumulation process of biological matter on the water-contact surfaces, which comprises two key growth stages. The first stage is generally explained as thecreation of a biofilm matrix phenomenon by an initial buildup of organic adsorption, the settlement, and progress of adsorbation bacteria, and the second stage could be defined as the following succession of microfoulers and macrofoulers accumulation. It causes deterioration in the performance of submerged man-made structures, especially if the liquid is moving through the surface. Biofouling, therefore, is one of the biggest concerns in various areas ranging from industrial equipment (**Fig. 2.1.a**) to marine equipment (**Fig. 2.1.b.**). Whilst the deterioration in marine biofouling is related to issues such as fuel consumption and maneuverability, the deterioration in industrial biofouling is related to energy consumption. Therefore, a means of protection method from biological foulants capable of similar expanding and contracting properties is required for these man-made surfaces. Protective organic coatings are frequently utilized because of their wide variety of benefits, including corrosion resistance, simplicity of 5aintenancee, aesthetics, non-slip surfaces for decking, and the avoidance of undesired marine organisms from fouling the hull. This chapter aims to perceive the factors that either directly or indirectly influence the biofouling process in both marine and industrial environments.



Figure 2.1 a) Biofouling in a tubular heat exchanger's plate, and **b)** Biofouling on a ship hull.

2.1 Industrial Fouling

Any undesired organic or inorganic buildup on an engineered surface, which is in contact with a fluid, can be described as fouling. There are numerous distinct factors that might lead to fouling, which is often categorized as follows, in industrial operations [3], [4]:

2.1.1 Chemical reaction fouling

Chemical reaction fouling particularly observed in petroleum industries where refining processes trigger the polymerization of unsaturated hydrocarbons (**Fig. 2.2)**, could begin with the contact of two chemicals in a heat transfer process [5].



Figure 2.2 Hydrocarbon residue in a heat exchanger's tubes.

2.1.2 Corrosion fouling

This kind of fouling happens when a surface in contact with a fluid corrodes electrochemically or through microbial growth **(Fig. 2.3).** In order to understand more about the thermal resistance linked to corrosion-caused fouling, corrosion must be taken into account while designing heat exchangers [6], [7].



Figure 2.3 Corrosion-creating oxides in a heat exchanger's tubes.

2.1.3 Ice-cold fouling:

It is the buildup of solid deposits on a cooled surface as a result of a fluid or one of its components solidifying (**Fig. 2.4**). This sort of fouling builds up depending on the temperature of the surface and the shearing action of the fluid on the surface creates as a function of its circulation velocity. This effect is observed when the wax solidifies on a heat exchange surface in a hydrocarbon solution despite its high melting point [8], [9].



Figure 2.4 Products of polymers that are icing in a heat exchanger.

2.1.4 Precipitation fouling

The precipitation or scaling of dissolved compounds on the surfaces is the cause of this kind of fouling (**Fig. 2.5**). Aqueous solutions often precipitate dependent on their temperature and the solubility of dissolved materials. For example, calcium carbonate ($CaCO_3$) precipitates on a superheated surface when the water it contains evaporates.

The salts that have been dissolved in the water begin to precipitate when they come into contact with the heated tube's wall and experience supersaturation. Depending on their intensity, deposits that have clung to the surface may have varying degrees of hardness. As a result, the deposit is hard and very tenacious when it is made entirely of salts. On the other hand, if the deposit is made up mostly of suspended particles, it has a low hardness and poor adhesion.



Figure 2.5 Salt precipitation in the heat exchanger's tubes.

The most common precipitates can be given as calcium carbonate ($CaCO_3$), calcium sulfate ($CaSO_4$), calcium oxalate (CaC_2O_4), barium sulfate ($BaSO_4$), magnesium hydroxide ($Mg(OH)_2$), silicates ($(SiO_{4-x})_n$ where $0 \leq x < 2$), aluminum oxide (Al_2O_3), aluminum silicate (Al_2SiO_5), copper (Cu), phosphates (PO_4^{3-}), magnetite (Fe_3O_4) [5], [10], [11].

2.1.5 Particle fouling

The buildup of solid particles that are suspended in a fluid is what it is (liquid or gas). Several techniques, some of which are strongly related to characteristics of particles like aggregation, are used to deposit the particles on surfaces. The size, type, and environmental conditions of the particles, as well as the amount of deposit and the pace of deposition on the surfaces, all influence these factors. Fouling is referred to as sedimentation when gravity is the primary mechanism for depositing suspended particles on a surface [11], [12] (**Fig. 2.6**).



Figure 2.6 Buildup of solid particles in a tubular heat exchanger's plate.

2.2 Industrial Biofouling

Fluid flow, mass, and heat transfer have a great effect on the colonization of the microorganism to the surface of industrial equipment, subsequently growth. Understanding the relationship between these terms and biofouling in the industrial process helps to better understand how they affect industrial process efficiency and how to overcome these issues [13], [14].

2.2.1 Fluid Flow

In industrial biofilm occurrence generally arises from a fluid carrying microbial content, flowing across the surface. The flow level of the liquid, the liquid's physical characteristics, and the type of solid surface that will be colonized might all be cited as influences on deposition [14]. Reynolds (1883) systematically studied the relationship between these terms and his studies relate the fluid flow design and operation process dependent on the movement of liquids.

Flow conditions could be given as laminar flow and turbulent flow. Whilst, laminar flow, also called streamline flow, is observed at low velocities, turbulent flow is observed at higher velocities. Laminar flow goes parallel to the solid surface. While turbulent flow moves parallel to the surface for the close region to surface, this movement is random for remote region of [14], [15].

There is a friction between the surface and the fluid, and it causes a resistance to flow. Therefore, it may be considered that the liquid layers in connection with the surface is immobile. The fluid movement will generate a drag force at the solid surface. As the distance from the contact layer between the solid surface and fluid increases, fluid flow velocity will rise. An immobile layer at the fluid/surface interface and a slow-moving layer at the surface will always exist, even in case of turbulent circumstances. The "laminar sub-layer" or "viscous sub-layer" are terms that are frequently used to describe the slow-moving fluid area near to a solid wall [16]. In a tube, the bulk velocity in the tube will affect how thick the viscous sub-layer is. The laminar sub-layer is typically thinner the greater the bulk velocity. As might be predicted, there is a transition area between two flow types, turbulent and streamline. As could be predicted, there is a change area between two flow types, streamline and turbulent. The "boundary layer" is the term used to describe the gradual shift in flow ratio between the viscous sub-layer and turbulent zone [17]. The condition is shown in Fig. 2.7, which also graphically depicts microorganisms' deposition and the amputation of loose biofilm fragments [14].

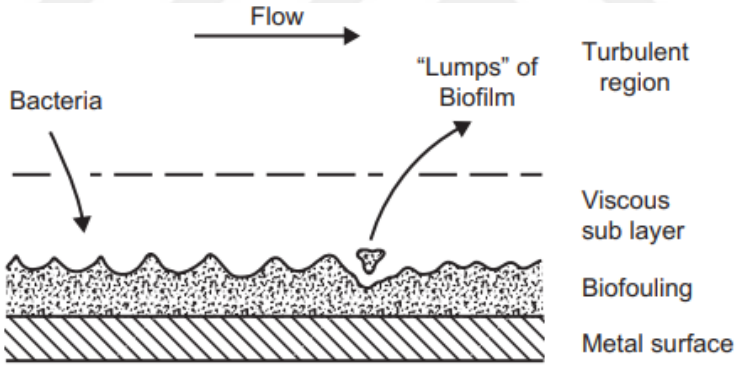


Figure 2.7 Illustration of the biofouling circuit.

Reynolds developed a criteria to discern between turbulent and streamlime flow in tubes as a result of his groundbreaking work. The difference is identified by a dimensionless number known as the Reynolds number (Re), which is given as follows:

$$Re = \frac{Dv\rho}{\mu} \tag{2.1}$$

where tube diameter is D; bulk fluid velocity is v; fluid density is ρ; fluid viscosityis μ; all in constant units [14], [18].

Though the idea was initially developed for tubular flow, by using the so-called "equivalent diameter," it may be used to flow methods other than pipes and tubes.

It has been demonstrated that the flow is turbulent above approximately Reynolds number 4000 and streamline below around Reynolds number 2000 [19]. Between these two Reynolds values is the transitional flow regime, which is sometimes described to as "boundary layer." [14], [20]

Whether flow is turbulent or streamline, as indicated by the Reynolds number, affects the shape of flow dispersal over the diameter of the maintaining tube. Under streamline circumstances, the tube's velocity shape is a parabola (see **Fig. 2.8**), the mean flow speed is equal to half that of the highest flow velocity of the tube, and the maximum velocity is observed at the center of the tube [14].

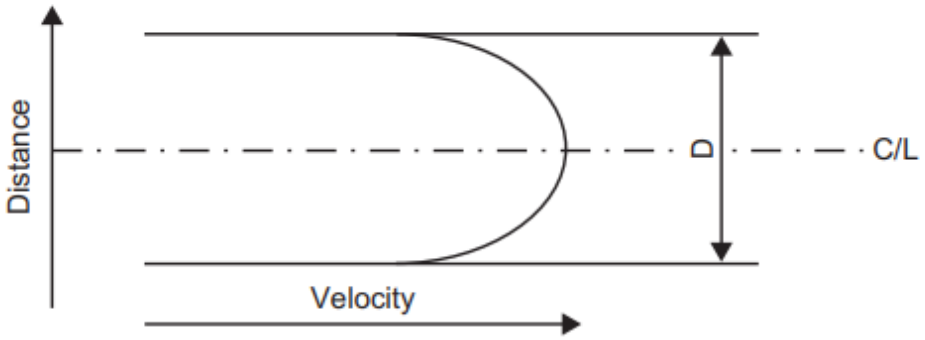


Figure 2.8 Laminar flow's velocity profile in a tube.

As seen in **Fig. 2.9**, the velocity shape is no longer a parabola when there is turbulent flow. The mean ratio of fluid velocity in turbulent circumstances is 0.82 times the at tube center velocity of flow [21].

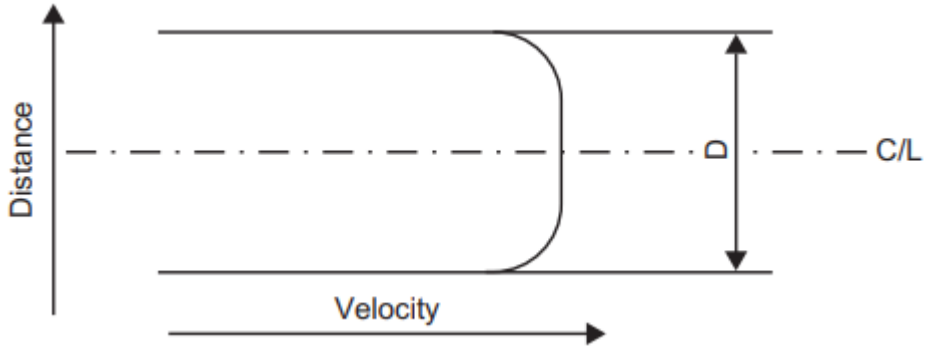


Figure 2.9 Turbulent flow's velocity profile in a tube.

A deposit on a solid surface will often be pulled away from the surface by the "drag" power at the interaction layer between the sediment and the flowing fluid. The deposit's ability to adhere to the solid surface and its inherent cohesive force in proportion to the power of the flowing stream will determine how much of the deposit is removed. It is a

highly complicated process, especially when it comes to the buildup of microbes, and it is hard, if not impossible, to forecast with any degree of precision save in very broad terms [21].

Pressure reduction in the fluid passing through the processing equipment is quite significant in process plant operations. Stanton and Pannell's work (1914) made it feasible to generate accurate pressure loss estimations under predetermined circumstances. "Friction factor" ,F, was described by them as a dimensionless concept, and connected it to the number of Renynolds ,Re, [22].

$$F = \frac{R}{\rho v^2} \tag{2.2}$$

(where R refers stress of shear).

In the region of streamline,

$$F = \frac{8}{Re} \tag{2.3}$$

In turbulent and transitional zones, the friction factor F depends on the Reynolds number, but it also depends on how rough the surface is that the fluid is flowing through. The number of dimensionless ,e/D, is utilized to account for the roughness if "e" represents the roughness' height. The loss of pressure in terms of the fluid's height ,ΔH, is calculated as follows [14], [22]:

$$\Delta H = \frac{4flv^2}{2g} \tag{2.4}$$

$$f = 2F \tag{2.5}$$

(where 'f' refers the friction factor; 'l' refers the length; 'g' refers the gravity accleration).

In engineering systems of industry, the event that temperature affects both density and viscosity causes differences in the number of Reynolds and thus the flow condition might be turbulent or laminar. Between 0 ^{o}C and 100 ^{o}C, the density of water does not change significantly. However, when the temperature rises across the same temperature range, the amount of viscosity is considerably reduced. Temperature is a crucial factor in the biofouling process since the number of Reynolds is based on temperature and it is

a critical variant in the study of flow conditions. The survival and development of biofilms contacting with water depending on temperature, for microorganisms this optimum temperature range is 25-45 ^{o}C [22].

2.2.2 Mass Transfer

Biofouling, or the buildup of undesired living material on a surface, is the result of organisms mass-transferred from the liquid flow to the solid surface and colonizing it. The movement of the mass, or concentration gradient, is the mass transfer from higher concentration to lower concentratios, acts as the “driving force” for mass transfer. When it comes to biofouling, this refers to the variations in nutrient and microbial concentrations between the receptive sollid surface and the bulk liquid flow. When the surface is colonized, the capacity to grow and develop on a sustained basis depends on the presence of sufficient nutrients and maybe more microorganisms. Additionally, mass transfer offers a way for microbial waste products to be transferred from the region of biofilm into the flowing liquid’s main body, promoting the growth of the biofilm [23].

When there is a mass transfer of microbes between the receptive surface and bulk in stationary liquid or liquid flowing under streamline conditions (for example the laminar sub-layer), the the microbial cells’ movement towards the solid surface is caused by their random movement in the liquid, which is typically mentioned as Brownian motion [14], [24].

The transport of microbial cells or nutrients differs significantly in turbulent water. The turbulence’s Eddy diffusion is superimposed on the Brownian motion. Moving down the mass transfer from the bulk liquid towards the forming biofilm on the surface are what may be referred to as “parcels of water” that contain solid particles, the organisms, or nutritional molecules [14], [24].

The diffusion rate could be calculated using Fick's equation if fluid B's main flow is not parallel to the direction that component A is diffusing through fluid B.

$$N_A = -D_{AB} \frac{dc_A}{dx} \tag{2.6}$$

where, N_A refers the molecular diffusion rate of A; C_A refers the concentration of A at a distance of x from the receptive surface; D_{AB} refers the molecular diffusivity of A through B.

The physical characteristics of A and B as well as the fluid flow characteristics, such as streamline or turbulent, will all affect how easily A diffuses through B. **Equation 2.7** is changed if there is turbulence in the system by adding a factor to account for the turbulence [14]:

$$N_A = -(D_{AB} + E_D)\ \frac{dc_A}{dx} \qquad (2.7)$$

(where eddy diffusion is referred with E_D ; E_D is very much greater than D_{AB} under turbulent flow circumstances).

In turbulent flow, The solid surface has a lamina sub-layer that prevents molecules, particles, bacteria, and their necessary nutrients from mass migrating from fluid to the surface. Under these conditions, Brownian motion, or molecular diffusion, is what causes the movement towards (and away from) the surface. The velocity of the bulk water will determine the layer thickness and, consequently, its resistance against to mass transmission. As the bulk water's speed becomes faster, the laminar sub-layers thickness decrease, in the situation of other parameters are constant, lowering the resistance against to mass transmission. Therefore, there could be more chances for colonization and successive development. Turbulent or streamline flow conditions will also affect how waste material produced by microbial activity is removed. The concentration gradient will, however, run counter to that for deposition, from greatest in the biofilm to lowest in the main flow. According to **Fig. 2.10**, underflow circumstances, a liquid stream passing over a deposit adhered to a surface will apply a pressure/force on residue [14], [25].

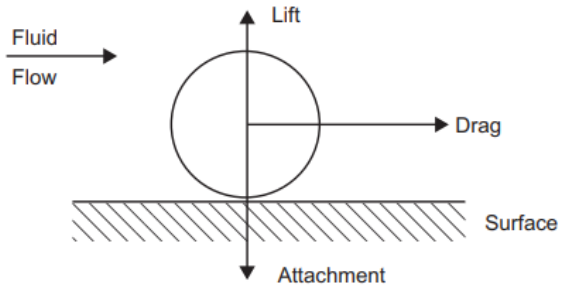


Figure 2.10 Demonstration of the forces acting on an attaching particle on a surface.

The boundary layers must be crossed by the colonizing cells that start the formation of biofilm and consequently the nutrients that support biofilm development. The variation between the bulk concentration (in turbulent circumstances) and fluid/solid interface's

concentration, or the gradient of concentration inside the laminar sub-layer, is the driving force for mass transfer. The laminar zone might restrict the potential expansion of the biofilm since it provides resistance to the transfer process. The laminar sublayer, on the other hand, will offer less barrier to mass transfer the larger the bulk velocity. Conversely, the shear forces at the liquid/solid interface improve with rising fluid velocity across a solid surface. At the deposit-fluid contact, these shearing processes place removal forces on the deposit. The cells that manage to withstand the forces of elimination are the "survivors," and they are what cause the biofilm to begin to grow. [14], [26], [27].

Fig. 2.11 shows the theoretical biofilm development curve from a moving liquid stream. Although there isn't a definite line separating them, there are three stages.

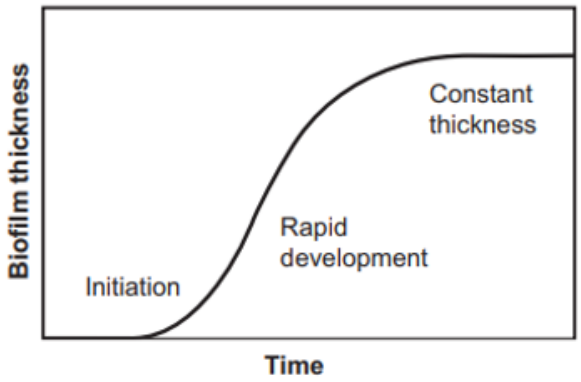


Figure 2.11 A theoretical curve of biofilm growth on a solid surface.

Assuming colonization is complete and there are enough nutrients present in the flowing water, the biofilm will expand rapidly exponentially until it attains a mostly constant thickness, which will depend on the current nutrient content and liquid velocity. **Fig. 2.12** presents a more accurate depiction of the formation of a biofilm, which will vary based on the environmental factors in each sample [28], [29].

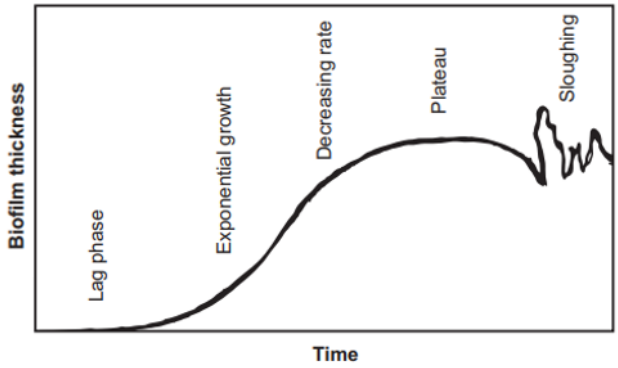


Figure 2.12 Growth curve with local operational circumstances adjusted.

The forces of mass removal and mass transfer to the surface both increases as the flow velocity in a particular system rises. There is an ideal speed where the microbial biofilm formation is greatest under these conditions [30]. This impact is seen in **Fig. 2.13**. The information was gathered using water that included nutrients and the bacterium *Pseudomonas fluorescens* (Nesaratnam, 1984). Due to the biofilm's great resistance to the movement of nutrients to the surface, particularly microorganisms, at moderate speeds, the biofilm's expanse is relatively minimal. The resistance to nutrition transfer lowers as velocity rises, while removal forces rise at the same time. Eventually, though, when the velocity is further increased, the effect of shear surpasses this benefit and the thickness of biofilm is negatively impacted, even though the mass transfer is enhanced [14], [31].

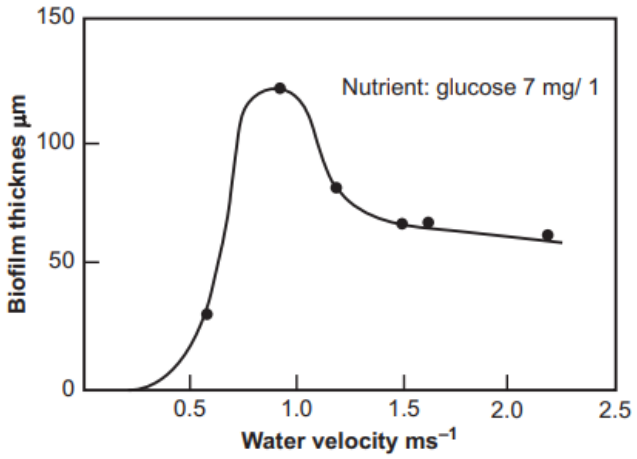


Figure 2.13 The fluid velocity effect on biofilm thickness.

More often than not, biofilm formation results from the nutrients availability rather than from the addition of new microbes (Miller and Bott, 1983). There is no need for

additional mass transfers of microorganisms once the surface has been colonized by them, as shown by **Fig. 2.14**, provided there is sufficient mass transfer of nutrients [32].

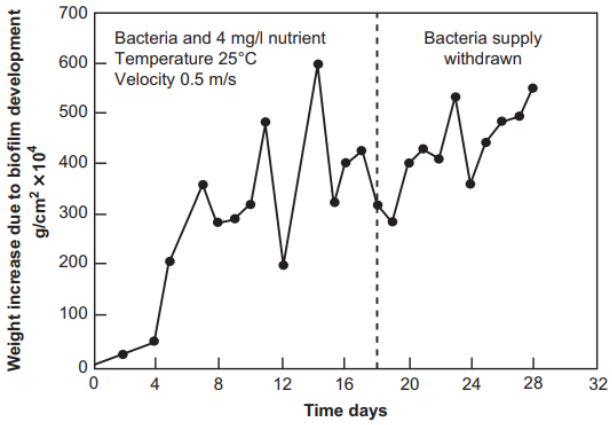


Figure 2.14 The result of removing microorganisms from a flowing stream.

The biofilm forms normally even in the absence of bacteria thanks to nutrients in the flowing water and a colonized surface. Even if there are bacteria in the water, the biofilm degrades without a source of nutrients [14], [32], as seen in **Fig. 2.15.**

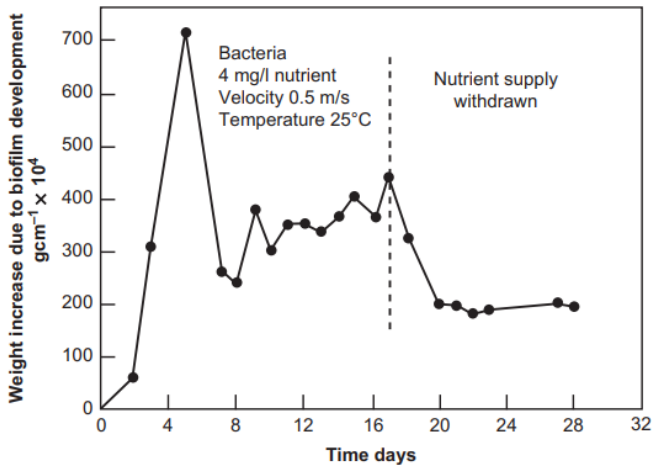


Figure 2.15 The result of removing nutrients from a flowing stream.

Obviously, growth will be impacted by nutrient concentration. The mass transfer and "driving force" for the biofilm increase with the concentration in the flowing water, creating the conditions for development [33]. With all other factors staying the same, **Fig. 2.16** shows the impact of increased nutrition availability (glucose) on the weight rise of a biofilm (Nesaratnam, 1984) [31].

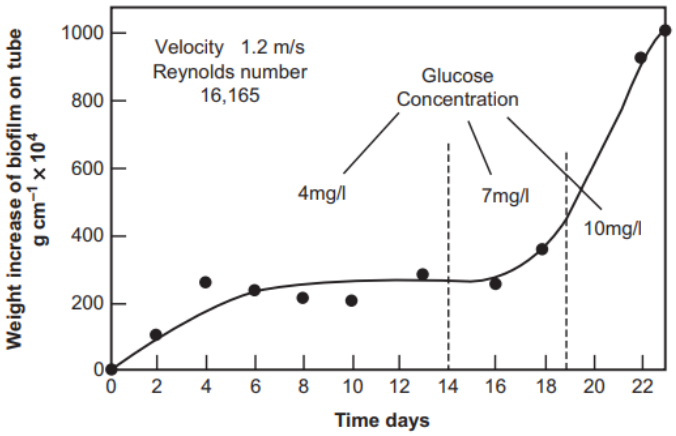


Figure 2.16 The variation in biofilm mass on a surface under various nutrient concentrations.

Additionally, the biofilm thickness, biofilm density, microbe concentration, nutrient content, and fluid shear stress are the main variations that impact the removal, also known as the sloughing process. Some bacteria, however, will be more suited to withstand the removal pressures [26], [34]. The survivors' cells may be positioned in the structure in a way that lessens the impact of speed. As a consequence, the resulting biofilm structure might take on a specific development and result in a thick biofilm, such as rod-like *Pseudomonas fluorescens* cells.

2.2.3 Heat Transfer

The temperature has an impact on microorganisms, hence fluid flow temperature has a direct impact on the development of biofilms. The temperature of the bulk fluid is impacted by heat transfer. As a result of a temperature difference, heat transmission occurs, much as the mass transfer is impacted by a concentration difference [35], [36]. The thickness of laminar sub-layer is lowered with increasing velocities of bulk, and heat transmission is enhanced because the sub-layers of slow-moving fluid also act as a heat-transfer barrier. The biofilm temperature on the surface of heat exchanger, for instance, will be greater than that of the fluid (often water) if the heat exchanger surface has biofilm, generating a "driving force" for biofouling. The influence of temperature on the formation of biofilms is seen in Fig. 2.17 within the limited temperature range necessary for microbial viability [21].

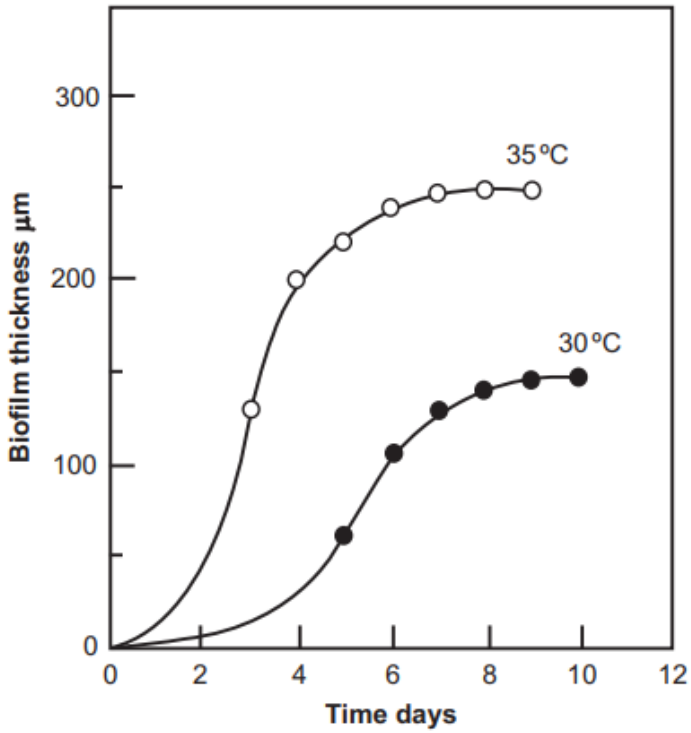


Figure 2.17 The impact of temperature fluctuation on a biofilm's thickness of *Escherichia coli* [21].

The fluids are often divided by a metal wall in many industrial operations involving heat transfer between the fluids to heat or cool as necessary. **Equation 2.8** calculates the amount of heat that is transferred Q through two surfaces of a flat wall of thickness x at temperatures T1 and T2 [21]. (T1 > T2):

$$Q = \frac{kA(T_1 - T_2)}{x} \tag{2.8}$$

(Where x is the dividing wall's thickness, A is its area, and k is the metal's thermal conductivity; all measurements are in consistent units.).

Rearranging and rewriting Equation 2.8 results in:

$$Q = \frac{(T_1 - T_2)A}{x/k} \tag{2.9}$$

('thermal resistance' is given with x/k).

Figure 2.18 shows the heat transmission condition with fouling along the dividing wall on both sides. The quantity of heat being transported must pass through each of the

fouling layers and the metal that collectively make up a composite heat transfer resistance [21].

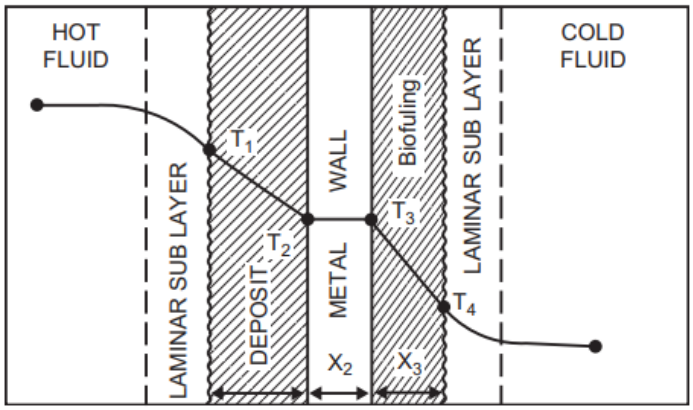


Figure 2.18 Temperature dispersion along the surface of the fouled heat exchanger.

$$(T_1 - T_2) = \frac{x_1 Q}{k_1 A} \tag{2.10}$$

$$(T_2 - T_3) = \frac{x_2 Q}{k_2 A} \tag{2.11}$$

$$(T_3 - T_4) = \frac{x_3 Q}{k_3 A} \tag{2.12}$$

Then,

$$(T_1 - T_4) = \frac{x_1 Q}{k_1 A} + \frac{x_2 Q}{k_2 A} + \frac{x_3 Q}{k_3 A} \tag{2.13}$$

Rearranging,

$$(T_1 - T_4) = \frac{Q}{A}\left(\frac{x_1}{k_1} + \frac{x_2}{k_2} + \frac{x_3}{k_3}\right) \tag{2.14}$$

Therefore,

$$Q = \frac{(T_1 - T_4)A}{\frac{x_1}{k_1} + \frac{x_2}{k_2} + \frac{x_3}{k_3}} \tag{2.15}$$

So, it can be concluded as:

Heat transferred = (Total driving force) x The area of heat transfer) / Total thermal resistance.

2.3 Marine Biofouling

The phrase “marine biofouling”, which is the most serious issue since navigation began, can be defined as “the undesired buildup of bacteria, algae, and animals on man-made structures immersed in a maritime environment.” Even while the fouling process is mostly studied because of the harm it does to man-made structures, it may also happen on the surfaces of living marine organisms and cause issues with shellfish and seaweed aquaculture. Microfoulers, such as bacteria and diatomic biofilms, and macrofoulers, such as macroalgae, barnacles, mussels, tubeworms, and bryozoans, coexist to create fouling communities [37]–[39] (See **Fig. 1.1**). Regardless of the location or the time of year, an organic coating of adsorbed substances, which depends on the glycoproteins, ions and fuvic and humic acids present in the liquid phase for its structure, will quickly cover every chemically inert submerged surface. The biofouling process begins less than 24 hours after the creation of this “conditioning layer”, which is accomplished by Van der Waal forces and electrostatic interactions. The flow of liquid through Brownian motion, sedimentation, and convective transmission encourages contact and colonization between the microorganism and the surface. Additionally, because flagella are used for propulsion, organisms can search for substrates by themself. Bacteria, yeasts, and diatoms are the primary colonizers that settle inside protective biofilm formations as secrete extracellular polymeric substances, and this secretion modifies the local surface chemistry, which might encourage further development like the enlistment and colonization of microbes, by encasing and securing them to the substrate. The spores of macroalgae, fungus, and protozoa, which are considered secondary colonizers, are said to settle around one week after immersion when the environmental circumstances are favorable, according to the literature. The entrance of invertebrate larvae to the surface during the spawning season, which occurs on average after 2-3 weeks of immersion, is sometimes regarded as the last stage of the marine biofouling process [40].

Salinity, temperature, nutrient levels, flow rates, and solar radiation intensity are some of the variables that affect biofouling. These elements change with the seasons, the

location, and the depth. In temperate climates, seasonality has a significant impact on colonization and succession in biofouling communities, with winter seeing less fouling development (due to the reductions in light levels, water temperature, and the number of spores and larvae). Due to the constancy of water temperature and light levels at these latitudes, which contribute to a continual reproduction and settling of some macrofouling species, tropical and subtropical locations exhibit less change in the biofouling communities. Fouling is still a highly complicated and dynamic issue in tropical regions [37], [40], [41].

Geographical location affects the fouling species, with sub-tropical and tropical locations experiencing strong fouling pressure due to the more favorable physical and chemical circumstances compared to temperate, cold, and polar zones. Fouling is often caused by the same primary groupings of organisms over the world, however, the specific dominating species involved might differ [39], [40].

2.4 Conclusion

Both industrial biofouling and marine fouling are affected by fluid flow velocity, temperature, and availability of nutrients. The effect on marine biofouling is actually the same as industrial biofouling, but the marine environment is more complicated in comparison with the industrial systems and not adjustable. For example, in the heat exchanger, fluid velocity and tube diameter can be designed, see 2.2.1.

Biofouling is triggered by:

- Temperature,
- Fluid flow velocity,
- Nutrients' concentration of fluid,
- Organism's concentration of fluid,
- Shear force.

The effective presence of a laminar sub-layer in industrial biofouling prevents the macrofouling with a contribution of shear resistance caused by velocity and friction.

3
ANTIFOULING

3.1 Antifouling

Fluid-contact surfaces such as the interior surface of heat exchanger tubes and pipes, as well as ship hulls and marine platforms, are exposed to attack by microorganisms from fluid (generally water). These surfaces need to be protected against bio-foulants and these attempts are known as “antifouling”. With the initial marine activity, biofouling control initiatives have started. This chapter focuses on the history of antifouling approaches and the evolution process up to current circumstances to give research motivation more clearly [39], [42].

3.2 Antifouling Methods’ History

The history of navigation has paralleled the evolution of fouling control strategies. A historical technique of preventing fouling on ship hulls was the use of poisonous antifoulants, but biocides like arsenic, lead, mercury, and organic derivatives of them have since been outlawed because of the dangers they presented to the environment. Tributyltin, an antifoulant, was utilized in conjunction with a ground-breaking self-polishing copolymer technology that employs a similar heavy metal toxic effect to repel marine species (TBT). The foul release coatings (FRCs) are antifouling treatments without heavy metals. Because certain seals, ducks, and fish have tin bioaccumulation problems and cause catastrophic shellfish deformities, the use of organotin was finally prohibited, resulting in legislation that led to tributyltin's global ban. Due to the limited of effective volatile organic compound (VOC) regulations in antifouling products, organic surface coatings that are thermoplastic, non-convertible, and just vaporize a solvent to dry now widely available. The UK MOD VOC goal values are now 400 gL^{-1} water-free paint [29], as stated in March 2005, however, this is susceptible to change as the toxicity of contemporary tin-free antifouling solutions is addressed. Although antifouling methods have been developed for a long time, in the last 10 years there has been a greater emphasis on ecologically friendly alternatives. Figure 3.1 illustrates the key antifouling generation with time [39], [40], [43].

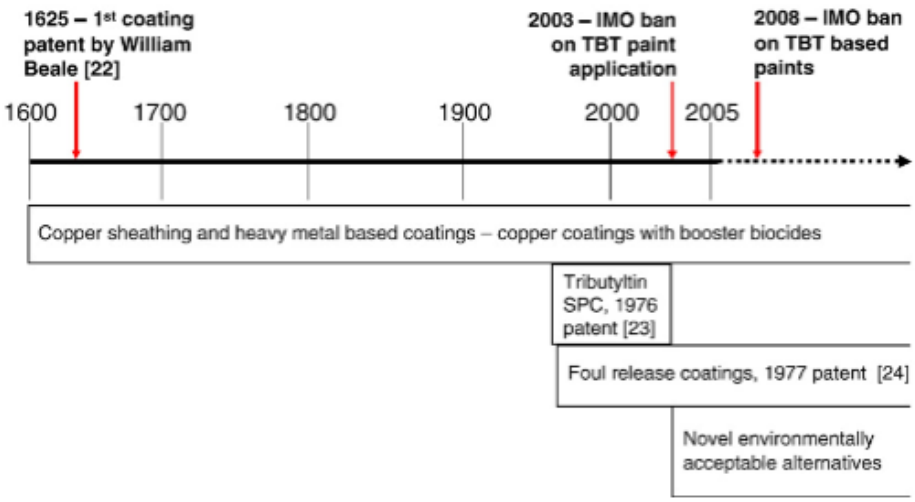


Figure 3.19 The illustration of the important antifouling generation with the timeline.

3.3 Modern Approaches

3.3.1 Heavy metals

Since TBT was banned in 2003, there has been researched towards ecologically friendly substitutes, as previously discussed. Other metallic species are currently used as stand-ins and are supplied using a modified self-polishing copolymer delivery method, such as copper and zinc. Hydrolysis and erosion are both used in the self-polishing copolymer (SPC) approach to managing the antifouling action. The hydrolysis of the antifouling component from the polymer backbone is made possible by seawater infiltration, and the solubility of the coating leaves the surface polished. A longer lifetime is made possible by the coating's surface's controlled disintegration.

By utilizing either an insoluble matrix or a soluble matrix, there are two option significant ways for regulating the antifoulant chemicals releasing from protective coating.

Due to the partitioning of metabolic processes, heavy metals are frequently hazardous to both humans and marine creatures. Alternative methods are replacing the cautious utilization of heavy metal contents to prevent biological fouling in the marine ecosystem as a result of the TBT prohibition and enhanced restrictions on toxicity limits [44]–[46].

3.3.2 Booster biocides approach

In addition to growing skepticism over the usage of copper, a select set of macrophytes, including the important fouling algae species Enteromorpha (now Ulva), have also been shown to be more tolerable. Consequently, booster biocides have been used to lengthen and improve the performance of copper-containing biological fouling protection systems. The UK Health and Safety Executive has controlled two important booster biocides, with Diuron being prohibited from use and Irgarol being limited to use on boats longer than 25 m. The persistence and toxicity of terrestrial pesticides, which have been altered for use in protection systems against to biofouling in marine environment, are becoming a bigger problem. This strategy frequently favors one species over another or is overly general, affecting creatures that are not the objective. The coating capacity to continuously leach the booster biocides limits the efficacy of the copper-based coatings. Better control is needed for the amounts of released biocide. In free association varnishes, whether they are resolvable or not, and ongoing monitoring is required for persistence of them in marine residues owing to such processes as incorporation into damaged paint particles. In response to the requests for an efficient antifouling approach to replace TBT, the use of booster biocides offers a temporary fix [24], [46].

3.3.3 Foul release coatings

Low surface energy is how foul release coatings (FRCs) work, which makes it harder for organisms to form a solid interfacial contact with the surface. Once the ship has passed a certain velocity, when the velocity of ship is generally 10 to 20 knots, according to the fouling community, organisms can be removed due to the coating's molecular smoothness. By reducing the thermodynamic effort of adhesion, such a non-stick surfaces help remove biofouling through tensile and shear stresses in addition to their own weight. The crucial surface free energy (22–24 mN m^{-1}) and lower elastic modulus could combine to cause the interface/joint between the adhesion of organisms and the coated solid surface to fracture and collapse. A marine biofouling content's attachment to a moist surface results in.

Fluoropolymers and coatings made of silicone-based polymers are the two main categories of FRCs. In contrast to fluoropolymers, which normally have an application thickness of 75 m, silicone coatings often have a 150 m thickness. The coating modulus

may be managed by adjusting the coating thickness. Thicker coatings, such as those found on silicone elastomers, are more effective since it takes less force to break the link between the coating and the foulant. Instead of the shearing correlated with the fluoropolymer coatings' tougher, slimmer coatings, the adhering organism is removed by a peeling fracture process.

Diatoms and other low-form biological foulants are very persistent and challenging to get rid of from foul-release coatings. This implies that it will be challenging to remove diatomaceous slime from a providing non-stick protection systems as the ship is in motion. FRCs may be predicted to achieve removing Ulva biofilms, 4-6 days old, at practically relevant vessel velocity using versions of low-form separation, with over 60% zoospore elimination observed around 17.7 knots.

These low-energy coatings offer a novel method for creating an environmentally acceptable replacement for biocide-based antifoulants due to their solely physical deterrent effects. It provides a broad range of antifoulants without the biodegradation problems, statutory requirements, or registration costs associated with an active antifouling molecule. This is a successful passive strategy for dealing with the hostile sea environment. The essential speed velocity required to remove the foulers, however, rises due to the tenacity of biofilms. Biological communities are permitted to develop and macrofoulers can subsequently be translocated biogeographically, generating environmental difficulties of foreign species trafficking. When the ship is dockside, this procedure does not prevent biofouling. The elimination of indigenous species, competition for ecological niches, problems for local biodiversity and aquaculture, and the eradication of native species are only a few of the detrimental consequences of foreign species on natural biological ecosystems. The dockyard's hazardous silicone lubricants and certain silicone-based paints' usage of the curing ingredient dibutyltin laureate raise further concerns. The chemicals TBT and monobutyltin (MBT) may be present in this organotin catalyst. FRCs need certain operating profiles to operate effectively and are not an effective antifouling option for vessel hulls in general [24], [46].

3.3.4 A biomimetics approach

The word "biomimetics" refers to design that is inspired by biological processes rather than a literal imitation of such activities. The expression implies that the natural

environment serves as a guide for design of engineering inventions or as a “bottom-up” approach to structuring hierarchical systems. One example of the use of a biomimetic approach for coatings is the regulation of deposition of inorganics such as silica and silver by biomolecules.

The diverse mechanisms that marine organisms use to protect their own surfaces from fouling have been investigated. Within the marine ecosystem, evolution has allowed for the development of certain antifouling properties. Marine organisms have both physical and chemical methods to protect themselves from the harmful process of biofouling. Natural chemical defense methods have been of interest over the last two decades as chemical prospecting for pharmaceuticals has backed this type of research and exploration. A molecular approach to antifouling has yielded a variety of potential compounds [24], [46].

4
GLASS-CERAMICS

4.1 Definition of Glass-Ceramics

Glass-ceramics are inorganic substances having controlled crystallization and nucleation capabilities while preserving a glassy form. The process of crystallization involves introducing nucleating chemicals to the glass matrix. TiO_2 (titanium dioxide), Cr_2O_3 (chromium (III) oxide), ZrO_2 (zirconium dioxide), P_2O_5 (phosphorus pentoxide), and fluorides are the primary contents that act as nucleating agents, acting as nucleation centers, within glass-ceramics. Controlled heat treatment is required to begin nuclei growing and eventually to develop crystallization [47], [48]. Controlled heat treatment and microstructural differences have been given in **Fig. 4.1.**

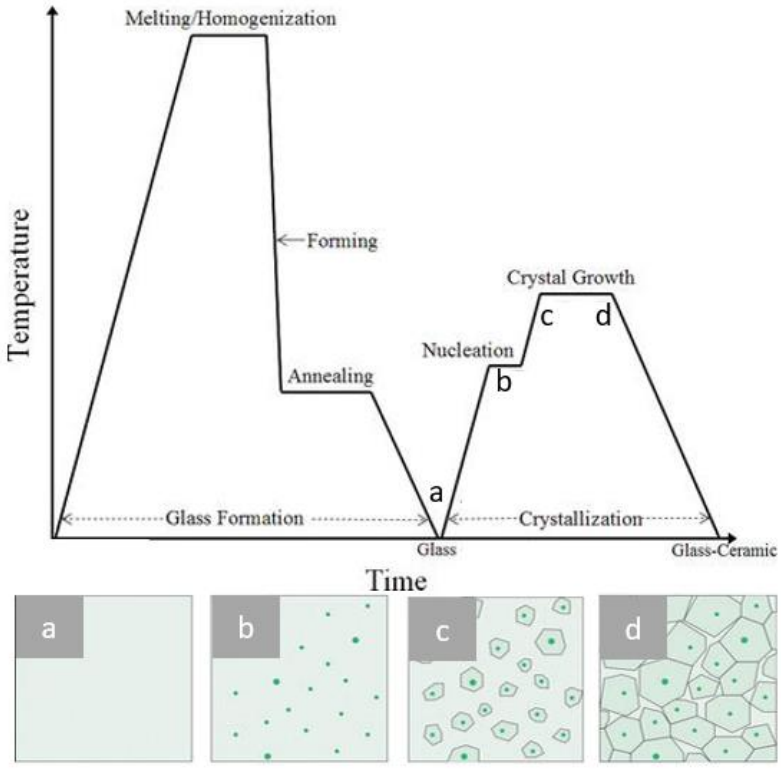


Figure 4.1 a) fully glass / amorphous structure, **b)** amorphous structure with nuclei, **c)** beginning crystallization in an amorphous structure, and **d)** devitrified amorphous structure [47].

The major stage of glass-ceramic manufacture, known as controlled crystallization or crystallization heat treatment, aims to transform amorphous glass into microcrystalline ceramic. **Fig. 4.2** illustrates how temperature affects the development of nuclei and the growth of crystals. Any glass's propensity to form crystal nuclei and grow them may be used to explain how it crystallized. If enough nuclei (at least $10^{12} – 10^{15}$ nuclei in 1 cm^3 volume) are produced by heterogeneous nucleation below the equilibrium melting temperature, a semi-stable temperature range is created where crystal formation is possible [49].

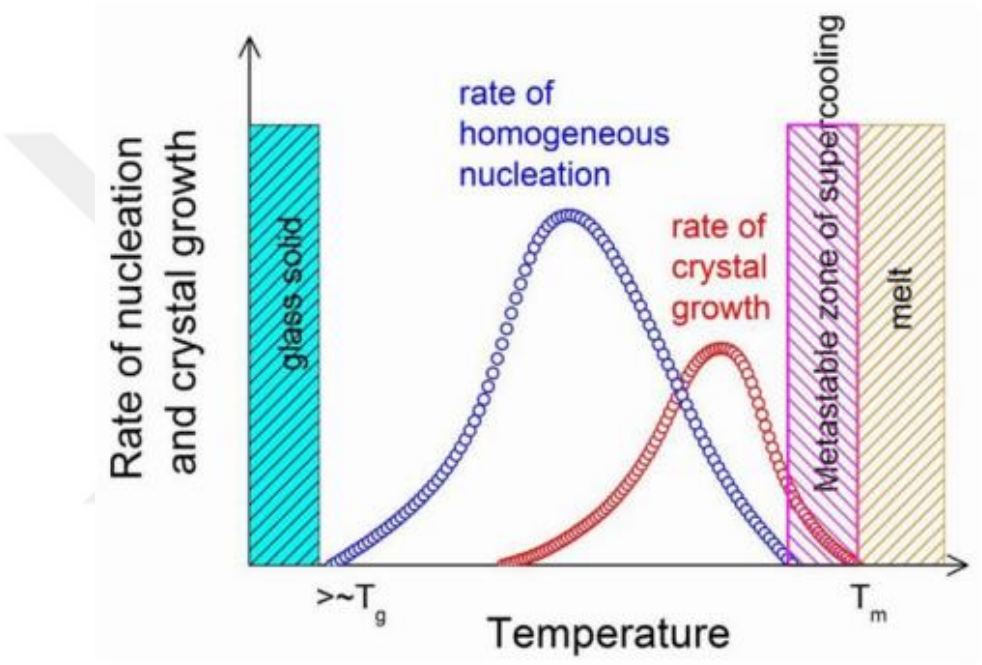


Figure 4.2 The impact of temperature on crystal development and nucleation in glasses [50].

4.2 Properties of Glass-Ceramics

The thermal characteristics of glass-ceramic materials prevent any shrinking during manufacture. They may be widely applied in technological and industrial applications in this way, particularly in kitchenware. The necessary transparency and opacity values may be attained with the use of crystals and microstructure control due to their glassy phase and nonporous structure. All necessary colors may be achieved in glass-ceramic applications, which is another optical characteristic. Due to the crystal structure, glass structure, and chemical endurance property, the 7 chemicals exhibit outstanding chemical properties when they interact with glass-ceramics. Mechanically, flexural

strengths of up to 500 Mpa are possible, and the improvements led to toughness values of more than 3 Mpa.$m^{1/2}$ [47], [51]–[53].

4.3 Formation of Glass-Ceramics

4.3.1 Pressing

In this technique, pressure is used between a mold and a plunger to form the glassware. It can be utilized that metal presses, air vacuums, and other sorts of pressing machinery [47].

4.3.2 Casting

For this ancient method to work, the temperature must be above the glass transition temperature and the glass viscosity must be at a minimum. This method could be used in the field of dentistry [47].

4.3.3 Spinning

This technique differs from traditional casting in that it calls for the use of a conical mold that should revolve. The viscosity must fall within the range of 30 and 100 Pa s for this procedure. This is how vintage television cathode ray tubes were produced [47].

4.3.4 Rolling

The rolling technique is pouring molten glass onto a press table that is being water-cooled and then rolling it out. Viscosity should be between 700 and 1000 Pa s. Flat glasses may be made using this technique [47].

4.3.5 Float process

The float or Pilkington method, which is currently most frequently employed in the manufacturing of flat glass, is the fundamental forming in a molten tin bath. Since it comes from the bottom of the furnace, the molten glass is flattened and reinforced in the tin bath at low temperatures. The flat glass keeps moving along the conveyor belt, moves into the annealing line, releases the tension, and keeps going [47].

4.3.6 Direct forming or reforming of glass-ceramics

In some cases, ceramic phases can be used to create glass-ceramics. It becomes feasible to mold the remaining glass stages as they soften [47].

4.4 Application Areas of Glass-Ceramics

Glass-ceramics have a wide range of industrial applications because of their superior technical qualities. Table 4.1 lists a few of these application areas.

Table 4.1 The list of some glass-ceramic systems, and main crystals, properties, and application areas of them [54], [55].

System	**Main Crystalline Phase**	**Property**	**Application Area**
$Li_2O.Al_2O_3.SiO_2$ (ZrO_2, TiO_2)	β-quartz β-spodumene β- eucryptite	Low thermal expansion High-temperature resistance	Kitchenware Telescope Mirrors Oven Tops
$Li_2O.Al_2O_3.SiO_2$ (P_2O_5)	$Li_2O.Al_2O_3.SiO_2$	Dielectric properties Chemical resistance	Electronic Insulation Optical Coding Magnetic Recording Head Electric Sleeve
$MgO.\ Al_2O_3.SiO_2$ (P_2O_5, TiO_2)	Cordierite ($Mg_2Al_4Si_5O_{18}$)	Radar permeable Low thermal expansion High strength	Missile Cap Radar Dome
$PbO.ZnO.B_2O_3.SiO_2$ (F)	Rankinite ($3CaO.SiO_2$)	Heat & Vacuum insulation	Electrotechnology Microelectronic Circuits Capacitor
$BaO.Al_2O_3.SiO_2$ (TiO_2)	Celsian ($BaAl_2Si_2O_8$) Barium Titanate ($BaTiO_3$)	High strength Thermal shock resistance	Kitchenware Cookware

Table 4.1 The list of some glass-ceramic systems, and main crystals, properties, and application areas of them (continued) [54], [55].

$SiO_2.Al_2O_3.MgO.K_2O$	Phlogopite $[KMg_3AlSi_3O_{10}(F,OH)_2]$	Turning ability Dielectric properties	Electrotechnology Insulator Hermetic Seals
$SiO2.CaO.Na_2O$ (P_2O_5)	Apatite $Ca_5(PO_4)_3(F,Cl,OH)$	Biocompatibility Chemical resistance	Dentistry Prothesis
$SiO_2.Al_2O_3.MgO$ (TiO_2)	Mg-Al Titanate $MgxAl_{2(1-x)}Ti_{(1+x)}O$	High hardness Resistance	Construction
$SiO_2.Al_2O_3.CaO$ (ZnO)	Wollastonite $(CaSiO_3)$	High hardness Resistance	Architectural Materials
$SiO_2.Al_2O_3.MgO.CaO$ (Sulphide, fluoride)	Wollastonite $(CaSiO_3)$ Anorthite $(CaAl_2Si_2O_8)$ Diopside $(MgCaSi_2O_6)$ Pyroxene $[(Na,Ca)_n(Mg,Fe,Al)(Al,Si)_2O_6]$	High hardness Abrasion resistance Chemical resistance	Floor Tile Exterior Architectural Materials Pump Pipe

5
GLASS-CERAMIC COATINGS

5.1 Glass-Ceramic Coating on Metal Substrates

Glass-ceramic coatings, which are also known as vitreous enamel coatings are a superior technique for protecting metal substrates and extending the service life of metal items [56], [57]. To create glass-ceramic coating, an intermediate product is needed. This product consists of precursor glass, also known as frit, and other additives, such as pigments and floaters [58], [59]. The main component of the glass-ceramic coatings is precursor glasses, which have a fully amorphous structure. Precursor glass is essentially glass granules or flakes produced by melting a variety of inorganic oxides at 1000–1500 °C and then a fast cooling process [60], [61]. Additionally, various additives are required to increase certain qualities including application, decoration, and engineering. Before application, the mixture of precursor glass and additives are milled to achieve a suitable particle size, which is determined according to the application method. To avoid particles having inappropriate particle sizes for the application, a sieving process is carried out [58].

Wet application techniques for glass-ceramic coating include flow coating, spraying, dipping, and electrophoretic deposition. The suspension is created by mixing water with the powdered frit and grinding ingredients. On the other hand, powdered frits may be used to cover metal substrates with glass-ceramic coatings following the crystallization process utilizing thermal spray coating or electrostatic powder spraying for dry application [59], [60], [62].

Following the application of the frit powder to the substrate, the devitrification phase starts. Based on the coating formulation and the metallic substrates, the devitrification or crystallization procedure's properties alter. Glass-ceramic coatings adhering to steel substrates are heated between 780 and 850 °C, whereas glass-ceramic coatings adhered to aluminum substrates are heated between 500 – 570 °C [59], [62].

5.2 Chemical Contents and Their Objectives of Glass-Ceramic Coatings

Glass-ceramic coatings are composed of amorphous structures known as "frit." According to the Seger formulation, these are semicrystalline glassy coating materials produced by vitrifying and recrystallizing oxides such as SiO_2, B_2O_3, Al_2O_3, Na_2O, K_2O, NiO, CuO, CoO, P_2O_5, Fe_2O_3 [63]. Four groups are used to categorize its production: Frit is produced by high-temperature fusing and quenching, followed by milling of the frit with or without milling additives, application of the milled frit to the metal substrate, and a third step of crystallization at temperatures of 720–850 °C [47]. Based on the crystal and amorphous structure created by the process, a decorative coating material that is resistant to mechanical, chemical, and thermal damage is achieved [51].

While **Table 5.1** shows the functions of oxides and minerals in glass-ceramic coating, **Table 5.2** shows how oxides can be grouped according to how they operate in the glass-ceramic structure. Silica has the capacity to create glass at a high enough temperature in glass-ceramic systems without the aid of any other components. SiO_2 is used more frequently in glass-ceramic formulations than any other glass-ceramic component. The vitreous coating, such as glass-ceramic coatings, is a network of silica tetrahedra with other substances added as modifiers. Low melting point components, melting at temperatures of 1050 °C or below, contain one or two parts of SiO_2 per part of other components [58], whereas compositions that melt at 1250 °C or above contain three to five parts of SiO_2. SiO_2 has a very high melting point (more than 1700 °C), which is by far its biggest drawback as a coating material [64].

Table 5.1 The functions of minerals and oxides**,** used in glass-ceramic coatings [65], [66].

Component	Minerals	Functions
SiO_2	Quartz Feldspar	Glass forming oxide, a refractory component, hardens the vitreous system, improves chemical resistance, and raises viscosity.
B_2O_3	Borates	Flux decreases viscosity, improves surface hardness, and creates the vitreous matrix.

Table 5.1 The functions of minerals and oxides**,** used in glass-ceramic coatings (continued) [65], [66].

Na_2O K_2O Li_2O	Albite Feldspar Spodumene	Alkaline components that reduce the glass' flexibility, raise its brightness, and lower the glass' softening point.
Al_2O_3	Feldspar Corundum	Decreases the expansion coefficient, increases viscosity and the resistance to heat, chemicals, and mechanical stress, and favors an opaque finish.
ZrO_2	Zirconium	Opacifies final product and increases resistance to acids, bangs, and shocks.
ZnO	Zincite Blende Wurtzite	Decreases the expansion coefficient and enhances surface quality and brightness.
CoO	Cobalite	It creates a structure with homogeneous spaced tiny bubbles and it is a highly powerful adhesion agent.
NiO	Nicolite	Another adherence agent, it results in a structure with a few sparsely distributed big bubbles.
CuO	Copper Oxide	At lower temperatures, it starts the adhesion reaction when mixed with primary bonds.
MnO_2	Manganese Dioxide	Creates brown-colored frits, amplifies dark colors, and serves as a weak bonding agent as well as an oxidant.
Sb_2O_3	Antimonite	Increases acid resistance and provides a high degree of opacity.
TiO_2	Rutile Anatase	Opacifiers improve whiteness, brightness and enhance heat- and acid-resistance.
BaO	Baryte Witherite Calcite	Alkaline-earthy components that integrate anti-acid glass-ceramics coating, increasing their resistance, their smelting facility and their viscosity.
CaO MgO	Dolomite Limestone Periclase	Also, their presence in precursor glasses, which used with electrostatic application, arranges the surface resistivity with polycation effect.

Table 5.1 The functions of minerals and oxides**,** used in glass-ceramic coatings (continued) [65], [66].

BaO	Baryte Witherite Calcite	Alkaline-earthy components that integrate anti-acid glass-ceramics coating, increasing their resistance, their smelting facility and their viscosity. Also, their presence in precursor glasses, which used with electrostatic application, arranges the surface resistivity with polycation effect.
CaO MgO	Dolomite Limestone Periclase	
P_2O_5	Apatite	Changes the finish's opacity, enhances color stability, and lessens chemical resistance.
F_2	Fluorite	Softens glass and affects transparency.

Table 5.2 The classification of oxides in the glass structure according to their functions [54], [58], [67].

Glass Former	**Glass Modifier** (R_2O)	**Glass Modifier** (RO)	**Glass Former** (RO_2, R_2O_3)	**Adhesion Promoter**
SiO_2	Li_2O	MgO	TiO_2	CaF_2
B_2O_3	Na_2O	CaO	ZrO_2	MnO_2
	K_2O	SrO	SnO_2	CoO
		BaO	Fe_2O_3	NiO
		ZnO	Al_2O_3	

There may be differences in the number of structures that make up the frit structure. The quantity and kind of oxides utilized may change depending on the characteristics anticipated from the construction.

According to their role in the chemical structure, the oxides utilized in the chemical makeup of enamel are analyzed under five headings: fluxes, refractories, adhesion agents, opacifiers, and color agents [58].

5.2.1 Fluxes

The primary function of the oxides in this category is to lower silicon dioxide's melting point, which is the main glass-making oxide in the enamel composition. The uniformity of the enamel is also improved by the oxides in this category. A mixture with the right consistency improves surface quality while also strengthening the connection between enamel and metal. Additionally, the acidic refractories and these fundamental characteristic oxides combine to produce the glass structure. Borax, soda ash, soda nitrate ($NaNO_3$), fluorspar (CaF_2), cryolite (Na_3AlF_6), barium carbonate ($BaCO_3$), magnesium carbonate ($MgCO_3$), litharge (lead (II) oxide), red lead (lead (II, IV) oxide, and zinc oxide (ZnO) can all be mentioned as main raw materials in this category [67].

5.2.2 Refractories

These substances sustain the melt's acidic component and aid in the creation of the glass structure. Quartz, feldspar, and clay are the three most significant substances in this class. It is a manufacturer of quartz glass and is in charge of giving the finished product its mechanical and chemical qualities [58].

5.2.3 Adhesion Agents

When enamel coatings are deposited to metal surfaces, they must bind with the metal in order for them to be effective. So, oxides including cobalt oxide, nickel oxide, and copper oxide are employed in the melt [54], [58].

5.2.3.1 Adhesion Mechanism Between Glass-Ceramic and Metallic Substrate

5.2.3.1.1 Diffusion Theory

Iron diffusion from the metallic substrate to the glass-ceramic material and silicon diffusion from the glass-ceramic to the substrate material takes place at the interfaces between the glass-ceramic coating and the metallic substrate. Therefore, it is believed that the diffusion process contributes to the adhesion mechanism [68].

5.2.3.1.2 Chemical Theory

According to this theory, the metal is driven to oxidize and produce the iron oxide (FeO) molecule, when sintering, glass dissolves the metal's existing oxide layer [69].

Reactions that take place in the substrate during the glass-ceramic coating's firing:

$$Fe_3O_4 \rightarrow Fe^{2+} + 2Fe3+ + 4O2 \quad (5.1)$$

$$2\ Fe3+ + Fe \rightarrow 3Fe2+ \quad (5.2)$$

Fe reduces the molecules of cobalt oxide (CoO) and nickel oxide (NiO) to produce metallic cobalt and nickel in glass-ceramic coating.

$$Fe + CoO \rightarrow FeO + Co \quad (5.3)$$

$$Fe + NiO \rightarrow FeO + Ni \quad (5.4)$$

The compound's oxygen affinity grows as you move along the Ellingham diagram's bottom. Iron has a greater affinity for oxygen than nickel and cobalt at the glass-ceramic heating point, as shown in **Fig. 5.1** Cobalt and nickel are therefore mostly employed to give adhesive properties [59], [69].

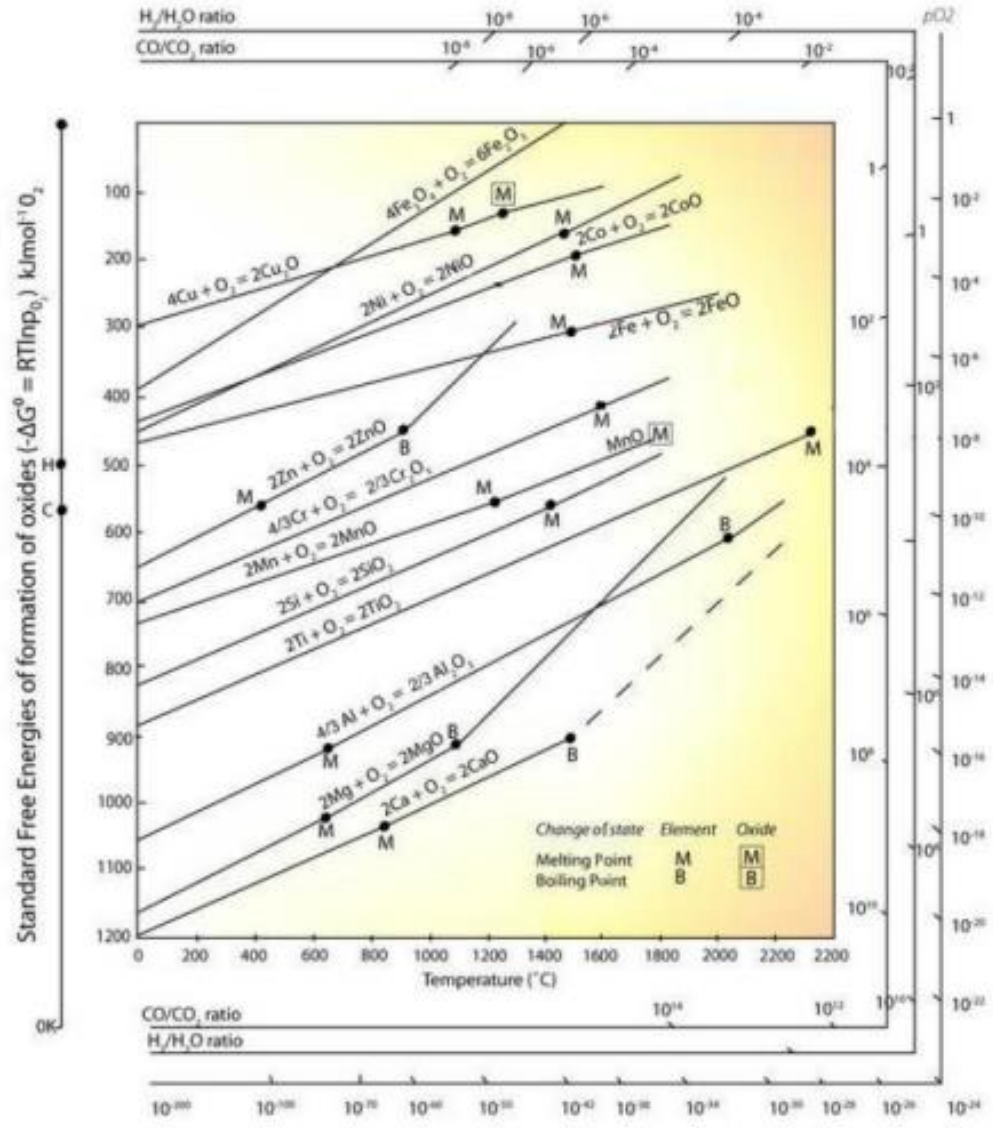


Figure 5.1 Ellingham Diagram [59].

5.2.3.1.3 Mechanical Theory

The field of contact between the substrate and coating serves as the foundation for the mechanical approach[59]. The glass-ceramic/substrate interaction is improved by chemical (using hydrochloric HCl and sulfuric acid (H2SO4) and mechanical treatment of the metallic substrate surface [62].

5.2.4 Opacifiers

The primary function of oxides in this category is to provide an opaque enamel covering. This category of oxides typically includes zirconium oxide, antimony oxide, titanium dioxide, sodium antimonate ($NaSbO_3$), and zirconium silicate ($ZrSiO_4$). These oxides all have the ability to be refractory as a property. In addition, there are supplementary opacifiers like cryolite and fluorspar that make the melt more fluid [67].

5.2.5 Color Agents

With their superior aesthetic and technological attributes, enamels are the coating type that is at the forefront. For this reason, various hues and tones have to be used in coatings. Cobalt oxide, copper oxide, iron oxide, and nickel oxide are the oxides that are most frequently employed in this context. These oxides can be employed as coloring agents, or color can be directly added to the precursor glass [67].

5.3 Properties of Glass-Ceramic Coatings

5.3.1 Thermal Properties

5.3.1.1 Thermal Expansion

When a material expands due to thermal expansion, its volume or length rises as the temperature does. In other words, by monitoring the changes at a single unit of temperature change, it is possible to estimate the volume or length changes in the substance. Multiplying the change in unit shape by the temperature difference yields the thermal expansion coefficient. The change in length of the material as the temperature increases by 1 °C is explained by the linear thermal expansion coefficient. The linear thermal expansion coefficient (α) is calculated using the equation shown below.

$$\mathrm{A} = \frac{1}{l}\, x\, \frac{\Delta l}{\Delta t} \tag{5.5}$$

where l is the length of the material, and Δl is the elongation obtained by means of heating through Δt °C.

The volume thermal expansion coefficient illustrates how, when temperature increases by 1 degree Celsius, a material's volume changes. The volume thermal expansion coefficient (β) and the linear thermal expansion coefficient (α) are inversely proportional in isotropic materials like amorphous structures and glasses.

$$B = 3 \cdot \alpha \tag{5.6}$$

Because it impacts the relationship between glass-ceramic coatings and metal, the thermal expansion coefficient of glass-ceramic coatings is significant. Glass-ceramic coating technique requires that the thermal expansion coefficients of the substrate metal and the coating be near to one another. If the thermal expansion coefficient of the glass-ceramic coatings is smaller than that of metal, the glass-ceramic coating will shrink fast during cooling after firing treatment. When the adherence between the glass-ceramic coating and the metal is very strong, as defined by the glass-ceramic coatings adhesion characteristics, the metal surface stands out against glass-ceramic coating shrinkage. When the tensile strength of the glass-ceramic coatings is exceeded in this situation, stress-developing fissures remain in the structure. On the other hand, chipping problems happen when the compressive strength of the glass-ceramic coatings is greater than the thermal expansion coefficient of the metal. Because compressive strength is 15-20 times more harmful than the tensile strength, glass-ceramic coatings should have a lower expansion coefficient than metal [70], [71]. The volume thermal expansion coefficients of various metals and glass-ceramic coatings are listed in **Table 5.3**.

Table 5.3 Cubical thermal expansion coefficients of some glass-ceramic coatings and some metals [70].

Material	**Cubical Thermal Expansion Coefficient ($3.\alpha \times 10^{-7}$)**	**Temperature Range (°C)**
Iron	426	0-500

Table 5.3 Cubical thermal expansion coefficients of some glass-ceramic coatings and some metals (continued.) [70].

Low Carbon Steel	465	27 – 760
Cast Iron	378 – 390	20 – 500
Ground Coat for Steel	240 – 300	0 – 100
Cover Coat for Steel	280 – 360	0 – 100
Ground Coat for Cast Iron	250 – 300	0 – 100

5.3.1.2 Thermal Shock

According to the theory put forward by Winkelmann and Schott, the thermal shock resistance of glass-ceramic coatings defines how the glass-ceramic reacts to abrupt temperature fluctuations:

$$K = \frac{P}{\alpha . E}\, x \sqrt{\frac{\lambda}{c}\, d} \tag{5.7}$$

where P is tensile strength, α is the linear expansion coefficient, E is the elasticity modulus, λ is the thermal conductivity coefficient, c is the specific heat and d is the density.

Different factors, including not just certain thermal qualities but also a range of other aspects, affect thermal shock resistance. The most significant factor in this is internal strain. Glass-ceramic coatings experience compressive stresses during rapid heating and tensile strains during rapid cooling because they have a lower coefficient of thermal expansion than metal. Glass-ceramic coatings are more resilient to thermal shock during fast heating because compressive pressures are less than tensile forces. In this instance, the size of the strains is also crucial. Convex surfaces have higher tension than concave surfaces, which results in a weaker thermal shock resistance for convex surfaces. The thickness of the glass-ceramic coating and the metal of the substrate both have an impact on thermal shock resistance [71].

Fast cooling decreases the thermal shock resilience of glass-ceramic coatings. On the other side, a cooling atmosphere is essential. Compared to thermal shock with cold water, thermal shock with cold air has a smaller effect. In order to evaluate the thermal shock resistance of glass-ceramic coatings, cold water experiments are utilized [72].

5.3.1.3 Fusibility and Fluidity

When melting and firing the raw material for glass-ceramic coatings following application, two crucial molten state characteristics—fusibility and fluidity—come to the fore. It is controlled by the chemical composition, but the computation has primarily been experimental. Most of the computations were accurate for a particular composition range. For each glass-ceramic coating composition, tests including the cone fusion test, fusion flow test, fusion block test, bead test, and interferometer test have thus become crucial. The fusion block test establishes the fusion temperature of glass-ceramic coating compositions, the cone fusion test establishes deformation intervals, the fusion flow test establishes temperature-related hardness and softness of frit, the bead test establishes frit fusibility, fluidity, and surface tension properties, and the interferometer test establishes the expansion coefficient [71].

5.3.1.4 Viscosity

As with all glassy materials, the viscosity property of glass-ceramic coatings is a valid parameter that is strongly influenced by temperature, hence a minor change in temperature can result in a significant change in viscosity. According to **Fig. 5.2**, the T_G temperature is the point at which a substance turns brittle and has a viscosity of 10^{12} N.sec/m^2. The melting temperature was T_S, and the viscosity was 10 N.sec/m^2.

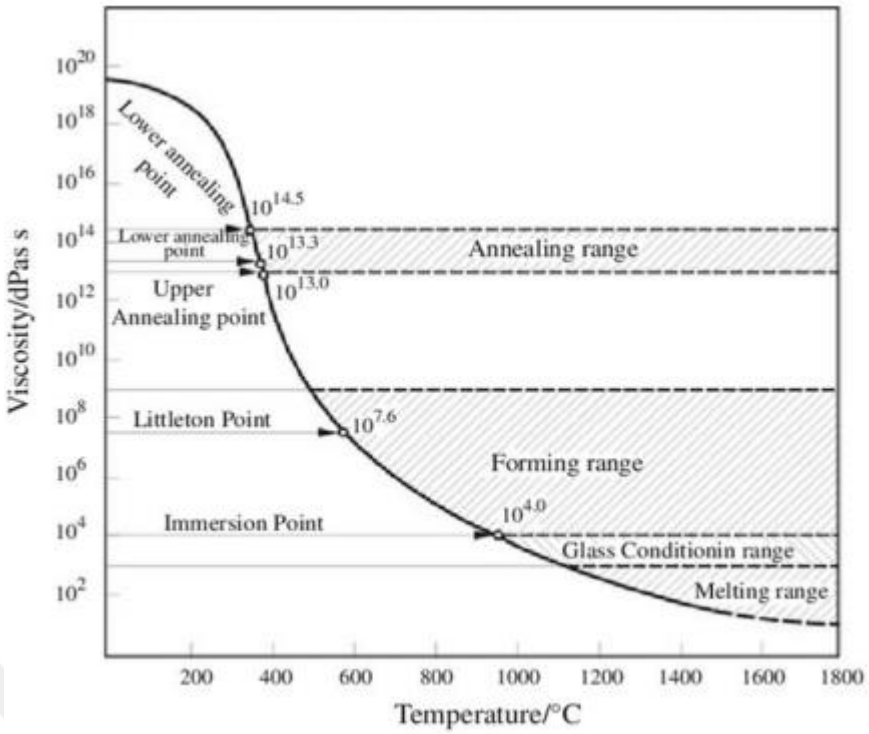


Figure 5.2 Viscosity – Temperature curve for a theoretical glass [73].

These values can be measured by using the chemical composition. The T_G temperature in glass-ceramic coatings is often less than 500 °C, and the T_S temperature is close to 1400 °C. Additionally, as the viscosity increases, the firing temperature of glass-ceramic coatings increases, gas evolution reduces, and surface flatness increases. On the other hand, low viscosity values result in imperfections in glass-ceramic coatings and uneven coating thickness. During the firing process, the viscosity of glass-ceramic coatings ranges between 10^2 and 10^3 N.sec/m^2 [71].

In wet applications of the glass-ceramic coating method, the viscosity values of the created glass-ceramic coating slurry can be easily modified using substances like boric acid, clay, and sodium nitrite [54].

5.3.1.5 Thermal Conductivity

In both scientific and industrial perspectives, the heat conductivity of enamels is a significant characteristic. Heat transmission through enamel in kitchen equipment is a crucial need. As a reflector or emitter, it is a desired quality in military, construction, refrigerator, and oven applications. By adding high thermal conductivity oxides (metal powders) to the mix, enamels' thermal conductivity can be increased [67].

The following formula is use' to compute thermal conductivity, which is the magnitude of the thermal conductivity coefficient:

$$\lambda = p_1 . \lambda_1 + p_2 . \lambda_2 + p_3 . \lambda_3 \quad (5.8)$$

5.3.2 Physical and Mechanical Properties

5.3.2.1 Density

The density (specific gravity) attribute is frequently utilized to regulate the sample's fluidity in wet applications. The density of glass-ceramic coatings should be diluted; this can be done by using a pycnometer to measure the density. The formula to determine the density of glass-ceramic coatings is:

$$S = \frac{(w - p)}{(w - p) - (w_2 - w_1)} \quad (5.9)$$

where S is the specific gravity of glass-ceramic coating, w is the weight of the tapered pycnometer and sample, w1 is the weight of the tapered pycnometer filled with water, and w2 is the weight of the tapered pycnometer, sample, and water, and p is the weight of the tapered pycnometer [70].

5.3.2.2 Specific Heat

Specific heat is the amount of energy needed to raise a gram of material's temperature by one degree Celsius at constant pressure and volume. The following equation can be used to determine the glass-ceramic coating's specific heat [70]:

$$S = p_1 . s_1 + p_2 . s_2 + p_3 . s_3 \ldots \quad (5.10)$$

where S is the specific heat of the glass-ceramic coating, p is the percentage of the oxide and s is the factor for the oxide.

5.3.2.3 Hardness

According to the Mohs scale, the hardness of glass-ceramic coatings ranges from 5 to 6, with minor variation depending on chemical composition. Because they don't provide accurate findings for glass-ceramic coatings, the Rockwell, Brinell, and Knopp hardness measuring techniques are not frequently employed. The Mohs scale is also used to gauge how resistant a glass-ceramic coating is against scratching [70].

5.3.2.4 Elasticity

Although the elasticity is a crucial material characteristic, it is not frequently applied in the field of glass-ceramic coatings. It may be analyzed using mechanical and sonic techniques. The mechanical method's mathematical formula is as follows [70]:

$$A = 4PL^3/bd^3\Delta \tag{5.11}$$

where P is the load, L is the length of the material, b is the width, d is the thickness and Δ is the deflection [70].

5.3.2.5 Compressive Strength

One aspect of glass-ceramic coatings that is commonly disregarded but might have an impact on other features is their compressive strength. It has a value of 77-81 kg/mm^2 for typical glass-ceramic coatings and may be estimated using Winkelmann and Schott's methods [70].

5.3.2.6 Tensile Strength

Tensile strength of glass-ceramic coatings is a crucial characteristic but determining it out can be challenging. Glass-ceramic coated materials are suitable for breaking due to their brittle fracture characteristics. As a result, several methods for studying it have been suggested. It has an effect on the thermal characteristics of glass-ceramic coatings, notably their tensile strength, while not being a desired or explicitly analyzed attribute [70].

5.3.3 Chemical Properties

5.3.3.1 Acid Resistance

In many applications, especially in kitchenware, glass-ceramic coatings are continuously subjected to acid assault. The continuity of the structure [SiO^4] in the glass-ceramic coatings determines the acid resistance of the glass-ceramic coatings, making SiO_2 one of the most significant oxides determining acid resistance. Tetrahedrons made of [SiO_4] are utilized to cover the areas around [AlO_4] – R^+ and [BO_4] – R^+ in the construction to protect them from the corrosive effects of acid. In other words, acid resistance increases as the amount of SiO_2 in the glass-ceramic coatings formula increases. The continuity of the [SiO_4] tetrahedrons is disrupted by ions like Li^+, Na^+, and K^+, which lowers acid resistance as the R_2O group in the structure gets larger [74], [75].

5.3.3.2 Alkali Resistance

Glass-ceramic coatings may potentially be exposed to an alkaline attack depending on the region of application. On the other hand, the alkaline attack proceeds more slowly than the acid attack. Alkali tests on the glass-ceramic coatings endure longer as a consequence. Additionally, the impact of corrosive materials that generate ion exchange leach in the coating structure of the glass-ceramic coatings is lessened as compared to acid and alkaline solutions. It is frequently tested using sodium pyrophosphate, sodium hydroxide, and sodium bicarbonate solutions.

Glass-ceramic coatings undergo an ion exchange leach as a result of the hydrogen ions in the solution reacting with the matrix of the glass-ceramic coatings and causing the alkaline ions to ionize. The most frequent occurrence of this pH-dependent reaction is at pH<9.

Alkaline ions are created when hydrogen ions combine with a silica network in the presence of two non-bridging oxygen atoms. As a result, an aqueous surface layer will occur when any of the alkali metal ions bound by non-bridged oxygen readily replace hydrogen.

At pH > 8, the silicate structure normally starts to dissolve, and as the pH rises, the process continues. At these pH values, the Ohs interact with the glass matrix or hydrated layer. Further interactions of hydroxyl groups with the initial product lead to the creation of Si(OH), the molecules that enter the alkaline solution. Water and the second product, SiO^-, combine to generate the $SiO^- + H_2O \rightarrow Si\text{-}OH + OH^-$ reaction. Glass-ceramic coatings degrade as a result of the recurrent interactions with hydroxyl groups [74].

5.3.3.3 Water Resistance

Glass-ceramic coatings are water-resistant and maintain the structural integrity at room temperature. Hot water has no impact on the coating structure either. However, following continuous exposure to high temperatures and pressures at the site of application, the coating structure starts to deteriorate [74].

Glass-ceramic coatings shall not exceed 8 mg/m^2 after 21 + 21 days (a total of 42 days) of testing, according to tests carried out in accordance with the DIN EN ISO 4753-3 standard. Water resistance is crucial in thermosiphon, valve, and boiler applications [76].

5.4 The Usage Areas of Glass-Ceramic Coatings

Glass-ceramic coatings are used in a wide range of applications, such as water heaters, thermosiphons, boilers, fireplaces, pipelines, silos, and hot water services. They have superior engineering qualities, such as resistance to high temperatures and chemical corrosion, as well as mechanical strength and aesthetic qualities. Glass-ceramic coatings are an essential coating for cookware and kitchenware in addition to these qualities because of their exceptional technical attributes, appealing appearance, and wide range of color possibilities [65], [67], [77].

5.5 Application Methods

There are two different glass-ceramic coating methods: wet and dry. After taking into account the application area, cost, sheet metal qualities, and glass-ceramic properties, the coating procedure is decided.

5.5.1 Spraying Method

By compressing air and spraying glass-ceramic slurry or powder, body metal can receive a spray glass-ceramic coating. The two most popular techniques for spraying glass-ceramic coating are manual spraying and automated machine spraying. Spraying on a machine automatically enables large manufacturing [78].

Spray glass-ceramic coating may be utilized for both flat and indented components. In the manufacturing sector, it is used to cover stove side panels, and kitchenware items including pots and pans, kitchen trays, chassis, doors, bodies, grills, stove plates, and burners. The sprayable glass-ceramic slurry in order to obtain a better atomization effect, glass-ceramic coating in the wet process should be ideal, meaning glass-ceramic suspension big enough to adhere to the metal surface yet tiny enough to flow through the spray nozzles. Batch particles that are bigger than the nozzle diameter may clog the holes, preventing the application of glass ceramics entirely or just intermittently. As a result, operations will become slower and less effective, and there will be uneven coating thickness and a rough coating surface. In addition, considerable care should be taken to ensure that the glass-ceramic surface is of high enough quality after drying and firing to prevent breaking and shrinkage [79].

An important benefit of the spray approach is that glass-ceramic powders that spill over may be reused without sticking to the component. Therefore, it is important to keep

environmental contaminants like dust, oil, and grime out of the cabin where the application is performed [80].

5.5.2 Dipping Method

The simplest and most direct method of glass-ceramic coating is dipping. It is suitable for one-color items. The interior and exterior surfaces of pots and pans are frequently coated with this technique [59].

5.5.3 Electrophoresis Method

The assembly of nanoscale particles into nanostructures and micropatterned thin films, solid oxide fuel cells, structural and functional composites, textured ceramics with crystalline-oriented microstructures, and biocompatible coatings on metal implants are just a few examples of the complex shapes that electrophoretic deposition (EPD) is frequently used.

The most crucial factors determining coating quality in the electrophoresis process are the density and particle size of the glass-ceramic as well as the amount of power used. In this colloidal technique, charged powder particles are suspended in a stable colloidal solution. The depositing electrodes in this solution are the proper shape. The two procedures involved are electrophoresis and deposition. In the first step, known as electrophoresis, charged powder particles move in the direction of an electrode while being influenced by a DC electric field. During deposition, powder particles adhere to the dense mass electrode [81].

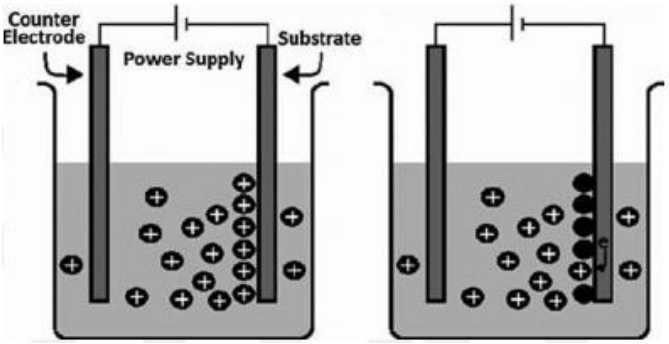


Figure 5.3 Electrophoresis Coating Method [82].

5.5.4 Flow Coating

The modified immersion process utilized in modern business is known as flow coating. The glass-ceramic coated component is not immersed in the mixture throughout this

process. Instead, one or two nozzles are used to apply the mixture to the component that has to be coated. This process is less time-consuming and less expensive than immersion [59].

5.5.5 Thermal Spray Method

A range of coating procedures known as thermal spraying includes depositing molten or semi-molten metallic or non-metallic materials in the finely split form to create a coating. A hot, high-velocity gas jet is used to accelerate and heat powder particles before projecting them as a coating onto a substrate [83], [84].

Some of the techniques employed include plasma spraying, high-velocity oxy-fuel spraying, D-gun spraying, combustion flame spraying, and arc-wire spraying [85].

Van der Waals forces, diffusion bonding, and mechanical bonding take place between the substrate and the molten or semi-molten glass-ceramic particles in this process. The coating thickness varies from 20 micrometers to several millimeters depending on the method and feedstock. The substance is heated via combustion or electrical (plasma or arc) heating (combustion flame). High porosity coatings are a drawback of thermal spraying techniques. It possesses strong adhesion, high hardness and density, and great corrosion, heat, and wear resistance because of the glass-ceramic composition [83].

5.5.6 Powder Electrostatic Application

An electric charge is transferred to dry powder particles in order to apply electrostatic coatings. This approach involves electrostatically charging glass-ceramic powder, which is then sprayed onto the substrate material with an applied voltage of roughly 80–100 kV. The quality of the coating is influenced by the voltage and current supplied by the charging electrode. By altering the voltage settings, the powder can adhere to the substrate material [59], [86].

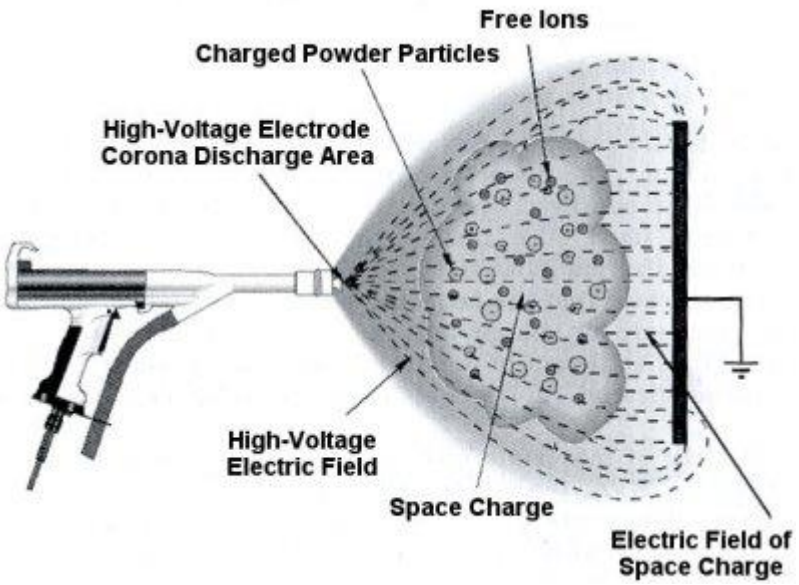


Figure 5.4 Glass-Ceramic Powder Charging in Corona Discharge.

6

EXPERIMENTAL PROCEDURE

In this study, an antifouling evaluation was carried out for glass-ceramic coating systems. Following literature research, a glass-ceramic system was designed to investigate in terms of antifouling behavior. **Figure 6.1** shows all the experimental processes of the study, which has 4 main titles: i) frit preparation, ii) slurry preparation, iii) application, and finally iv) antifouling evaluation. Between the i) and iii) stages, conducted analysis aims to determine the differences after the heat treatment process of glass-ceramic, and between the iii) and iv) stages, conducted analysis proposes to evaluate the AF performance of glass-ceramic coating system.

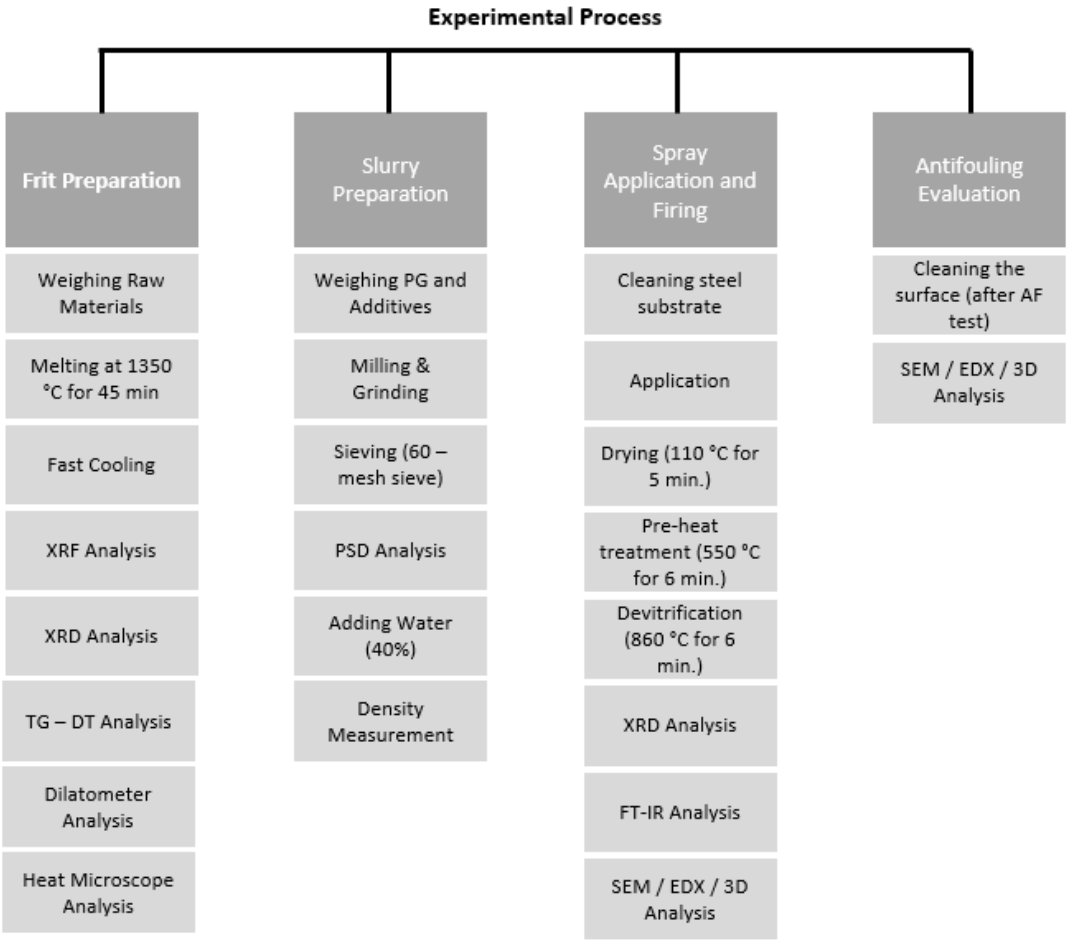


Figure 6.1 The flow chart of experimental process.

6.1 Materials

The required raw materials such as quartz (SiO_2), borax pentahydrate ($Na_2B_4O_7.5H_2O$), soda ($NaHCO_3$) etc., which using in precursor glass' production, and the additives such as clay, boric acid (H_3BO_3), and sodium nitrite($NaNO_2$) were provided by Akcoat Advanced Coating Chemicals & Co. for application process.

6.2 Precursor Glass Preparation

Three different recipes were created for the Seger formulation. The called as anatase based glass ceramic coating (TiBGCC) has anatase crystalline in glassy structure an it was designed to observe whether catalytic affects antifouling performance of coating. Adhesive glass-ceramic coating (AGCC) was designed for 2 objectives, one of them is to provide adhesion between the substrate and the TiBGCC and other one is to observe if catalytic effect is more effective then surface tension when anatase stabilezed in glass-ceramic coating. The last designed glass-ceramic coating was named as alkali resistant glass-ceramic coating (ARGCC) designed to examine the effect of alteration layer on antifouling protection. Shortly, three different comparisons will be made in this study. Whilst in designed first two glass-ceramic coating will give view about if stabilized anatase crystalline has posistive efffect on AF protection, in comparison of whole glass-ceramic coatings will explain the surface tension effect on antifouling protection. An inference will be made about which one is more effective on antifouling protection when catalytic property and tendency to form alteration layer are compared.

After the raw components were weighed and put into corundum pots, the melting process were carried out by melting the pots at 1350 °C for 45 minutes for each batch. After melting, the molten products were poured into water to conduct the quenching process and achieve the frit, precursor glasses, structures. Filtered, the resultant granular frit compositions were then dried for 24 hours at 100 °C. Thus, the dried precursor glass were prepared for the grinding process. The precursor glasses were coded as TiBPG, APG, and ARPG, respectively.

6.3 Precursor Glass's Characterization

6.3.1 Chemical Analysis

The chemical compositions of the precursor glasses' powders were examined via X-Ray Fluorescence analysis (Bruker AXS S8 Tiger, Germany).

6.3.2 Crystalline Structure Analysis

To ensure that the precursor glasses are amorphous and to investigate the effect of heat treatment on precursor glasses were analyzed by X-Ray Diffraction analysis (Bruker D8 Advance USA, Cu Kα radiation, 40 kV, 25 mA, 2θ: 5°- 85° with 0.02° step size).

6.3.3 Thermal Analysis

To determine the thermal behavior of the sample; $T_{Sintering}$, $T_{Softening}$, T_{Sphere}, $T_{HalfSphere}$, and $T_{Melting}$ temperatures precursor glasses were analyzed by heating microscopy (Misura 3.32 ODTH HSM 1600-80, Italy). Thermal properties were examined up to 1250 °C with a heating rate of 10 °C/min due to geometric shape changes according to the DIN 51730 standards.

The coefficient of thermal expansion (COE) was measured for each precursor glass in the range of 20 – 540 °C using a dilatometric device (DIL 402 PC Netzsch, Germany) with fused silica pushrod and sample holder, as well as a Pt–Pt/Rh thermocouple. The heating rate was 10 °C/min. For the preparation of dilatometer analysis, firstly samples were pelleted, devitrified at 860 °C for 6 min., and 5 × 5 × 25 mm piece of devitrified samples were cut to analyze.

Thermal characteristics of precursor glasses were investigated by Simultaneous Thermo Gravimetry Differential Thermal Analysis (TG – DTA Netzsch STA 449F1A-0207-M, Germany). Weight changes were examined by thermogravimetry (TG) and enthalpy changes resulting from exothermic-endothermic reactions of glass-transition, crystallization temperatures etc. were performed by differential thermal analyses (DTA). Simultaneous TG-DTA analyses were conducted on precursor glass by using 30 mg of the frit powders in an alumina crucible heated up to 1200 °C at a constant 10 °C/min in heat flow in N_2 atmosphere.

6.4 Preparation of the Glass-Ceramic Coated Samples

300 g capacity alumina-zirconia ball mills were employed for the milling process. The prepared frit composition was ground in the mill for 12 min. Then, floaters and electrolyte additives were added, and the grinding process was maintained for an additional 3 minutes. **Table 6.2** provides the formula that was utilized in the study. Additives were added in step 2 as a percentage of the total weight milled in step 1.

Table 6.1 The table of milling formula, contents' ratio in % weight, milling time, and size of milled intermediate product of coating.

Step	Role	Material	TiBGCC	AGCC	ARGCC	Milling Time (min)
1	Glass-ceramic coating former	TiBPG	100	-	-	12
		APG	-	70	-	
		ARPG	-	-	100	
	Refratory	Quartz	-	30	-	
2	Floaters	Clay	5	5	5	3
	Electrolytes	Sodium Nitrite	0.25	0.25	0.25	
		Boric Acid	0.25	0.25	0.25	

A 60-mesh (250 µm) sieve is used to filter the powder enamel composition after it has been removed from the mill. 40% (120–150 mL) of the total frit composition's water was then added. To evenly distribute the water and the floats and electrolytes in the water, the mixture was stirred in the mill for two minutes. The mixture was filtered through 60-mesh sieve and obtained suitable slurry was obtained to applicate.

The resulting slurry was applied by wet spraying method to a 360 mm x 130 mm x 5 mm plate of DC06EK grade steel. This piece was subjected to cleaning with an industrial degreaser, then the surface was subjected to hot water rinsing, cold water rinsing, neutralization, and drying steps. A heat treatment procedure was conducted in 3 steps to devitrify the glass-ceramic. In the first step, the plate dried at 100 °C in an oven to evaporate the water inside. Subsequently, the devitrification process was carried out at 550 °C (pre-heating) for 6 min and 860 °C for 6 min in furnaces (Protherm – PLF110/30, Turkey), respectively.

6.5 The Characterization of Glass-Ceramic Coatings

6.5.1 Microstructural Analysis

Scanning electron micsrocopy (SEM) with an energy-dispersive X-ray spectrometer (EDS) attachment was utilized to analyze the surface properties of the glass-ceramic-coated plates, including microstructure, surface morphology, and surface chemical uniformity. The backscatter electron mode (BSE) was employed for SEM and SEM-EDS studies, using a 10 kV acceleration voltage and an 8 mm working distance.

1 cm x 1 cm of coated plates were mounted in a hot bakelite mold (Struers CitoPress, USA) and polished with an automatic polishing method (Struers Tegramin, USA). After the preparation of glass-ceramic-coating samples, SEM (Jeol JSM-6060LV, Japan) analysis was performed to cross-section between the coatings and the steel substrate in the BSE mode and microstructure of the glass ceramic coatings were examined. The adhesion mechanism between glass-ceramic and steel substrate was investigated.

6.5.2 Crystalline Structure Analysis

XRD was used to determine the crystallization, phase analysis, and amorphous structure of glass ceramic coatings. The following procedures were used to create bulk samples of glass-ceramic coatings for XRD analysis to identify the crystalline structure: 15 g of frit and 1 cc of isopropyl alcohol (IPA) were mixed, shaped into pellets under pressure, and pre-heated at 550 ℃ for 6 min and sintered at 860 ℃ for 6 min. After the glass ceramic structures formed, the sinter-crystallized pellets were ground up in order to conduct XRD measurements (Bruker D8 Advance USA, Cu K radiation, 40 kV, 25 mA, 2: 5°- 85° with 0.02° step size).

6.5.3 Chemical Characterization

The prepared coating samples was further characterized using Fourier transform infrared (FTIR) analysis to measure the intensity and the corresponding wavelength range between 400 and 4000 cm^{-1} of resulting infrared adsorption by the samples.

6.5.4 Thickness Measurement

Following wet spray coating and sinter-crystallization to create glass-ceramic coatings in accordance with ISO 2178:2016 standard, the thickness of the coatings were measured using a DeFelsko Positest DFT Combo model coating thickness gage. In order to achieve desirable technical features like adhesion and chemical resistance,

among others, and to preserve these qualities throughout the coatings' macro- and microstructure, coating homogeneity is an important factor.

6.5.5 Adhesion Capability Evaluation

By using an impact resistance test, the adhesion behavior of glass-ceramic coatings may be investigated. According to the BS EN ISO 10209: 2013 standard, adhesion behaviors were assessed by releasing a 1.5 kg, 22 mm diameter cylinder punch from 75 cm onto a glass-ceramic coated steelplate. As a consequence, the standard was used to examine the effects of a 15 kJ energy on the coated surfaces. Following the application of hits, impact marks on the coatings were rated, ranging from 1 (for the best adhesion) to 5 (failed adherence).

6.5.6 Chemical Durability's Evaluation

A cold citric acid resistance test was carried out in accordance with ISO 28706-1 standard to evaluate the glass-ceramic coatings' ability to withstand chemical corrosion. A solution is created by mixing 10 g of citric acid monohydrate ($C_6H_8O_7.H_2O$) with 100 mL of distilled water (H_2O). At room temperature, 4 mL of the solution is poured over the glass-ceramic coating surfaces. The surfaces that had been acid-treated were covered with a cap and let stand for 15 minutes to prevent the solution from evaporating. The plate was then dried and washed with water. To grade the cold citric acid test, a pencil line was drawn over the area where the acid test was conducted. The optimal acid resistance is represented by the test result's AA, whereas a failure is shown by the letter D.

6.5.7 Color Measurement

Color analysis was carried out by using a spectrophotometer (Spectrophotometer CM-700d, Konica Minolta) in accordance with ISO 7724 guidelines and SCE D65 methods. The color values were calculated in terms of L*, a*, and b*. The measured L value corresponds to brightness, the measured a value to chromatic color from red to green and the measured b value to chromatic color from yellow to blue.

6.5.8 Gloss Measurement

Gloss values of coatings were measured in five distinct spots at 60° using the TQC Sheen Polygloss gloss meter instrument. The figures represent the average of five

measurements. A value of 0 indicates the maximum opacity and a value of 90 denotes the maximum brightness of coatings.

6.5.9 Contact Angle and Surface Tension Analysis

The surface tension affects the surface ability to hold fluid and it is calculated using the contact angle value. The wetting angles of the glass-ceramic coating sample were measured with the optical tensiometer (Attention Theta optical tensiometer with One Attention software) using a drop of distilled water of about 5 µl in accordance with the ASTM D7334-08.

6.6 The Evaluation of Glass-Ceramic Coating's Antifouling Performance

The current methodology covers the results of a rapid test for barnacle colonisation in the field by exposure to North Sea water at the beach side of Norderney [87], [88]. This test method is an ideal pre-screening, as it provides results within a few days that are more reliable than laboratory tests, where barnacle larvae are not exposed to competition from larvae of other organisms and as it allows ineffective systems to be screened out more quickly and effective ones to be modified and retested for improvements during the summer season.

For mounting the test panels to the test station, first two 6 mm holes were drilled into the panel – one at the top and one at the bottom. Subsequently, slides with reference coatings were glued to the test panel which has one positive reference and one negative reference. A digital template was built to mark three slide-sized areas on each panels (top, mid, bottom) in which the barnacles will be counted, leading to three analyzable replicates of each coating and reference. During low tide, the panels were exposed at the beach station in the intertidal zone, falling dry for approximately 60 to 90 minutes at every low tide.

After 7 days of exposure, the panels were removed. The photos were prepared by applying the templates and afterwards the barnacles on the marked areas and the slides were counted with the cell counter add-on for Image. The mean and the standard deviation as well as the barnacle density per square centimeter of the replicates have been calculated.

6.6.1 Microstructural Analysis after Antifouling test

To examine in detail the change in micro and macrostructure and, therefore, the impact of biofouling on the glass-ceramic coating structure, SEM and EDS analysis have been conducted.

6.6.2 Surface Cleaning Procedure after Antifouling Test

An alcohol swab was used in a cleaning operation on a specific region of the AF-tested surfaces. One side of the swab was used for each direction as the surface was cleaned in two different ways with a specific number of strokes. How effectively the surface has recovered from the presence of foulants may be used to evaluate a property's ability to be cleaned. Although a level of higher than 70% is considered to be normal and a level of as low as 50% can rarely be achieved, a level of 100% is optimal. Lower numbers are frequently viewed as inadequate.

7

RESULTS & DISCUSSION

7.1 The Results of Precursor Glass Characterization

7.1.1 XRF Analysis

The chemical compositions of the precursor glasses have been given in **Table 7.1**. Whilst SiO_2, TiO_2, B_2O_3, Na_2O, K_2O are the major components, Al_2O_3, P_2O_5, F are minor components, TiBPG. In this composition, TiO_2 is not only used for crystallization agent, but also is used for glass former. Glass-ceramic coatings' precursor glass, applying a steel plate, are devitrificated above 800 °C to provide superior mechanical, chemical and thermal properties with high adhesion quality. To stabilize the anatase crystalline during heat treatment process, the ratios of glass formers and fluxes were optimized in order to increase phase transformation temperature of TiO_2[89][90]. In some processes of the design of precursor glass, crystallization procedure is determined with some additive such as refractories, pigments, etc. APG composition was designed to provide high adhesion property in terms of using ground coat prior to TiBGCC, and it was aimed that high surface tension with quartz additive [91]. The high amount contents of B_2O_3 and fluxes have the capability of surface wettability. Also, the adhesive contents such as NiO and CoO can provide the chemical reaction through Ellingham Diagram with quartz additive [56], [59], [91]. ARPG was designed to achieve resistance to alkaline solutions by using Li_2O, ZrO_2 content with other alkaline components [92]. The presence of CoO and NiO contents will provide the chemical adhesion [56], [59]. Additionally, P_2O_5 can behave a crystallization agent which may form the crystalline phase containing SiO_2, in the high amount of SiO_2 containing glass-ceramic systems [93]..

Table 7.1 The XRF analysis results of TiBPG, APG, ARPG.

Role	Components	TiBPG	APG	ARPG
Glass Formers	SiO_2	45 – 55	40 – 50	60 – 70

Table 7.1 The XRF analysis results of TiBPG, APG, ARPG (continued).

Glass Formers	B_2O_3	8 – 11	15 – 20	3 – 10
Fluxes	Li_2O	12 – 17	15 – 25	13 – 21
	Na_2O			
	K_2O			
Crystallization Agent	TiO_2	15 – 21	-	1 – 5
	ZrO_2	-	-	1 – 5
Adhesive Agents	NiO	-	0.5 – 2	0.1 – 5
	CoO			
Network Modifiers	Al_2O_3	3 – 5	3 – 5	0.1 – 3
	P_2O_5			
Non-oxide Flux	F	0.5 – 2	2.2 – 5	0.1 – 1

7.1.2 XRD Analysis

Fig. 7.1 shows the X-ray diffractometry patterns for precursor glasses from 2θ:10° to 2θ:90°. Whole precursor glasses completely has the amorphous structures, or glassy phases, were thought to be responsible for the large peak between 2θ: 15° and 35°. Since there were no obvious crystalline peaks in the curve, precursor glasses had an amorphous structure and had undergone quality quenching procedures [54].

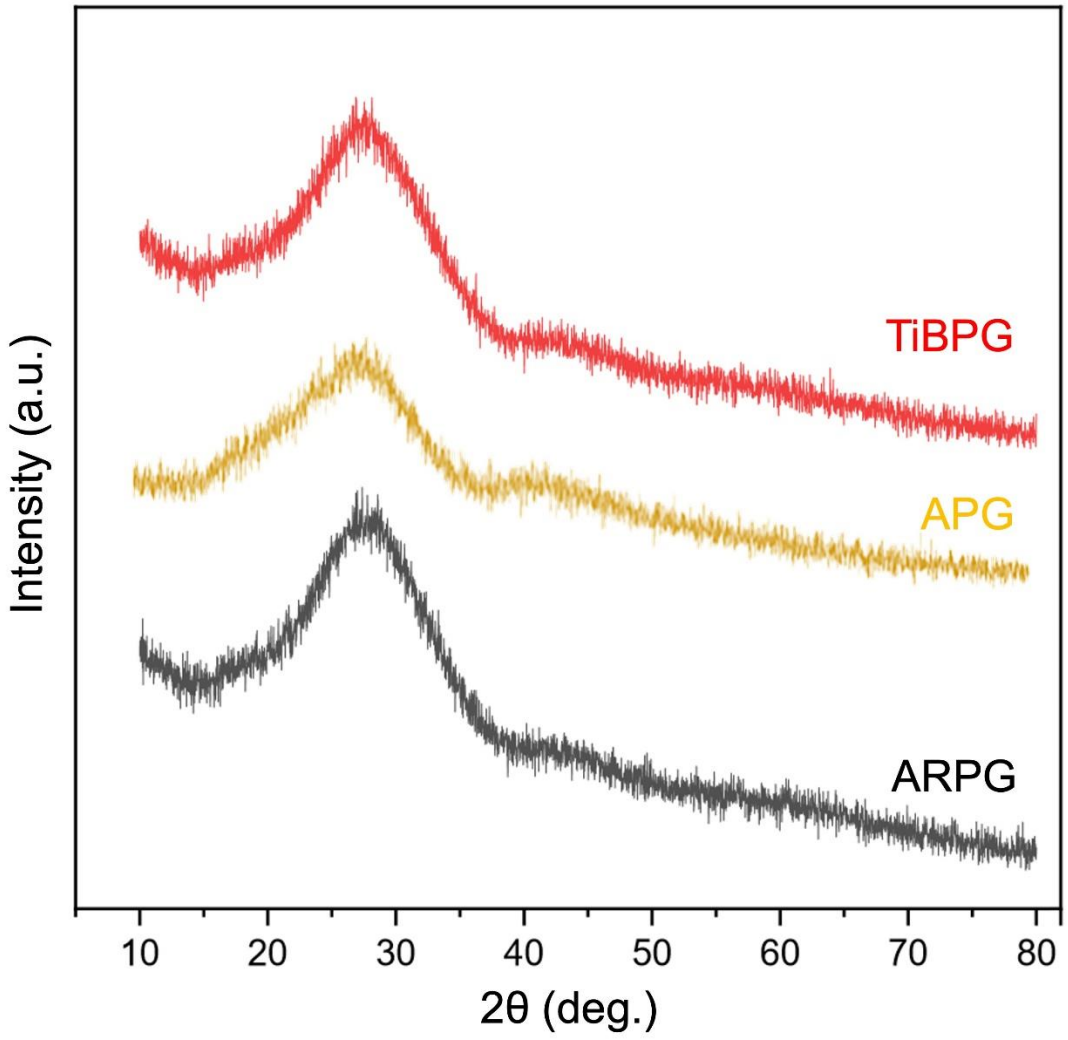


Figure 7.1 XRD analysis's result of precursor glasses.

7.1.3 Thermal Analysis

7.1.3.1 Heat Microscopy Analysis

In order to analyze the thermal behavior of prepared precursor glasses with additives, geometric changes such as the height and width of various temperatures were assessed according to the DIN 51730 standard. Five typical temperatures are provided by heating microscope analysis. The greatest shrinkage when rounded edges appear and the initial shrinkage with a 5% change in size are referred to as sintering ($T_{Sintering}$) and softening ($T_{Softening}$), respectively, as shown in **Fig. 7.2**. The sample's corners are perfectly round, and the spherical point where the first hint of melting emerges is known as the sphere temperature (T_{Sphere}). The half-sphere temperature ($T_{HalfSphere}$) is found at the semi-spherical position where the sample height is equal to half the base width. Melting

temperature ($T_{Melting}$) is defined as the flow point at which the sample melts and shranks to a third of its original height in the hemispheric condition [94], [95].

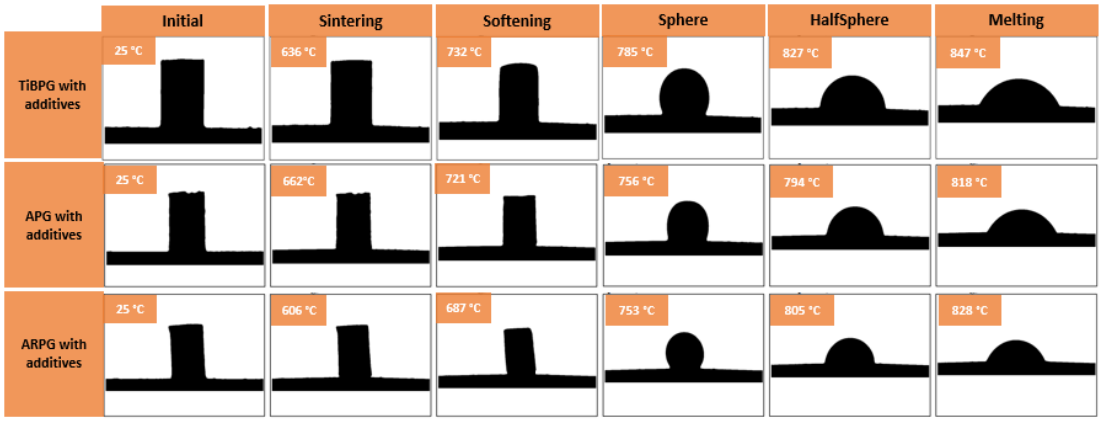


Figure 7.2 The shape images of precursor glasses with additives at different theis characteristic temperatures.

Fig 7.2 and 7.3 demonstrate the characteristic temperatures, $T_{Sintering}$, $T_{Softening}$, T_{Sphere}, $T_{HalfSphere}$, and $T_{Melting}$ of each precursor glass milled with additives. As temperature rises, viscosity drops, allowing the glassy structure to wet the sample's exterior, as shown at softening temperatures. $T_{Sintering}$ represents the first dimensional drop of 5%. $T_{Sintering}$ can be affected by particle size and flux contents. The sintering temperatures, $T_{Sintering}$, of precursor glasses were determined as 636 ˚C, 662 °C, and 606 °C, respectively. Although the APG had high amount of flux contents and low amount of refractory, the sintering temperature observed as the highest value. It was caused by the high amount of quartz additive in its milling formula [96]. Due to the low viscosity of the glass structure, which causes the wetting of the samples' surface, the softening temperatures in this study were determined by observing the round edge of the samples. The shapes of TiBPG and ARPG were more spherical than the shape of APG because of the quartz additive provided higher viscosity at their $T_{Softening}$ [97]. $T_{Softening}$ values were observed as 732 °C, 721 °C, and 687 °C, respectively. $T_{Sintering}$ and $T_{Softening}$ temperatures show high importance on determining bubble dimension of coating after devitrification process. Additionally, the flux oxide effect in the precursor glass chemical composition on the heating behavior was observed more clearly with reaching T_{Sphere} . From this temperature, fluxes play a key role in reaching to $T_{Melting}$. At the points where the shapes became spherical form, in which height is equal to diameter, show T_{Sphere}. T_{Sphere} values were determined as 785 °C, 756 °C, and 753 °C, respectively. The hydrostatic pressure

associated with the density of the liquid phase tries to flatten the shape, whereas surface tension seeks to decrease the surface to a minimum, making a spherical. If the height of the sample equals to the half the width of the base, then the sample reaches the $T_{HalfSphere}$. $T_{HalfSphere}$ values were noted as 827 °C, 794 °C, and 805 °C, respectively. Finally, when the sample's height equals to a third of base, it is understood that the melting starts. 847 °C, 818 °C, and 828 °C were referred to $T_{Melting}$ values of samples [95].

Viscosity continues to diminish when temperature rises over the softening point ($T_{Softening}$), and the glass-ceramic system behaves like a high-density liquid. It is assumed that the coating system's decreasing viscosity accelerates the metal substrate, increasing its wettability. Due to the formation of dendritic structures on the metal substrate, the surface area has grown and may be wetted more readily during the implementation of the adhesion mechanism due to the reduced viscosity. As a result, the glass-ceramic coating and metal substrate interact chemically more quickly and intensely during the adhesion mechanism. This leads to better surface characteristics and adhesion characteristics between the metal substrate and the glass-ceramic coating [98]–[100]. Therefore, the heat-treatment temperature was selected as 860 °C in order to excellent adhesion between the substrat and the glass-ceramic coatings.

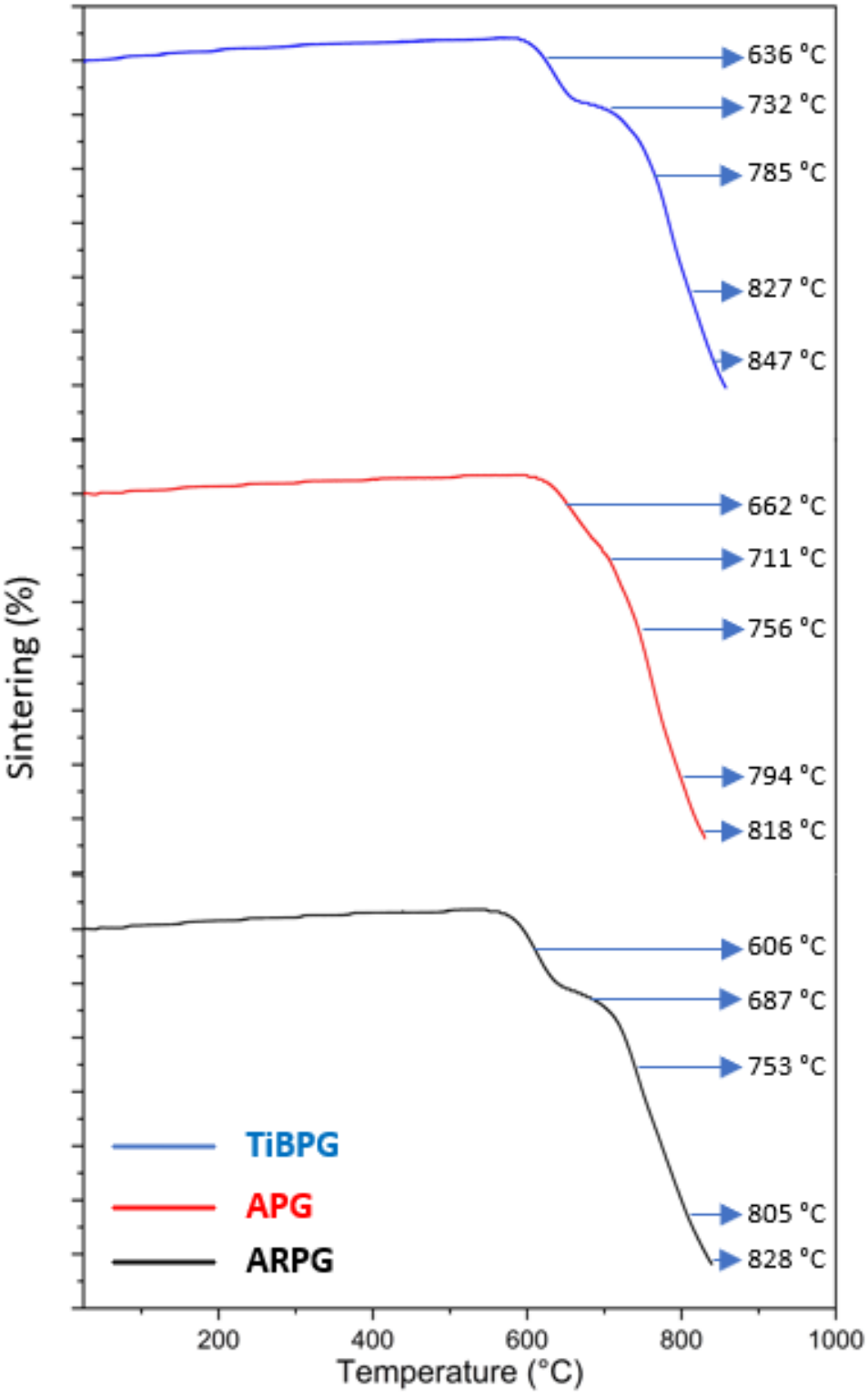


Figure 7.3 Heating microscopy curve of samples.

7.1.3.2 Dilatometric Analysis

Thermal expansion, which occurs when a sample is heated, causes its body length or volume to rise. The percentage increase in length of a material sample as the temperature rises by one degree is defined as the linear coefficient of thermal expansion (COE). The equation below is used to determine the material's linear COE [101].

$$\alpha = \left(\frac{1}{l}\right) x \left(\frac{\Delta l}{\Delta T}\right) \tag{7.1}$$

Volumetric thermal expansion, represented as "," is the term for the change in body volume that occurs when a body is heated by up to 1 °C. The volume COE for isotropic amorphous structures may be well explained by the following equation.

$$\beta = 3\alpha \tag{7.2}$$

The thermal expansion behavior of the precursor glass, or frit, is one of the that determines how well a glass-ceramic coating adheres to a steel substrate. The one of the most important elements to produce glass-ceramic coating without making any mistakes is if the steel substrate's and frits' COEs are very close to each other [101], [102].

Tension-causing fissures in the structure are seen when the glass-ceramic coating's tensile strength is surpassed. Conversely, because the glass-ceramic coating's compressive strength is stronger, only chipping flaws develop when the metal substrate's COE is significantly lower than that of the glass-ceramic. Because it is well known that compressive strength is far more harmful than the tensile strength, the COE of glass-ceramic coatings is always lower than that of metal substrates [70], [101].

Table 7.2 The Cubical Thermal Expansion Coefficient of steel substrate and glass – ceramic coatings.

Material	**Cubical Thermal Expansion Coefficient ($3.\alpha \times 10^{7}$)**	**Temperature Range (°C)**
Low Carbon Steel	465	27 – 760

Table 7.2 The Cubical Thermal Expansion Coefficient of steel substrate and glass – ceramic coatings (continued).

TiBGCC	263	30 – 300
AGCC	324	30 – 300
ARGCC	274	30 – 300

Cubical thermal expansion coeffeicient of glass-ceramic coating samples were calculated and given in **Table 7.2**. TiBGCC has the lowest cubical thermal expansion coefficient value, 263 ($1 / 10^{-7}$. ˚C), and it does not include any adhesive elements. To provide suitable adhesion between the steel substrate and TiBGCC, an adhesive ground coat, carrying adhesive elements and which has higher COE than TiBGCC, is necessary. Thanks to the ground coat, the chemical reactions, achieving the chemical adhesion, can be provided during the devitrification process. In addition, the decreasing COE value towards the outer layer removes the compressive strength, which causes chipping flaws, applied to the surface. Therefore, AGCC was employed as adhesive coat of TiBGCC due to its suitable cubical thermal expansion coefficient, 324 ($1/ 10^{-7}$. °C) and adhesive elemental content [63]. Additionally, ARGCC, 274 ($1 / 10^{-7}$. °C), and AGCC were employed singular coats thanks to their proper cubical thermal expansion coefficient values with elemental contents[70][101].

7.1.3.3 Simultaneous Thermo-Gravimetry Differential Thermal Analysis

The TG – DTA pattern of the TiBPG has been shown in **Fig. 7.4**. Utilizing thermogravimetry analysis, the weight changes of the precursor glass owing to water loss, contaminants removal, etc. with temperature fluctuations were studied (TGA) [103]. To comprehend temperature changes brought on by endothermic-exothermic events including crystallization, breakdown, structural transformations, etc., differential thermal analysis (DTA) was carried out [104], [105].

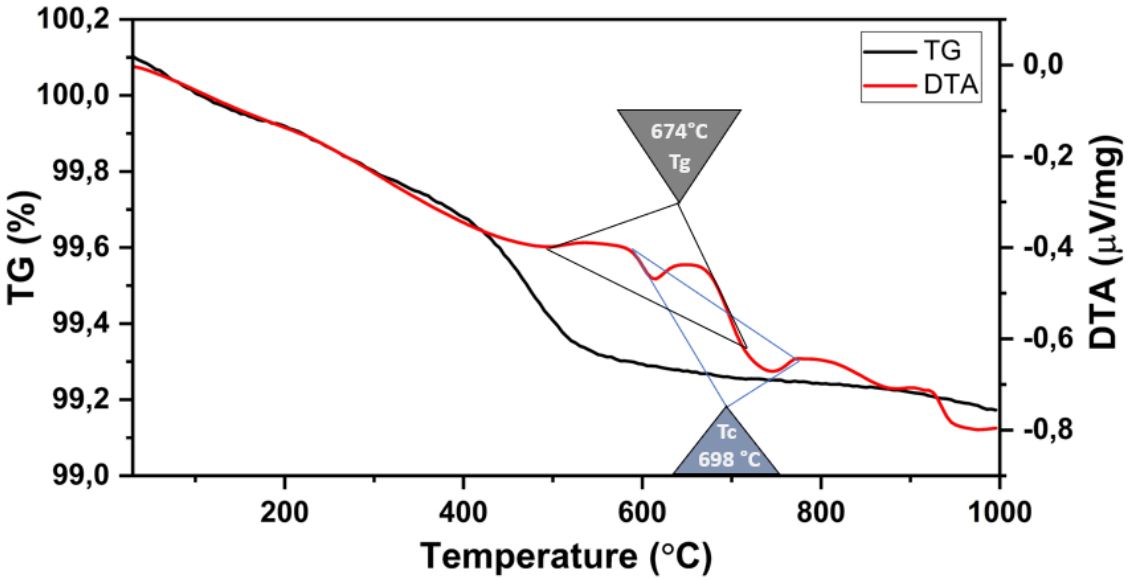


Figure 7.4 The TG – DTA curves of TiBPG.

Although two of exothermic peaks are visible, only the anatase peak was validated by the XRD results. For this reason, the precursor glass was fired for 6 minutes each at 650 °C and 750 °C before XRD examination was carried out. These analyses came to the conclusion that there was just an anatase peak. The exothermic and endothermic peaks of sample were therefore determined to overlap. Triangle was used to identify the dip and the apex. As a result, 674 °C was determined to be the T_g and 698 °C to be the T_c.

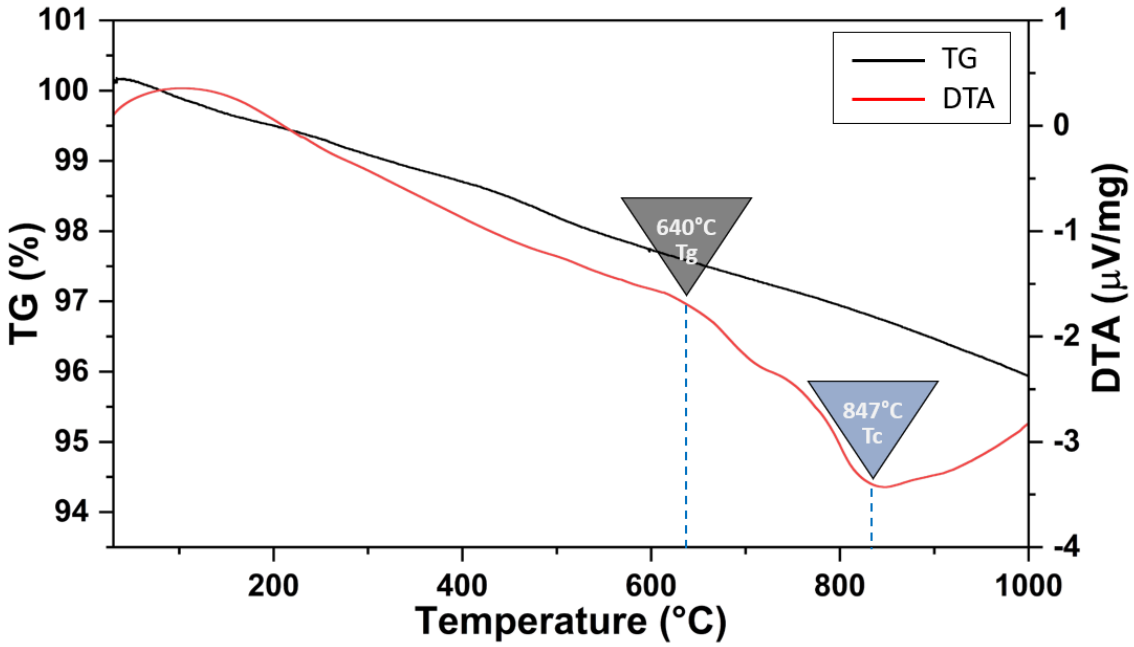


Figure 7.5 The TG – DTA curves of APG.

An endothermic peak at 640 °C and an exothermic peak at 847 °C were observed in DTA curve of APG. Whilst the endothermic peak refers glass transition temperature, the exothermic peak represents the crystalline formation temperature of CaF_2, given in **Fig. 7.5.**

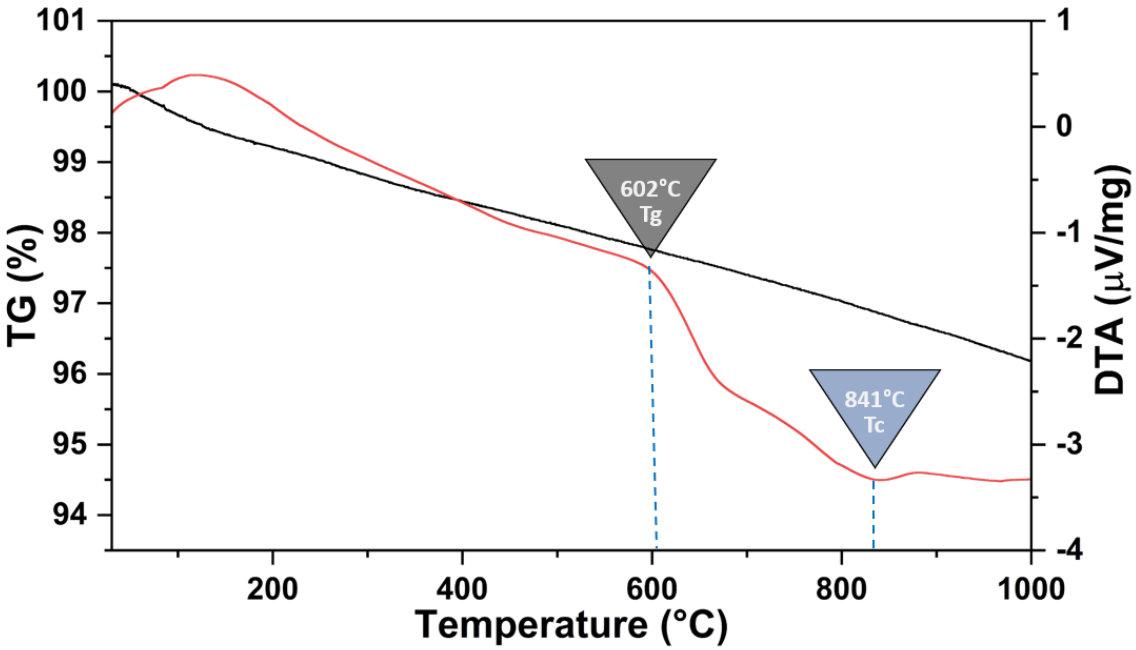


Figure 7.6 The TG – DTA curves of ARPG

In DTA analysis, **given in Fig. 7.6**, of ARPG, an endothermic peak, representing the glass transition temperature, was observed at 602 °C. Also, observed exothermic peak at 841 °C refers to the crystallization temperature of sodium aluminum silicate. The TG curves of both APG and ARPG have not dramatical change.

7.2 The Results of Glass-Ceramic Coating Characterization

7.2.1 Microstructural Analysis

The coating performance is generally affected by cross-sectional area behaviors. Interactions between the metal substrate and glass-ceramic, porosity size and distribution, and coating integrity (no micro-cracks) are the necessities of occurring a high-quality glass-ceramic coatings [106], [107]. After the coating procedure, the glass-ceramic coating have been investigated and shown in **Fig. 7.7, Fig. 7.8, and Fig.7.9.**

Porosity in vitreous enamel coatings can have a significant impact on the performance and durability of the coating. High porosity can lead to reduced strength, increased corrosion and staining, and decreased resistance to thermal shock. Porosity can also affect the appearance of the coating, as the small holes can be visible and may affect the overall color and gloss of the surface. To minimize porosity, proper manufacturing techniques and control of the composition and firing conditions of the enamel are necessary. This can include controlling the particle size and shape of the enamel powders, controlling the firing temperature and atmosphere, and controlling the cooling rate after firing [108].

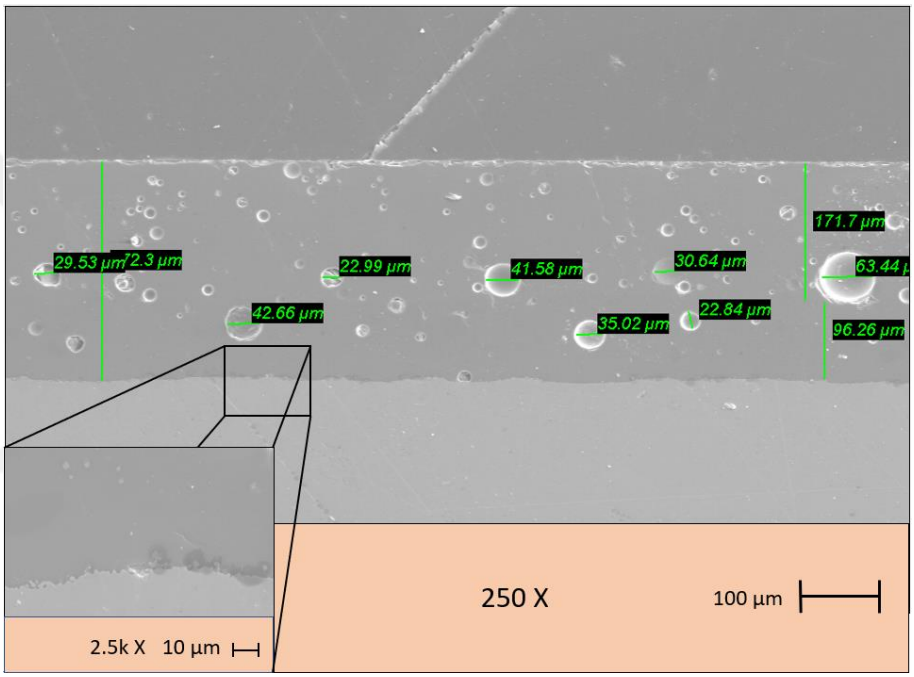


Figure 7.7 Cross-sectional area of TiBGCC.

Dentrites can act as a mechanical interlocking between the coating and the substrate, which improves the adhesion of the coating. They also provide a larger surface area for the coating to adhere to, which increases the bond strength between the coating and the substrate. Additionally, Dentrites can also act as a buffer against thermal expansion mismatch between the coating and the substrate, reducing the risk of cracking [109]–[111].

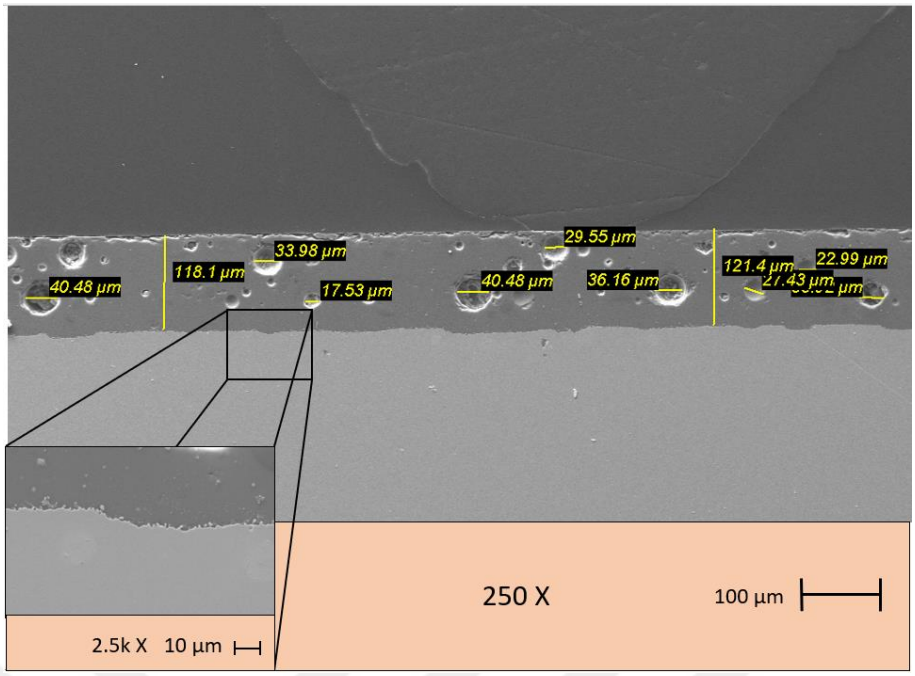


Figure 7.8 Cross-sectional area of AGCC.

At a magnification of 250, the homogeneous distribution and balanced size of porosities, and integrity of the coating structure have been observed from cross-sectional areas of TiBGCC, AGCC, and ARGC. Additionally, the dendritic contents have been seen at 2.5k magnification for each coating, which confirms the high-quality adherence between the glass-ceramic coatings and the metal substrate.

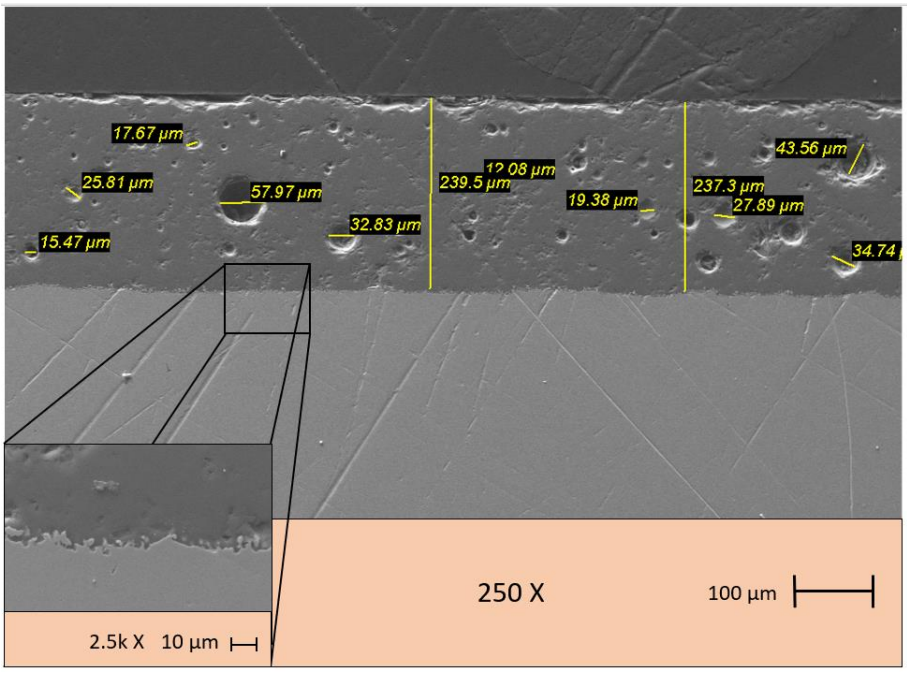


Figure 7.9 Cross-sectional area of ARGCC.

7.2.2 Crystalline Structure Analysis

XRD analysis has been carried out to observe whether any crystalline phase occurs in an amorphous structure of coating samples through heat-treatment processes. **Fig. 7.10** shows the XRD result of TiBGCC. The intrinsic properties of anatase are i) reflactive index is 2.52, ii) dielectric constant is 31, iii) crystal structure is tetragonal, iv) space group is I41/ amd, v) lattice constants are a=b=3784 and c=9515, vii) molecule/cell is 4, viii) volume (A) is 136.25, and ıx) density is 3.79 [112]–[114]. The only TiO_2 anatase, #00-021-1272, phase present in a glass-ceramic coating structure was accomplished by combining a greater ratio of TiO_2 than 15 weight percent with a lower ratio of Na_2O that is lower than 10 weight percent [89]. Rietveld analysis has also been conducted to assess the ratios of both amorphous and crystalline in TiBGCC to understand the **Fig. 7.10** do not show the crystalline phase only . It was observed that the heat-treated glass-ceramic at 86O °C for 6 min, glass-ceramic coating, had 16.37% of anatase phase. Also, the observed exothermic peak in DT analysis and the almost immobile interval of the heating microscope curve, at 698 °C, suggest the crystalline occurring in the system.

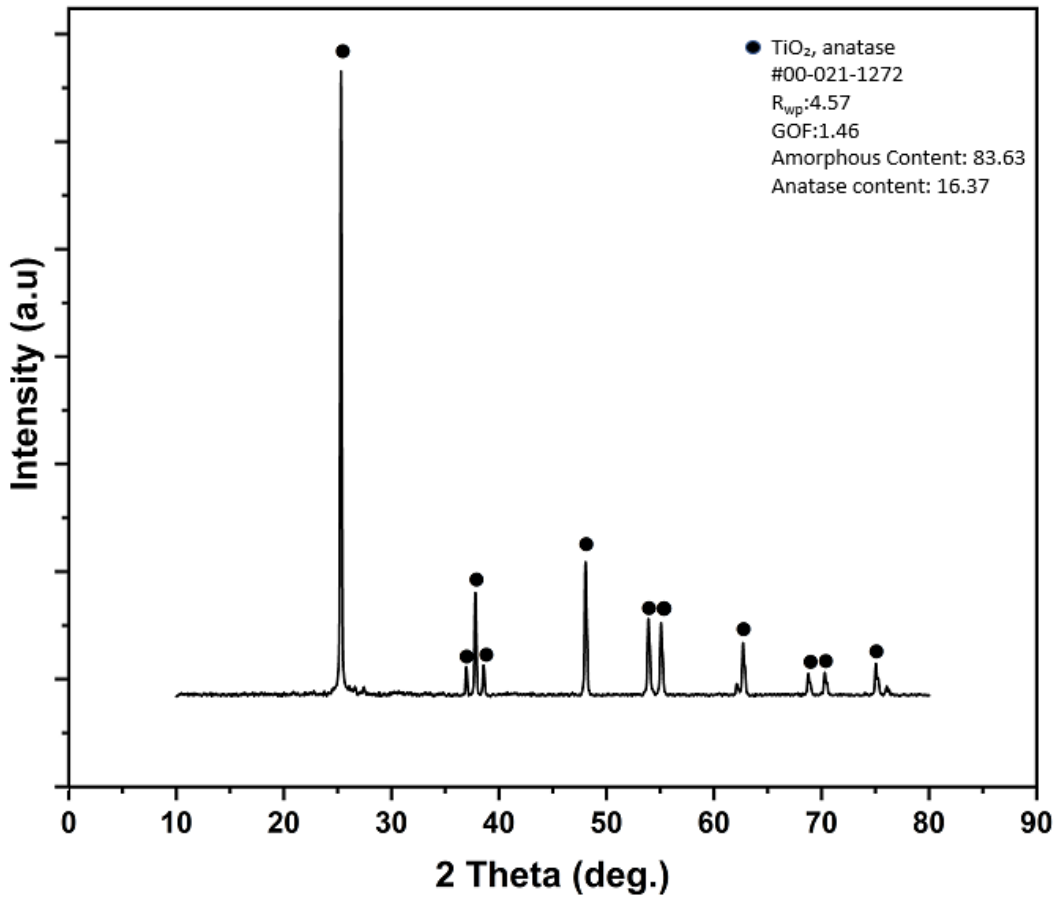


Figure 7.10 Crystalline analysis of TiBGCC.

As with many other metals, titanium is a member of the IVB group of elements and may produce a variety of oxides. There are three common crystalline phases of titanium(IV) dioxide (titanium): rutile, which is thermodynamically stable, and the metastable phases anatase and brookite. Because they are more stable than brookite, anatase and rutile have a wider range of uses.

Titanium (Ti^{4+}) atoms are paired with six oxygen atoms (O^{-2}) to produce "TiO_6" octahedra in all three forms. In contrast to brookite, with its orthorhombic geometry, anatase and rutile have a tetragonal geometry. Rutile has a slightly deformed "TiO_6" octahedron, whereas anatase has significantly distorted octahedral units. In contrast to the anatase polymorph, where each octahedron is in touch with eight neighbors, each octahedron in the rutile structure is surrounded by 10 closely spaced octahedrons. The polymorphs' interatomic distances also differ. The Ti-Ti lengths are longer and the Ti-O distances are shorter for anatase compared to rutile. The two types of TiO_2 have distinct mass densities and electrical band structures as a result of these variations in lattice architectures. The anatase phase is the most attractive for applications due to its inherent characteristics [115].

Because of its low cost, non-toxicity, and strong photocatalytic activity performances, anatase TiO2 is a potential photocatalyst [116]. The disciplines of treatment of wastewater [117], [118], air purification [119] , hydrogen generation [120], dye-sensitized solar cells [121], [122], etc. have all seen extensive application of it. In contrast to other crystallization methods of anatase crystallines, ensuring anatase crystallization within the glass-ceramic body makes the anatase structure more stable following processing at high temperatures. The precursor glass material was chosen as the heat treatment application temperature of 860 °C, for another reason: in addition to optimally wetting the substrate surface, it crystallizes the coating material without occurring the rutile phase, in **Fig. 7.10**, which prevents the anatase phase from becoming unstable [90].

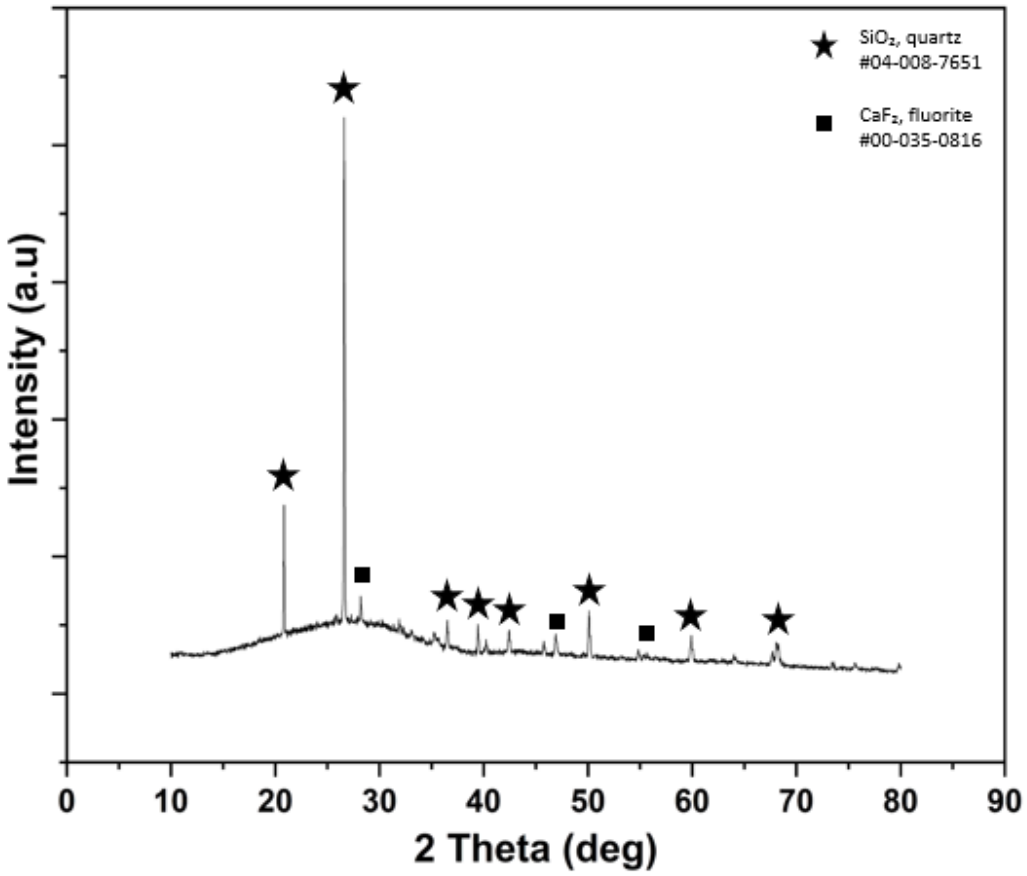


Figure 7.11 Crystalline analysis of AGCC.

The XRD result of AGCC has been demonstrated in **Fig. 7.11**. SiO_2 quartz, #04-008-7651 and CaF_2 fluorite, #00-035-0816, crystalline phases were observed in the amorphous structure. Calcium fluoride crystals are transparent to translucent, with a vitreous luster and a Mohs hardness of 4. They have a cubic crystal structure, and are typically found in cubic, octahedral, or dodecahedral shapes. They have perfect cleavage in four directions, which means that they can be easily split into thin sheets. Calcium fluoride has a high refractive index and a low dispersion, which makes it useful in optical applications such as lenses, prisms, and windows for ultraviolet and infrared spectroscopy. It is also used as a fluxing agent in the production of glasses and ceramics, and as a component in the production of aluminum [123]–[125].

When fluoride compounds are added as a fluxing agent to a mixture of glass or ceramic powders, it reacts with other components in the mixture at high temperatures, forming a liquid phase that allows the powders to fuse together and form a solid mass. As the mixture cools and solidifies, fluoride crystals are formed throughout the glass or

ceramic material. When the Ellingham Diagram for the fluoride compounds are investigated, it has observed that the formation reaction of CaF_2 crystal tends to occur due to the least Gibbs Free Energy value (<-285 ΔG°, Kcal/gfw) for the formation [126], [127].

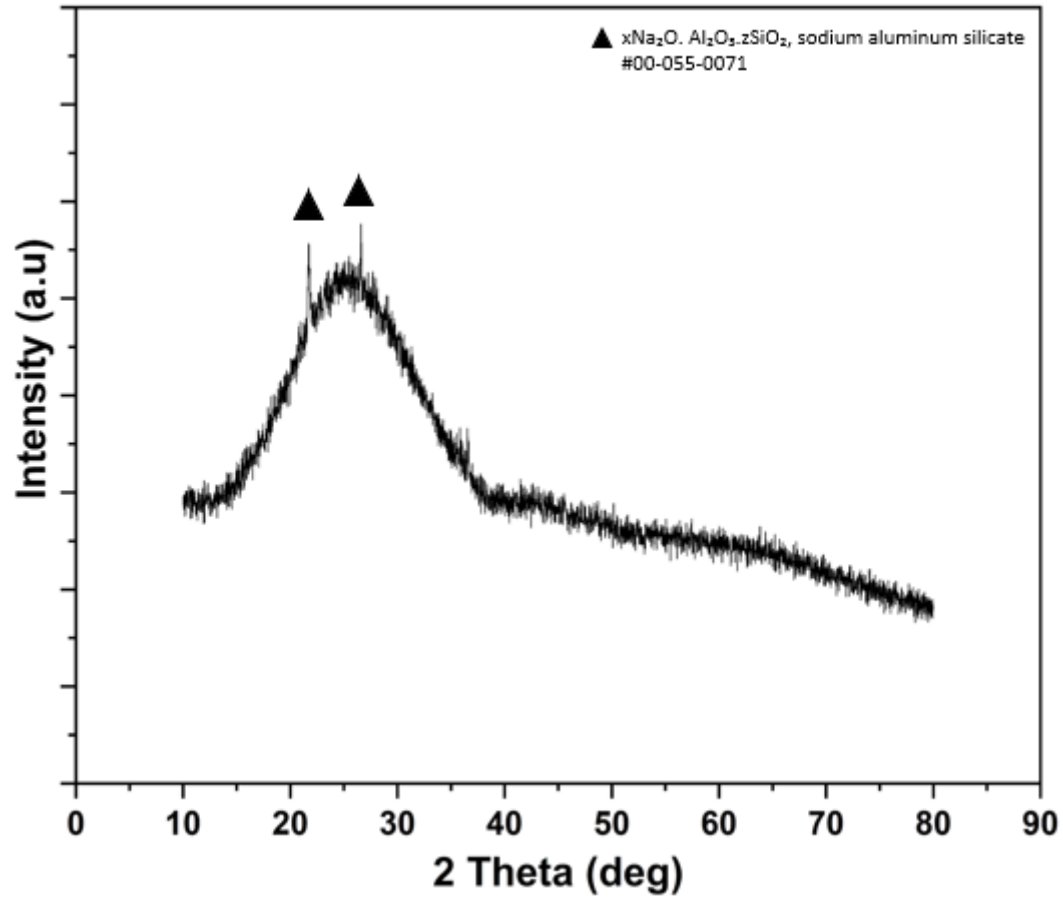


Figure 7.12 Crystalline analysis of ARGCC.

Figure 7.12 shows the crystalline analysis of ARGCC. Sodium aluminum silicate, #00-055-0071, phases were observed in the amorphous structure. Sodium aluminum silicate is a crystal composed of sodium, aluminum, silicon, and oxygen and has a tetragonal crystal structure, a Mohs hardness of 6.5, a density of 2.62 g/cm^3, and is insoluble in water. The formation of sodium aluminum silicate crystals occurs through a process called precipitation. This process involves the combination of dissolved ions in a solution to form a solid crystal [128]–[130].

The formation of sodium aluminum silicate crystals can occur through several mechanisms, including hydrothermal and volcanic processes. In hydrothermal processes, hot fluids rich in dissolved ions such as sodium, aluminum, silicon, and

oxygen, react and precipitate out of solution to form crystals. This process can occur in the deep crust or upper mantle of the Earth. In volcanic processes, sodium aluminum silicate crystals can form as a result of the cooling and solidification of magma or lava. The dissolved ions in the magma or lava react and precipitate out of solution to form crystals as the magma or lava cools and solidifies. Yet in this study, the formation of sodium aluminosilicate crystals occurs through precipitation process, which is the combination of dissolved ions in the glass matrix to form a solid crystal [131]–[133].

7.2.3 IR Analysis

The IR analysis resulst of TiBGCC has been given in **Fig. 7.13**. Ti – O – Ti vibration at both the 421 cm^{-1} and 1396 cm^{-1} have been observed. Additionally, at 996 cm^{-1} wavenumber, there is a B – O – Si vibration.

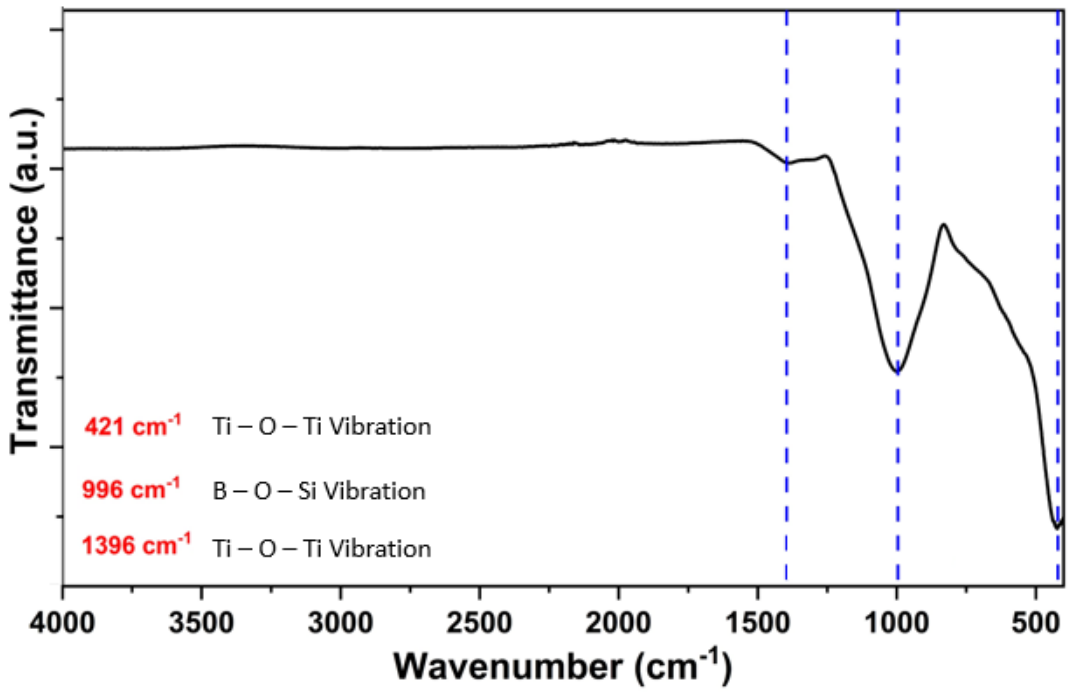


Figure 7.13 The FT-IR analysis result of TiBGCC.

Figure 7.14 demonstrates the IR analysis result of AGCC. The band between 1375 – 1400 cm^{-1} comes from the B-O boroxol ring that comes from the borosilicate structure of the studied glass-ceramic coating [134]. The band located at 970 cm^{-1} is related to the asymmetric Si-O-Si stretching vibration of silicate groups [135]. The band between 775 – 800 cm^{-1} is assigned to the symmetric stretching vibration of O-Si-O [136]. The

spectral band around 700 cm^{-1} is occurred due to the bending of B–O–B linkages [137]. The weak band at 605 cm-1 is assigned to internal vibration of PO_3^{-4} group, and this is due to the low amount of (<1 wt. %) phosphorus oxide in the chemical composition of the studied glass-ceramic coating sample [138].

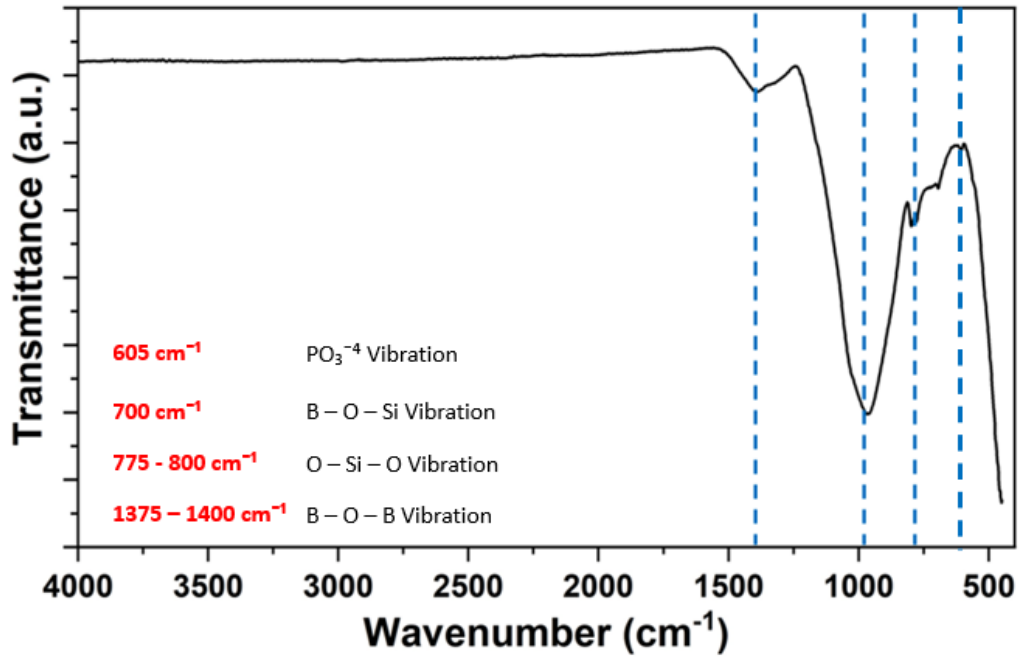


Figure 7.14 The IR analysis result of AGCC.

The IR curve of ARGCC has been given in **Fig. 7.15.** The asymmetric Si-O-Si stretching vibration of silicate groups is connected to the band at 970 cm^{-1} [135]. The band between 775 – 800 cm^{-1} is assigned to the symmetric stretching vibration of O-Si-O [136].

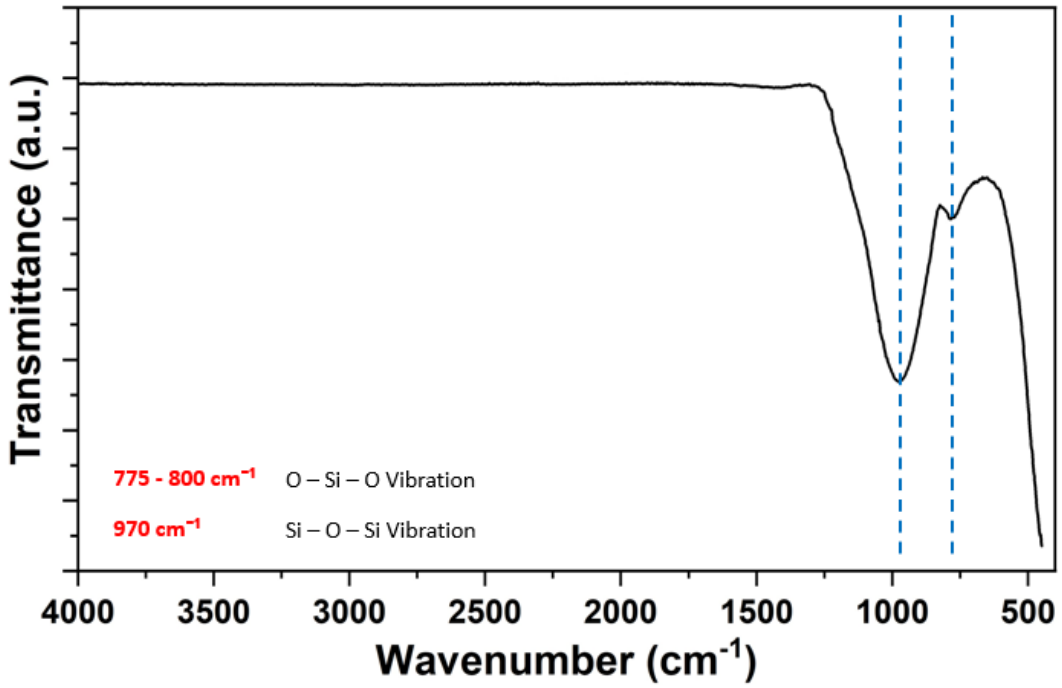


Figure 7.15 The IR analysis result of ARGCC.

7.2.4 Thickness Measurement

Glass-ceramic coating performance is directly affected by its thickness. If the coating thickness is lower than 90-100 µm, engineering performances decrease especially decorative properties. If the thickness of the coating is much more , this will result in a decline in the pavement's porosity output and variability in porosity size and distribution. Unwanted fractures will therefore be seen. Conducted thickness measurement according to the ISO 2178:2016 by DeFelsko Positest DFT Combo demonstrate that the coating thicknesses were suitable for superior engineering properties as given **Table 7.3**.

Table 7.3 Coating thicknesses of TiBGCC, AGCC, and ARGCC.

Sample	Thickness (µm)
TiBGCC	230 – 260
AGCC	120 – 150
ARGCC	210 – 240

Additionally, the SEM image from cross-sectional area of coating, shown in **Fig. 7.7**, **Fig. 7.8**, **Fig. 7.9**, proves the coating thickness is appropriate[139].

7.2.5 The Evaluation of the Adhesion Quality

Adhesion is one of the most important requirements for the glass-ceramic coating process. The first step for a glass-ceramic coating material to show superior engineering properties begins with its adhesion to the metal substrate. The adhesion quality of glass-ceramic coatings were evaluated according to the BS EN ISO 10209: 2013 and the results have been shown in **Table 7.4**. Also, the dendritic content density in the intersection area between the glass-ceramic coating and the metal substrate confirms the high quality of adhesion property [140].

Table 7.4 The results of adhesion evaluations of TiBGCC, AGCC, and ARGCC.

Sample	Grade
TiBGCC	1
AGCC	1
ARGCC	1

7.2.6 The Evaluation of the Chemical Durability

A cold citric acid resistance test was carried out in accordance with ISO 28706-1 standard to evaluate the glass-ceramic coatings' ability to withstand chemical corrosion. A solution is created by mixing 10 g of citric acid monohydrate ($C_6H_8O_7.H_2O$) with 100 mL of distilled water (H_2O). At room temperature, 4 mL of the solution is poured over the glass-ceramic coating surfaces. The surfaces that had been acid-treated were covered with a cap and let to stand for 15 minutes to prevent the solution from evaporating. The plate was then dried and washed with water. To grade the cold citric acid test, a pencil line was drawn over the area where the acid test was conducted [141]. The glass-ceramic coating's performance against to cold citric acid has been presented in **Table 7.5.**

Table 7.5 The resistance performance of TiBGCC, AGCC, and ARGCC against to cold citric acid.

Sample	Grade
TiBGCC	AA
AGCC	A
ARGCC	A

7.2.7 Color Measurement

A spectrophotometer (Spectrophotometer CM-700d, Konica Minolta) was employed to measure the color values in terms of L, a, and b. **Table 7.6** demonstrates the color values of glass-ceramic coatings, where "L" value relates to brightness, "a" value determines the chromatic color from red to green, and the "b" value shows to chromatic color from yellow to blue [142].

Table 7.6 The color values of glass-ceramic coatings.

(SCI D65)	TiBGCC	AGCC	ARGCC
L	94.32	28.02	33.58
a	- 0.69	- 0.58	- 0.66
b	3.13	- 1.21	- 3.23

7.2.8 Gloss Measurement

A glossmeter (TQC Sheen Polygloss) was utilized to measure the glass-ceramic coating's gloss value at 60 °C from five distinct spot of surface. **Table 7.7** gives the gloss measurement from 5 spots and average value of there is 93.2 [143]

Table 7.7 Gloss measurement of glass-ceramic coating.

(GU = 60°C)	TiBGCC	AGCC	ARGCC
Spot-1	93.2	80.2	83.1
Spot-2	92.8	81.1	82.8
Spot-3	93.2	80.2	82.7
Spot-4	93.5	80.4	82.7
Spot-5	93.1	80.1	83.0
Average Value	93.2	80.4	82.9

7.2.9 Contact Angle and Surface Tension Measurement

Hydrophilic surfaces can be useful in antifouling applications because they are less likely to be colonized by marine organisms such as barnacles, algae, and mussels. This is because the high wettability of the surface makes it difficult for these organisms to adhere to the surface and establish a foothold [144].

To examine the effect of hydrophility of surfaces and furthermore impact of surface tension on barnacle settlement, contact angle and surface tension were measured and given in **Table 7.8.**

Table 7.8 Contact angle and surface tension values of glass-ceramic coatings.

Sample	Contact Angle (°)	Surface Tension (mN/m)
TiBGCC	40.79	133.42
AGCC	35.85	322.42

Table 7.8 Contact angle and surface tension values of glass-ceramic coatings (continued).

ARGCC	43.23	95.63

7.3 The Evaluation of Antifouling Performance

Biofouling is an undesirable phenomenon that occurs in engineering surfaces that come into contact with a fluid flow. In summary, this phenomenon leads to energy-fuel consumption, time-wasting and needing of extra manpower due to maintenance requirement, both in industrial applications and maritime transport.

In general, the rate of biofouling on a fluid flow-contact surfaces depends on the amount of nutrients, bacteria, etc. carried by the liquid, the flow rate of the liquid, the stability of the surface against fluid's chemicals, and the temperature. In industrial environments, biofouling is seen as micro pollution, while both micro and macro pollution are observed in the marine environment.

Generally, it is claimed that biofouling is observed with 4 consecutive stages, but sometimes the pore etc. on the surface. Solid surfaces that are suitable for attachment such as can be preferred by short-lived macro-organisms in the absence of a surface to be attached to [14], [24].

The usage of TiO_2 in antifouling coating is receiving more and more attention and numerous research covered a variety of topics, including the development of several TiO_2 based basic antifouling materials, mechanistic research, and toxicity studies on suspended TiO_2. TiO_2 nanofillers might be used in coating resins to address the aforementioned issues with conventional coatings for ship hulls. Additionally, various antifouling coatings based on TiO_2 have been described, including galvanization [145], xerogel [146], and micro-arc oxidation [147] coatings.

The mechanisms underpinning the biocidal actions of TiO_2 particles were studied by Xia et al. [148], Ji et al. [149], and Zhu et al. [150]. It was shown that other biocidal agents' toxicity was increased, growth inhibition, cell inactivation, biochemical alterations, physical effects, and morphological changes occurred. TiO_2 can occupy the growth and even render bacteria inactive. The effects of anatase TiO2 particles on the

marine microalga Nitzschia closterium were studied by Xia et al. [148]. The TiO_2 nanoparticle concentration needed to result in a 50% decrease in growth during a 4-day period was 89 mg/L. Furthermore, even a 5 mg/L dose of TiO2 already significantly reduced growth. Similar testing was done on green algae Chlorella sp. using TiO_2 particles by Ji et al. [149]. TiO_2 nanoparticles (10 nm anatase) were tested on abalone eggs by Zhu et al. [150]. Hatching inhibition and deformity were seen at 10 mg/L, while there was no abnormality at 2 mg/L. Some scientists looked into the biology of TiO_2's biocidal effect on algal cells. There was increased oxidative stress [148]. Researchers found that, in comparison to intracellular reactive oxygen species levels, the extracellular reactive oxygen species production caused by TiO_2 nanoparticles under visible light from the cool fluorescent tube used during experiment was minimal (6%). This showed that enhanced reactive oxygen species levels brought on by ingested TiO_2 nanoparticles were connected to elevated TiO_2 nanotoxicity.

TiO_2 particles' physical properties, such as their crystallinity and particle size, can influence how well they prevent microorganisms from growing. The algicidal effect of TiO_2 particles diminishes with increasing particle size, as demonstrated by Xia et al. [148] and Ji et al. [149], respectively, in the range of 21–400 nm [148] and 5–600 nm [50]. Furthermore, Ji et al. [149] discovered that anatase particles had substantially better biocidal activity than rutile nanoparticles.

To evaluate the antifouling performances of glass-ceramic coatings, a rapid fouling test was chosen, which firstly introduced 18th International Congress on Marine Corrosion and Fouling (ICMCF) in Toulon in 2016 (Daehne et al.2016, Gall et al.2016) [87], [88]. This technique was carried out in North Sea water at Nordeney's beach in July 2021.

Physiochemical parameters may be used to model some biophysical interactions. This is due to the fact that many microorganisms, including bacteria, may be thought of as hydrated colloids [151]. Surface (substrate and organism) hydrophobicity, charge distribution, solution chemistry (i.e., pH and ionic strength), contact angle, and roughness may all have an impact on the physiochemical attachment. The hydrophobicity of most negatively charged cell surfaces changes during the course of a cell's life cycle [151], [152]. Silicate glass surfaces, on the other hand, are often hydrophilic, with the level of the glass's surface hydrophilicity depending on a variety of parameters, including its composition, atomic structure, and exposure circumstances. The contact angle with a surface is sometimes used as a surrogate for that surface's

hydrophobicity [153]. In general, germs stick to hydrophobic surfaces (such metal oxides) more firmly than hydrophilic surfaces (e.g., salts). Additionally, it has been discovered that a bacterium's zeta potential is adversely connected with how much it will stick to glass surfaces. The electric charge of the bacterium at the shear plane is known as the zeta potential. It is frequently used as a stand-in for the surface charge of bacterial cells [151], [153]. Bacterial adherence has been shown to be increased by increased surface roughness and a greater ionic strength in the changing solution. These models have limitations notwithstanding how useful they are for comprehending microbial adhesion to glass. There is now a DLVO (Derjaguin, Landau, Verwey, Overbeek) theory and a thermodynamic model [154], [155]. According to experimental findings, the distribution of active sites is more varied than previously believed, and the models require revision. The ratio of active to inactive surface sites (-Si-OH, -Si-O-Si-, and Si-O-X) for bacterial adhesion can be used to evaluate the degree of such heterogeneity [156]. Variations in an organism's gene expression, which can be brought on by surface contact itself, the hydration/dehydration of the biofilm, and the stiffness of the film, can lead to attachment, expansion, shrinkage, and detachment of a bacterium from a glass surface [157], [158]. When it comes to gene expression, bacteria must first perceive a surface before adhering to it, which causes the expression of numerous crucial genes [159]. Similar controlled gene expression processes have been seen during a microbial community's swarming, growth, and migration on a surface [157]. The consequences of biofilm hydration and dehydration on glass surfaces can be equally complex, and they are frequently confused with the biofilm's viscoelasticity (i.e., stiffness) [160]. However, a biofilm grows as it hydrates, which might put tension stress on an underlying, inorganic surface [161]. A surface may undergo compressive stress when a biofilm compresses due to dehydration. Shear stresses may form as a result of hydration/dehydration if the inorganic surface's mechanical strength changes from one area to the next. In a glass alteration layer, repeated hydration/dehydration cycles can lead to fatigue and perhaps mechanical failure. The speed and scope of this physical modification may be predicted by comparing the viscoelasticity of the biofilm to the surface's strength [162]. Hence, the biofilm formation is not visually inspected in the studied surface. Therefore, surface was examined further microstructural analysis method, SEM and EDS analysis in order to investigate the biofilm formation in micro-levels.

Table 7.9 gives the antifouling test results, which examined in terms of numerical accumulation of barnacles on the 3 different regions of coting sample's surfaces (barnacle/cm^2). An average numbers were also calculated.

Table 7.9 Barnacle attachment ratio in numerical on the glass-ceramic coatings' surfaces.

Sample	**Region-1**	**Region-2**	**Region-3**	**Mean Value**	**Standard Deviation**	**Barnacle Density (n/cm^2)**
Negative Reference	1560	1930	1650	1712	158	86.7
TiBGCC	1494	1488	1396	1459	45	73.9
AGCC	1388	1578	1120	1362	188	68.9
ARGCC	1630	2008	1620	1751	181	88.7
Positive Refence	2	3	4	3	1	0.2

At the end of the test, the tests panel except the positive reference. While the mean number of barnacles on the negative reference (1712), the TiBGCC and AGCC (68.9) were not that densely covered by barnacles, but ARGCC (1751) show similar behavior with negative reference. The mean numbers of barnacles were 1459 on TiBGCC and 1362 on AGCC which are less dense that the negative reference and the mean number

of banacle on ARGCC was 1751. While the barnacles avoided reference panel completely, single barnacles settled on positive reference. For a better comparability, the barnacle density was calculated for the coatings. While positive reference was populated by less than one barnacle per square centimeter (0.2 barnacles/cm^2), the TiBGCC was 73.9 barnacles/cm^2, the AGCC was 68.9 barnacles/cm^2, and the ARGCC was 88.7 barnacle/cm^2. The barnacle population on the negative reference was denser with 86.7 barnacles/cm^2 than TiBGCC and AGCC. The mean values of the negative reference and ARGCC were similar.

TiBGCC showed more consistent settlement of barnacles throughout the panel, leading to standard deviations of 45 which is very little compared to the mean number of barnacles on the panels. The consistent distribution of the settlement on the surface explains the surface tension that can be kept constant across the surface. For comparison, AGCC, ARGCC, and the negative reference had standard deviations of 188, 181, and 158, respectively, which account for roughly 10% of the mean number of barnacles on each of the three mentioned panels. The deviation between the replicates of the panels is considered to be neglectable regarding the evaluability of the outcome.

A relationship between the wettability of surfaces and the raitos of barnacle attachment on the surfaces was established. As measured contact angle values decreases (meaning wettability of surface increase), the settlement capability of barnacles on the surface declines. Whilst AGCC had the lowest contact angle value (35.85°), ARGCC had the highest contact angle value (43.23 °). Also, TiBGCC had the value 40.79 ° of contact angle, see **Table 7.8**. The account done during AF test showed that AF performances were ranked from best to worst as AGCC (68.9 barnacle/cm^2), TiBGCC (73.9 barnacle/cm^2), ARGCC (88.7 barnacle/cm^2). This is because higher wettability of the surface makes it difficult for these organisms to adhere to the surface and establish a foothold.

Since little to none barnacles had settled on positive reference while at the same time, the negative reference was densely populated by barnacles. The results show that the test coatings do not have strong enough antifouling properties to prevent barnacle fouling. Even less favourable subtrates get colonised when there are no more free places for barnacles in the North Sea, which is poor in hard substrates, because the larvae only have a limited lifespan and would otherwise die without settling anywhere [162].

7.3.1 The Result of Microstructural Analysis

Before and after rapid antifouling test, and after surface cleaning procedure, the images from both the surface and the cross-sectional area of samples were taken and sample surfaces were subjected to EDS analysis. It was necessary for the capability to examine any changes in microstructure. In order to comprehend any corrosion to the sea water from glassy structures, coating thicknesses of samples were also studied. EDS mapping analysis from cross-sectional area, before antifouling test and after cleaning procedure, was also conducted to understand whether any diffusion was through to the coating line for each sample.

7.3.1.1 TiBGCC System

The alteration noticed on the surface during the antifouling evaluation has been given in **Fig. 7.16.** The image at top-left represents the visual of surface of TiBGCC before antifouling test. The top-middle image refers to the glass-ceramic coating's surface after the antifouling test.

The images top-left, top-middle and top-right of TiBGCC's surface represent the surfaces before and after antifouling test and after cleaning procedure, respectively, are given in **Fig. 7.16.** The images below show SEM images taken from these surfaces at 250X magnification. Before antifouling test, there are some micro crackings on the surface, but it could be ignored. After antifouling test, although no biofilm occurrence on the surface, barnacle settlement was observed. In literature, bioaccumulation is generally explained by a sequential formation process, but in some areas, such as the North Sea, organisms may be more aggressive because of the few surfaces on which organisms can attach. This rule explains the current situation. Moreover, a cleaning procedure was applied to bio-fouled surface, then biofouling removed from surface. In comparison with the before antifouling and after cleaning procedure, there was no observed any microstructural change on the coating's surface, which means that the coating has easy-to-clean behavior against bio-foulants. The absence of biofilm also supports to this behavior thanks to the absence of extracellular EPS secreted causing by them.

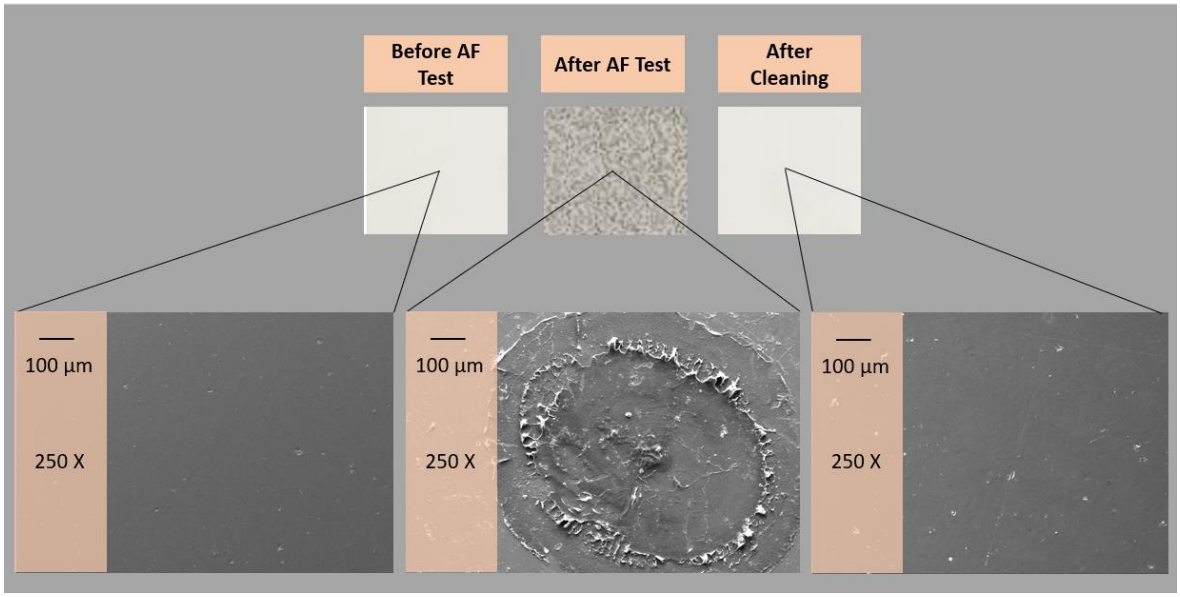


Figure 7.16 The images taken from TiBGCC's surface before and after antifouling test,and after cleaning procedure. (ones on left are before antifouling test, ones on middleare after antifouling test, ones on right are after cleaning procedure.)

EDS analysis was performed on the coated surface before and after the AF test and after cleaning procedure. **Table 7.10** provides the elements distribution, whereas **Fig. 7.17** displays the surface on which the EDS analysis was performed prior to the antifouling test. Also, the **Fig. 7.18** show the surface after antifouling test and specified areas and **Table 7.11** show the EDS analysis' results of these regions. Finally, the **Fig. 7.19** demonstrate the cleaned surface after antifouling and this surface was subjected to EDS analysis. The result of EDS analysis of this surface was given in **Table 7.12.** Carbon ratio assessment is important to analyze whether there is biofilm formation[40]. When the results were compared, a non-significant increase in the C ratio was observed, which explains that the biofilm does not form during test. (see Table 7.5, table 7.6a and Table 7.7) . This can be explained by the shear stresses previously described hydration/dehydration behavior builds on biofilm viscoelasticity [162].

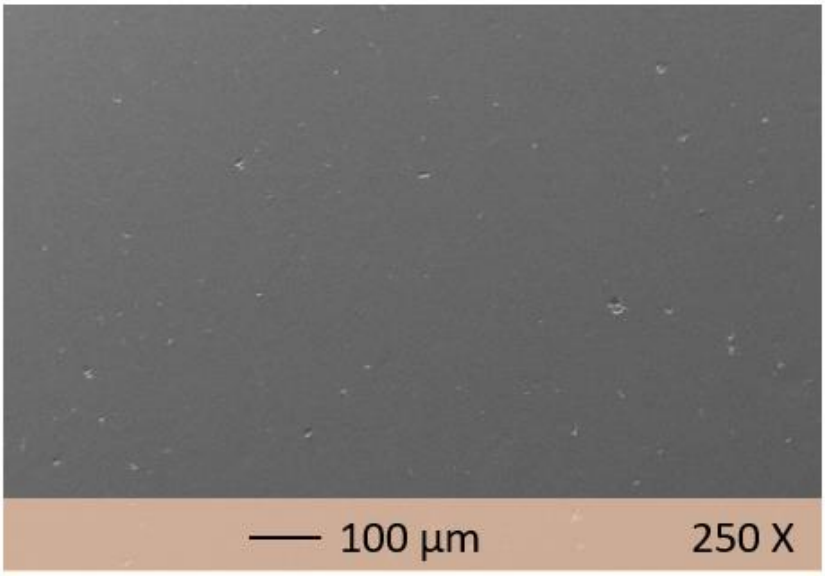


Figure 7.17 The surface on which the EDS analysis was performed before AF test.

Table 7.10 The result of EDS analysis the surface given in **Fig. 7.17**

Element	**Weight (%)**
B K	5.06
C K	3.46
O K	37.53
Na K	6.88
Mg K	0.58
Al K	4.57
Si K	23.83
P K	1.18
K K	6.31
Ti K	8.96
Fe K	1.64

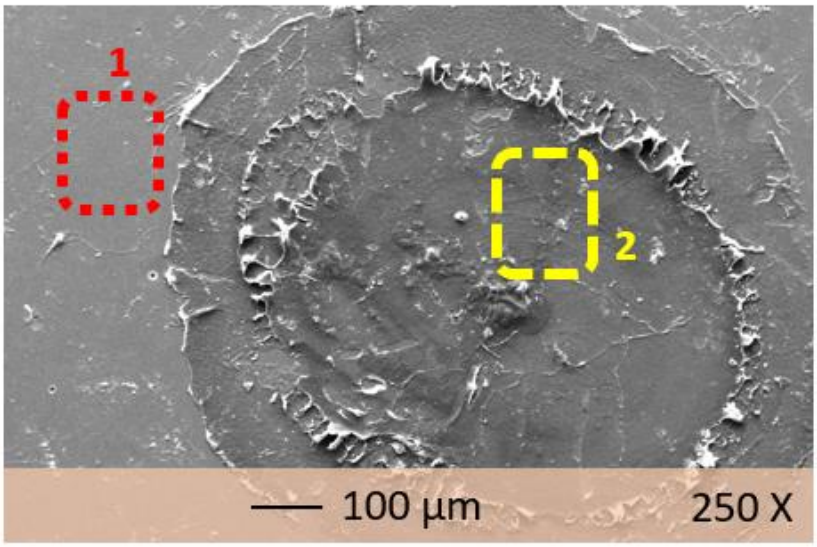


Figure 7.18 The image showing areas where EDS analysis was performed after AF test.

Table 7.11 The results of EDS analysis of Area-1 and Area-2 given in **Fig. 7.18**

Element	**Area – 1 (%)**	**Area – 2 (%)**
B K	5.09	7.17
C K	4.58	39.82
O K	38.67	11.12
Na K	6.66	3.58
Mg K	0.71	0.58
Al K	4.63	3.97
Si K	22.40	19.62
P K	1.13	1.84
K K	5.57	6.29
Ti K	7.55	6.01

Table 7.11 The results of EDS analysis of Area-1 and Area-2 given in **Fig. 7.18** (continued).

Fe K	1.01	0.00

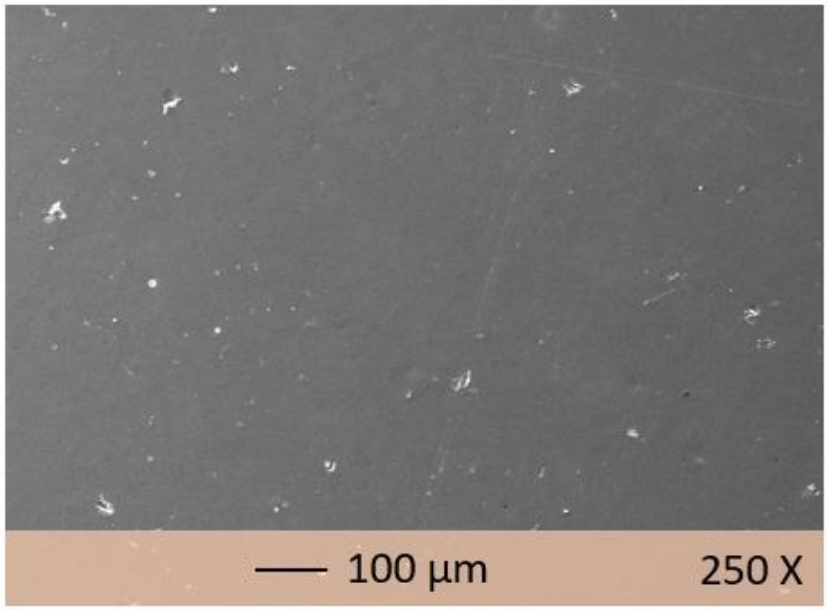


Figure 7.19 The surface on which the EDS analysis was performed after cleaningprocedure.

Table 7.12 The result of EDS analysis the cleaned surface given in **Fig. 7.19.**

Element	**Weight (%)**
B K	4.83
C K	3.97
O K	39.39
Na K	7.05
Mg K	0.57
Al K	5.07

Table 7.12 The result of EDS analysis the cleaned surface given in **Fig. 7.19** (continued).

Si K	24.32
P K	1.25
K K	4.68
Ti K	8.15
Fe K	0.71

The cross-sectional areas were also examined, given in **Fig. 7.20** and **7.21**, to observe whether there is any diffusion through coating or whether there is any corrosion from glass to the sea water by SEM images and EDS mapping analysis.

The ones of left images in **Fig. 7.20** and **Fig. 7.21** demonstrate that coating thickness has not changed during biofouling and cleaning processes, which suggest the absence of corrosion from coating to the sea water.

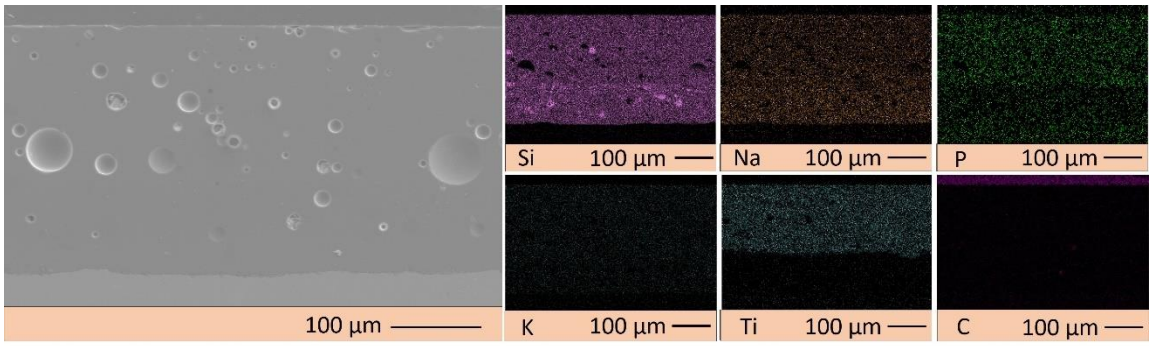


Figure 7.20 EDS mapping analysis from TiBGCC's cross-sectional area before antifouling test.

Also, EDS mapping analysis were conducted for comparison of the elemental alteration in glass-ceramic coating structure. When the C ratio is observed between Fig. 10 and Fig. 11, there is no C diffusion through the coating surface, which demonstrates that barnacles or other microorganisms living in North Sea are not able to spoil the glass structure. For Si, Na, P, K, and Ti, there were not any change, which also suggest the absence of glass corrosion or microorganisms' diffusion through to coating.

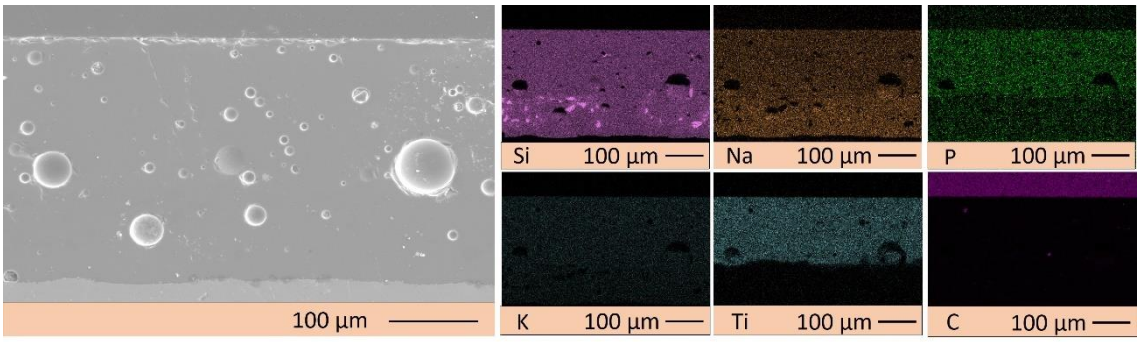


Figure 7.21 EDS mapping analysis from TiBGCC's cross-sectional area after cleaning procedure.

7.3.1.2 AGCC System

Fig. 7.22 shows the alteration noted on the surface during the antifouling evaluation**.** Similar to the result of TiBGCC, the settlement of barnacles was observed on the surface of AGCC during AF test without biofilm formation and after cleaning procedure, there was no barnacle residue on the surface.

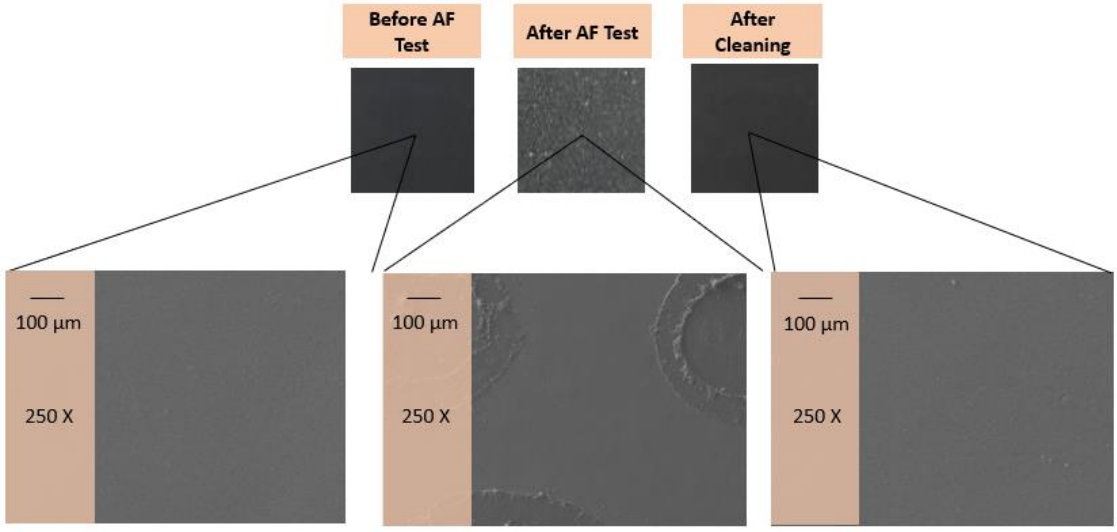


Figure 7.22 The images taken from AGCC's surface before and after antifouling test, andafter cleaning procedure. (ones on left are before antifouling test, ones on middle are after antifouling test, ones on right are after cleaning procedure.)

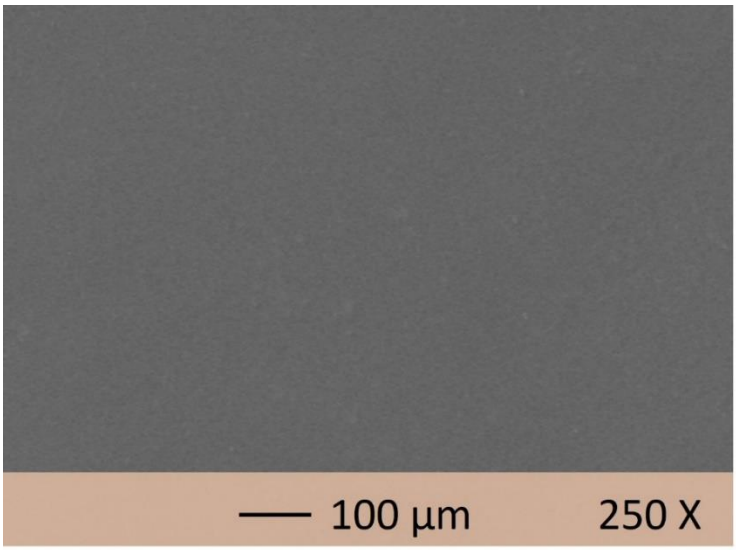


Figure 7.23 The surface on which the EDS analysis was performed before AF test.

To confirm the observation, EDS analysis was conducted through the surface and the results are shown in **Table 7.13**. The highest percentage was actually attributed to the Si, Na, and B other than O elements which shows the glass system of sodium borosilicate structure. The comparison is actually conducted with the C elements which shows just a slight content in the whole structure.

Table 7.13 The result of EDS analysis the before AF test given in **Fig 7.23**.

Element	Weight (%)
B K	8.93
C K	4.34
O K	37.53
F K	0.29
Na K	8.13
Si K	30.06
K K	1.44
Ca K	6.2

Table 7.13 The result of EDS analysis the before AF test given in **Fig 7.23**.

Ti K	2.49
Ni L	0.59

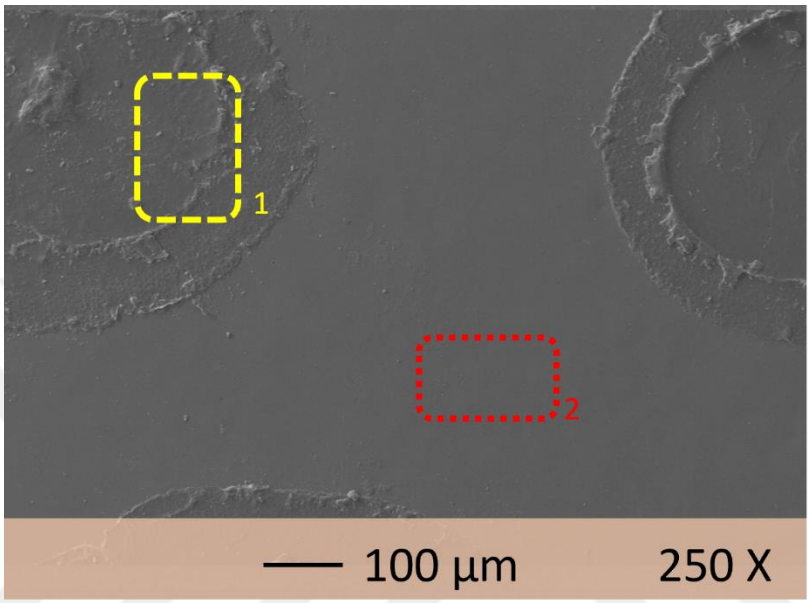


Figure 7.24 The image showing areas where EDS analysis was performed after AF test.

After the antifouling assessment, the SEM analysis shows two distinct areas which are shown as red and yellow areas. The yellow area shows the barnacle adhesion region while the red area shows the glass-ceramic surface. To confirm this assessment, EDS analysis was conducted and the results are demonstrated in **Table 7.14**. According to the EDS analysis of two distinct area, the carbon content shows the biggest change comparing with other elements. The carbon content in the glass-ceramic structure was lower than 5 wt. % before the antifouling test which comes from the organic pollutants during the sample preparation. However, after the antifouling test the yellow area shows bigger than 40 wt. % C content which proves that there is an organic structure on the surface. However the low amount C in the red area which is shown in **Fig. 7.24**, shows that the organic structure was not completely covered the surface. Hence, it was concluded that the biofilm formation did not occur and barnacle attachment was observed in the surface.

Table 7.14 The results of EDS analysis of Area-1 and Area-2 given in **Fig. 7.24**.

Element	**Area – 1 (%)**	**Area – 2 (%)**
B K	4.64	5.48
C K	43.8	3.20
O K	29.25	39.89
F K	0.78	1.29
Na K	4.22	11.32
Si K	10.61	29.35
K K	1.53	1.75
Ca K	4.34	6.71
Ti K	0.31	0.44
Ni L	0.52	0.57

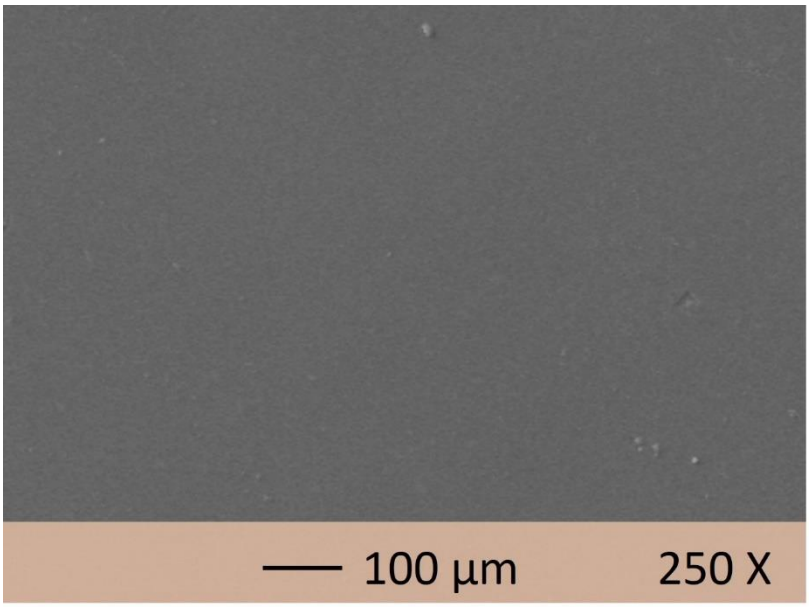


Figure 7.25 The surface on which the EDS analysis was performed after cleaning procedure.

Table 7.15 The result of EDS analysis the cleaned surface given in **Fig. 7.25**.

Element	**Weight (%)**
B K	6.93
C K	3.99
O K	38.44
F K	0.41
Na K	10.33
Si K	30.06
K K	1.21
Ca K	5.75
Ti K	2.21
Ni L	0.67

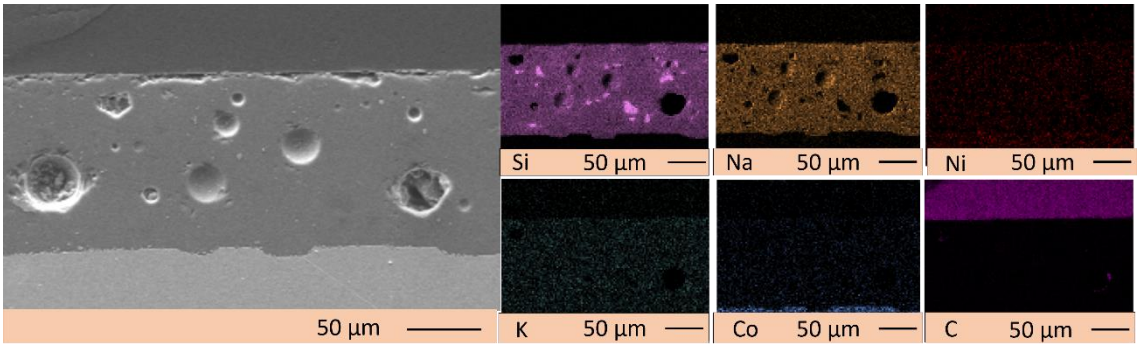


Figure 7.26 EDS mapping analysis from AGCC's cross-sectional area before antifouling test.

The coatig thickness was measure around 120 – 130 µm. The bubble formations inside the coating comes from the gas formation due to the wet spray application. During the devitrification process the gases of CO_2 and H_2O evolves and traps inside the coating structure. Also the H_2 gas comes from the steel substrate and trapped inside the coating[163]. According to the EDS analysis the Si and Na content shows major counting while others show minor. The C content comes from the epoxy resin which was used during the sample preparation for cross-section analysis.

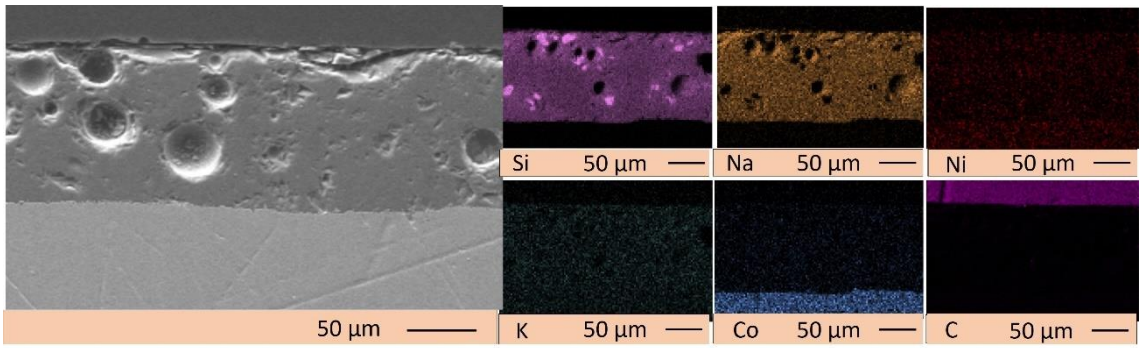


Figure 7.27 EDS mapping analysis from AGCC's cross-sectional area after cleaning procedure.

The SEM and EDS analysis after the antifouling analysis shows similar results with the as-made analysis. The Si and Na content still major components and the C element count is observed only on the top of the coating which comes from the epoxy resin for the sample preparation. Overall, the coating thickness and integrity did not alter after the antifouling analysis.

7.3.1.4 ARGCC System

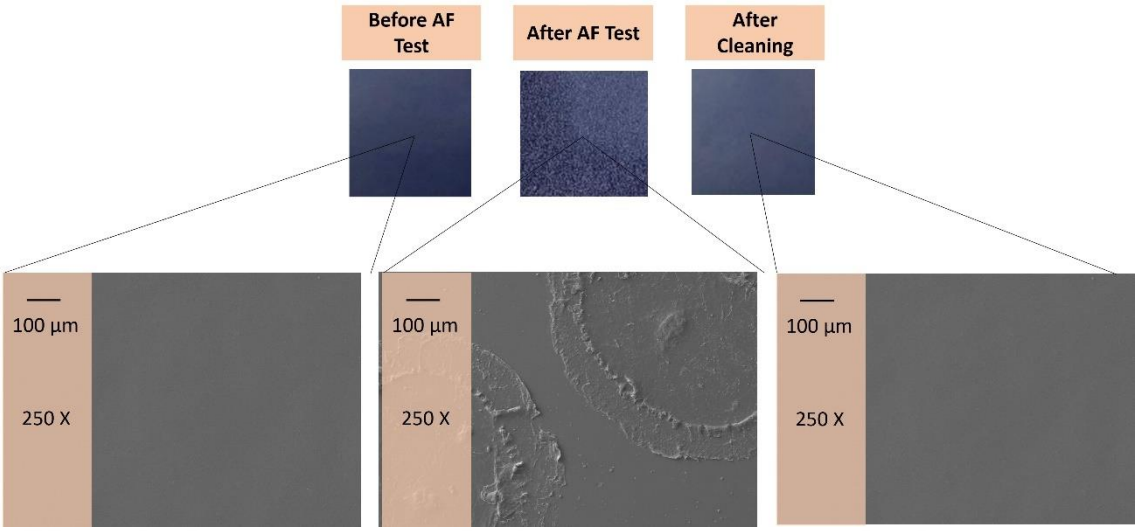


Figure 7.28 The images taken from AGCC's surface before and after antifouling test, and after cleaning procedure. (ones on left are before antifouling test, ones on middle are after antifouling test, ones on right are after cleaning procedure.)

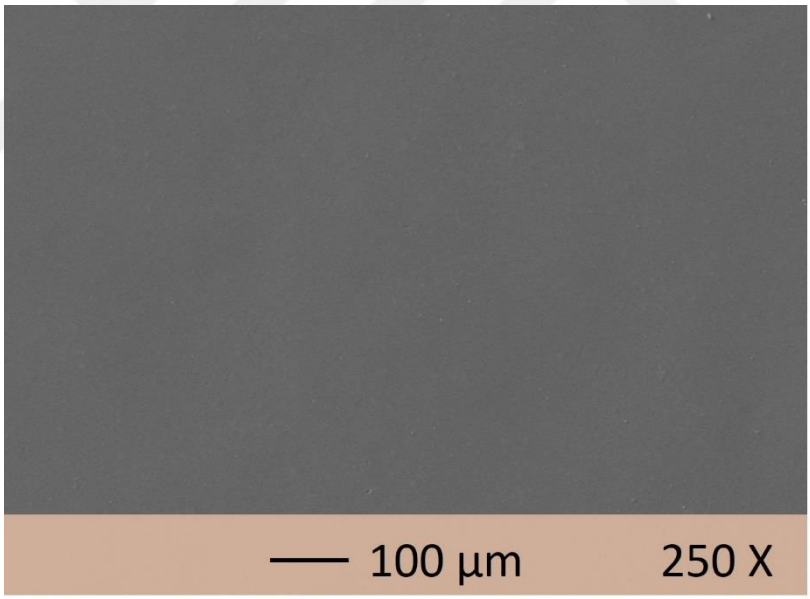


Figure 7.29 The surface on which the EDS analysis was performed before AF test.

The SEM analysis of the ARGCC system shows smooth surface without any defects on the surface. The EDS analysis of the surface is shown in **Table 7.16**. Based on the EDS results, it appears that the glass-ceramic surface is primarily composed of silicon (~31%) and oxygen (~37%). The presence of sodium (~9%), boron (~6%), potassium (~2%), calcium (~2%), and carbon (~1%) suggests that the glass-ceramic material is a

sodium-borosilicate glass-ceramic. The carbon content in the glass-ceramic surface is lower 1% wt. This is a relatively low percentage, and it is likely that the carbon is present as an impurity or trace element in the material. The carbon content is not intentional and it is a residue from the sample preparation method.

Table 7.16 The result of EDS analysis the before AF test given in **Fig 7.29**.

Element	Weight (%)
B K	6.43
C K	3.93
O K	37.52
F K	0.38
Na K	10.06
Al K	1.51
Si K	33.18
K K	2.83
Ca K	3.48
Ni L	0.68

The SEM analysis demonstrates the surface after antifouling testing and according to the EDS analysis provided in **Table 7.17**, yellow area is interpreted as barnacle adhesion region while the red area shows the glass-ceramic surface. The C content in the structure plays a decisive role here. While the C content is high in the barnacle-formed region, the C content is low in the non-formed region. Although the ratio of other elements decreased as a total percentage due to the high C content, similar results were observed.

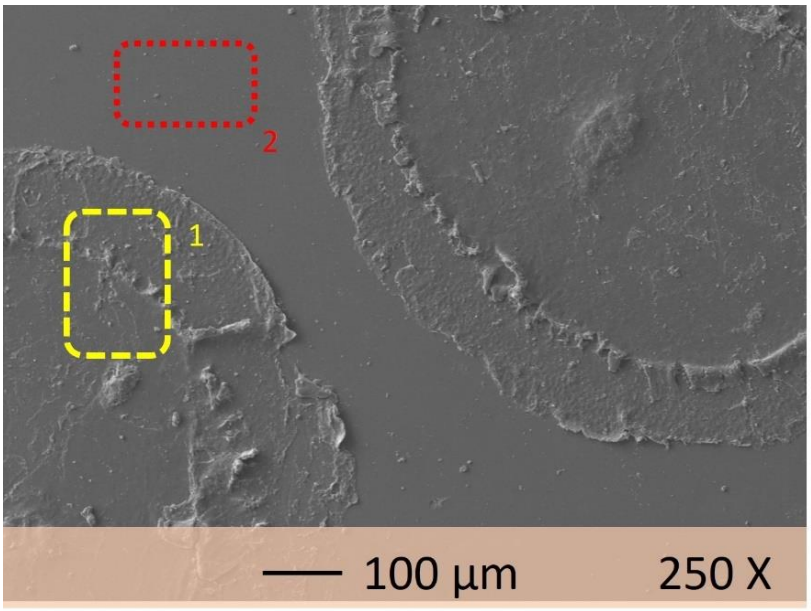


Figure 7.30 The image showing areas where EDS analysis was performed after AF test.

Table 7.17 The results of EDS analysis of Area-1 and Area-2 given in **Fig. 7.30**.

Element	**Area – 1 (%)**	**Area – 2 (%)**
B K	4.45	10.83
C K	35.15	5.21
O K	26.91	35.41
F K	0.44	0.23
Na K	5.41	9.87
Al K	1.08	1.37
Si K	20.41	30.65
K K	3.03	2.97
Ca K	2.35	2.77
Ni L	0.62	0.69

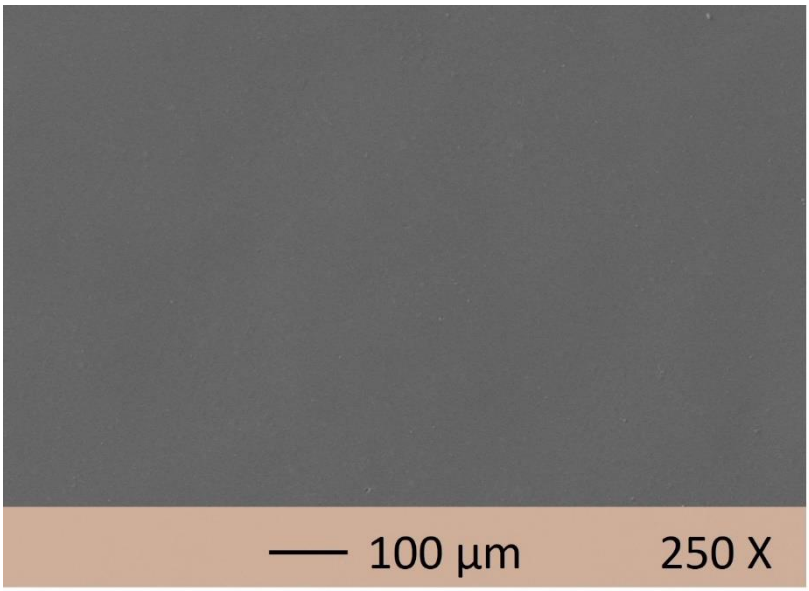


Figure 7.31 The surface on which the EDS analysis was performed after cleaning procedure.

Fig. 7.31 shows the surface after cleaning procedure. After the cleaning process, there is no trace of barnacle formation on the surface. In addition, since the cleaning is a very simple and easy method, the chemical content of the structure has not changed. Morphological examination showed that there was no adhesion or accumulation in the structure, and also no scratches or abrasions due to the cleaning procedure were observed.

Table 7.18 The result of EDS analysis the cleaned surface given in **Fig. 7.31**.

Element	**Weight (%)**
B K	8.43
C K	4.36
O K	36.29
F K	0.41
Na K	11.43
Al K	2.21

Table 7.18 The result of EDS analysis the cleaned surface given in **Fig. 7.31**.

Si K	30.43
K K	2.71
Ca K	3.01
Ni L	0.72

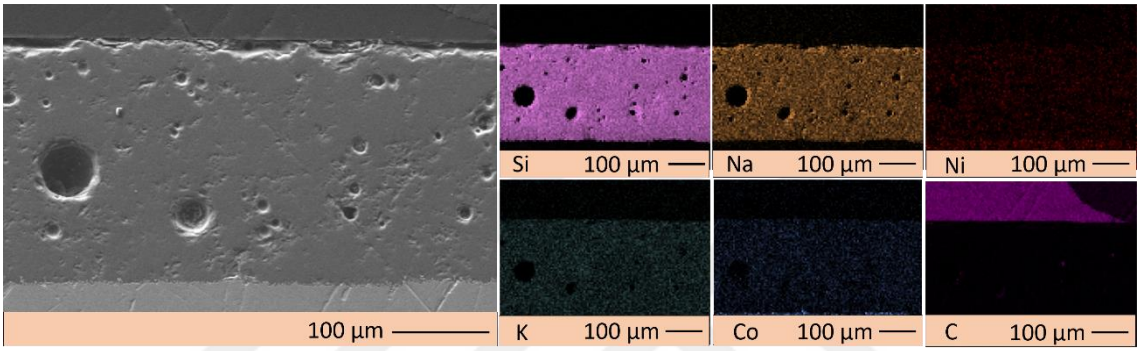


Figure 7.32 EDS mapping analysis from ARGCC's cross-sectional area before antifouling test.

Fig. 7.32 shows the result of cross-sectional SEM and EDS analysis of the sample. As in other glass-ceramic samples, bubble formations were observed in this sample as well. This situation was associated with the formation of water vapor and carbon dioxide gases as in the previous samples, as well as the release of H_2 gases originating from mobility and their entrapment in the structure, together with the steel being raised to a high temperature. As a result of elemental analysis, it was observed that the major count was taken from Si and Na elements. The place where the carbon count is taken is the region where the epoxy resin used during sample preparation is located.

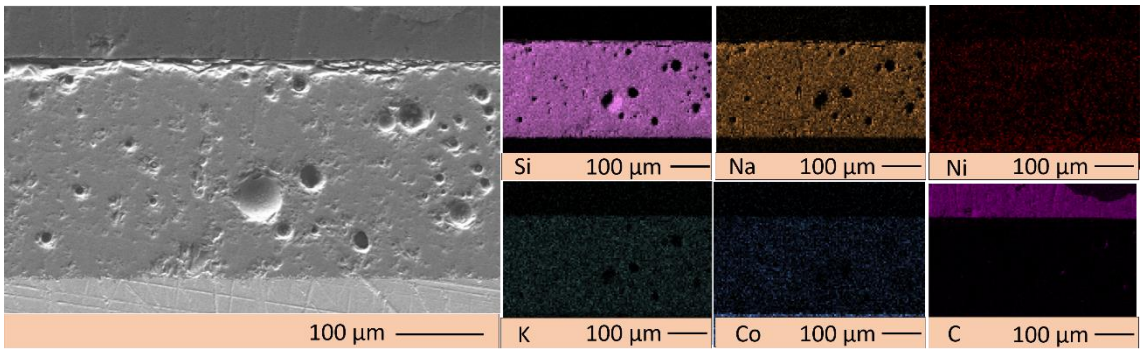


Figure 7.33 EDS mapping analysis from ARGCC's cross-sectional area after cleaning procedure.

The result of SEM and EDS analysis after antifouling analysis is shown in the **Fig. 7.33**. There was no change in the structure within the scope of coating thickness and element count. No mechanical crack formation or progression was observed in the cross-sectional structure. Element count analysis is similar to the results of the EDS analysis before the antifouling test.

7.4 Conclusions and Recommendation

In this study, the antifouling properties of three test coatings (TiBGCC, AGCC, and ARGCC) were evaluated against a positive reference and a negative reference. The results showed that the test coatings did not have strong enough antifouling properties to prevent barnacle fouling, as little to none barnacles had settled on the positive reference while the negative reference was densely populated by barnacles.

In terms of thermal analysis, the thermal behavior of prepared precursor glasses with additives was analyzed by assessing geometric changes such as the height and width of various temperatures according to the DIN 51730 standard. Five typical temperatures were identified and discussed, including sintering ($T_{Sintering}$), softening ($T_{Softening}$), sphere temperature (T_{Sphere}), half-sphere temperature ($T_{HalfSphere}$), and melting temperature ($T_{Melting}$). The study found that as temperature rises, viscosity drops, allowing the glassy structure to wet the sample's exterior. The sintering and softening temperatures were determined to have a significant impact on determining the bubble dimension of coating after devitrification process. Additionally, the flux oxide effect in the precursor glass chemical composition on the heating behavior was observed more clearly with reaching T_{Sphere}. Furthermore, the thermal expansion behavior of the precursor glass was found to

be an important factor in determining how well a glass-ceramic coating adheres to a steel substrate. The heat-treatment temperature was selected as 860 °C in order to achieve excellent adhesion between the substrate and the glass-ceramic coatings.

The microstructural analysis revealed that interactions between the metal substrate and glass-ceramic, porosity size and distribution, and coating integrity are essential for high-quality coatings. Porosity can have a significant impact on the performance and durability of the coating, and proper manufacturing techniques and control of the composition and firing conditions are necessary to minimize it. The cross-sectional areas of TiBGCC, AGCC, and ARGC showed homogeneous distribution and balanced size of porosities, and integrity of the coating structure, which confirms the high-quality adherence between the glass-ceramic coatings and the metal substrate.

The crystalline structure of three types of coatings, TiBGCC, AGCC and ARGCC, were analyzed using XRD analysis. The results showed that the TiBGCC coating had a crystalline anatase phase present, with a percentage of 16.37% after being heat-treated at 860 °C for 6 minutes. Additionally, this method of crystallization within the glass-ceramic body makes the anatase structure more stable following processing at high temperatures. On the other hand, the AGCC coating was found to have crystalline SiO_2 quartz and CaF_2 fluorite phases present in the amorphous structure while ARGCC coating showed sodium aluminum silicate crystal.

The results of the rapid fouling test on glass-ceramic coatings indicate that the TiBGCC and AGCC coatings had lower barnacle densities compared to the negative reference and ARGCC coatings. Specifically, the TiBGCC coating had a density of 73.9 barnacles per square centimeter, the AGCC coating had a density of 68.9 barnacles per square centimeter, and the ARGCC coating had a density of 88.7 barnacles per square centimeter. The negative reference had a density of 86.7 barnacles per square centimeter, which was similar to the ARGCC coating. The positive reference had a very low barnacle density of 0.2 barnacles per square centimeter. These results suggest that the TiBGCC and AGCC coatings may have better antifouling properties compared to the other coatings tested. In the comparison with these two coatings, while TiBGCC stands out in terms of consistent settlement of barnacle, AGCC stands out for being more wettable. Although the AGCC had less barnacle attachment on average, one region held more barnacle than the negative reference when looking at regional data.

Moreover, TiBGCC had less barnacle settlement in each region than the negative reference had.

As a result of this study, glass-ceramic coatings were achieved with 4 main findings: i) glass-ceramic coatings did not show any biofilm accumulation on its surface owing to the glass matrix together with their wettability ability, ii) macro-foulants, barnacles, could attach the coatings' surface, iii) any diffusion was not observed through the internal surface of coatings according to the EDS and SEM analyses and iv) barnacles could be removes from 88.7 barnacle/cm^2 to 0 barnacle/cm^2. The study also found a relationship between the wettability of surfaces and the ratio of barnacle attachment on the surfaces. As the measured contact angle values decreased (meaning the wettability of the surface increased), the settlement capability of barnacles on the surface decreased. The coating with the lowest contact angle value, AGCC, had the best antifouling performance, while the coating with the highest contact angle value, ARGCC, had the worst antifouling performance. In addition, this study found that the test coating TiBGCC showed more consistent settlement of barnacles throughout the panel, leading to a lower standard deviation compared to the other test coatings and the negative reference. The deviation between the replicates of the panels was considered to be neglectable regarding the evaluability of the outcome.

In conclusion, this study has demonstrated the potential of glass-ceramic coatings as a solution for preventing biofouling in industrial and marine settings. The results of the study have shown that glass-ceramic coatings are able to effectively prevent the accumulation of biofilm on their surface, resist attachment by macro-foulants, and maintain their integrity through cleaning procedures.

The lack of biofilm accumulation on the surface of the glass-ceramic coatings is particularly noteworthy as biofilm formation is a critical step in the biofouling process. Biofilms are communities of microorganisms that adhere to surfaces and form a protective matrix of extracellular polymeric substances (EPS). The EPS matrix provides a suitable environment for the growth and survival of microorganisms, and it also protects them from physical and chemical stress. As a result, biofilms are more resistant to cleaning and biocide treatments than free-living microorganisms. Additionally, biofilms can act as a source of inoculum for the fouling of new surfaces, leading to an acceleration of the biofouling process. Therefore, preventing biofilm formation can have a significant impact on the rate and severity of biofouling.

Furthermore, the results of this study have also shown that the glass-ceramic coatings were able to resist attachment by macro-foulants such as barnacles. Although barnacles could attach the coating surface in a certain count, this result is still promising as barnacles are known to be particularly aggressive fouling organisms.

In addition, the study has also shown that the glass-ceramic coatings were able to maintain their integrity during cleaning procedures. The lack of diffusion observed through the internal surface of the coating and the preservation of the coating's thickness and elemental composition suggest that the coatings could have a long service life.

However, it is also important to note that the barnacles could attach the coating surface in a certain count, and optimization of surface energy is required for marine ecosystem applications.

Overall, this study suggests that glass-ceramic coatings are strong candidates for environmentally friendly and long-service life antifouling applications, and that further research in this area could lead to even more effective solutions for preventing biofouling.

Future research could focus on optimizing the surface energy and the tube radius, flow rate for different industrial applications and marine ecosystem. Additionally, further studies could explore the coatings' performance over a longer period of time to confirm their long-term effectiveness. The findings of this study can also be used as a starting point for the development of other types of antifouling coatings that incorporate glass-ceramic materials, for an even more efficient solution for preventing biofouling in different industrial and marine settings.

REFERENCES

[1] M. D. Nguyen *et al.*, "Anti-fouling ceramic coating for improving the energy efficiency of steel boiler systems," *Coatings*, 2018, doi: 10.3390/COATINGS8100353.

[2] J. Wang, Y. Yuan, Z. Chi, and G. Zhang, "Development and application of anti-fouling ceramic coating for high-sodium coal-fired boilers," *J. Energy Inst.*, 2018, doi: 10.1016/j.joei.2017.08.003.

[3] Moore N.L., Garrett-Price B.A., Smith S.A., and Watts R.L., "Industrial Fouling: Problem Characterization, Economic Assessment, and Review of Prevention, Mitigation, and Accommodation Techniques," Feb. 1984, doi: 10.13140/RG.2.1.2131.6086.

[4] P. Vijaysai *et al.*, "Predictive performance assessment of heat exchangers for proactive remediation," 2006, doi: 10.1109/ICIT.2006.372718.

[5] Garcia Sergio and Trueba Alfredo, "Fouling in Heat Exchangers," *IntechOpen*, 2019, doi: 10.5772/intechopen.88079.

[6] W. Faes *et al.*, "Corrosion and corrosion prevention in heat exchangers," *Corros. Rev.*, vol. 37, no. 2, pp. 131–155, Apr. 2019, doi: 10.1515/CORRREV-2018-0054.

[7] W. Faes, J. Van Bael, S. Lecompte, K. Verbeken, and M. De Paepe, "Optimization of heat exchanger design taking corrosion into account," *Therm. Sci. Eng. Prog.*, vol. 30, p. 101277, May 2022, doi: 10.1016/J.TSEP.2022.101277.

[8] P. Pronk, C. A. Infante Ferreira, and G. J. Witkamp, "Mitigation of ice crystallization fouling in stationary and circulating liquid–solid fluidized bed heat exchangers," *Int. J. Heat Mass Transf.*, vol. 53, no. 1–3, pp. 403–411, Jan. 2010, doi: 10.1016/J.IJHEATMASSTRANSFER.2009.09.016.

[9] J. Y. Huang, Y. M. John Chew, and D. Ian Wilson, "A spinning disc study of fouling of cold heat transfer surfaces by gel formation from model food fat solutions," *J. Food Eng.*, vol. 109, no. 1, pp. 49–61, Mar. 2012, doi: 10.1016/J.JFOODENG.2011.09.034.

[10] L. Dong, B. D. Crittenden, and M. Yang, "Fouling Characteristics of Water−CaSO4 Solution under Surface Crystallization and Bulk Precipitation," *Int. J. Heat Mass Transf.*, vol. 180, Dec. 2021, doi: 10.1016/J.IJHEATMASSTRANSFER.2021.121812.

[11] C. Shen, Y. Wang, Z. Tang, Y. Yao, Y. Huang, and X. Wang, "Experimental study on the interaction between particulate fouling and precipitation fouling in the fouling process on heat transfer tubes," *Int. J. Heat Mass Transf.*, vol. 138, pp. 1238–1250, Aug. 2019, doi: 10.1016/J.IJHEATMASSTRANSFER.2019.04.136.

[12] M. Awais and A. A. Bhuiyan, "Recent advancements in impedance of fouling resistance and particulate depositions in heat exchangers," *International Journal of Heat and Mass*

Transfer, vol. 141. 2019, doi: 10.1016/j.ijheatmasstransfer.2019.07.011.

[13] H.-C. Flemming, "Why Microorganisms Live in Biofilms and the Problem of Biofouling," *Mar. Ind. Biofouling*, pp. 3–12, Dec. 2009, doi: 10.1007/978-3-540-69796-1_1.

[14] T. R. Bott, "Industrial Biofouling," *Ind. Biofouling*, pp. 1–5, Jan. 2011, doi: 10.1016/B978-0-444-53224-4.10001-4.

[15] White F.M., Fluid Mechanics, 7th ed. McGraw-Hill Education, 2011.

[16] K. Thulukkanam, Heat Exchanger Design Handbook. 2000.

[17] B. Sundén, "Computational fluid dynamics in research and design of heat exchangers," Heat Transf. Eng., 2007, doi: 10.1080/01457630701421679.

[18] O. Reynolds, "XXIX. An experimental investigation of the circumstances which determine whether the motion of water shall be direct or sinuous, and of the law of resistance in parallel channels," Philos. Trans. R. Soc. London, 1883, doi: 10.1098/rstl.1883.0029.

[19] M. Wosnik, L. Castillo, and W. K. George, "A theory for turbulent pipe and channel flows," *J. Fluid Mech.*, 2000, doi: 10.1017/S0022112000001385.

[20] R. W. Fox and A. T. McDonald, "Introduction to Fluid Mechanics," *Eur. J. Eng. Educ.*, 1994, doi: 10.1080/03043799408928334.

[21] T. R. Bott and M. M. V. P. S. Pinheiro, "Biological fouling — velocity and temperature effects," *The Canadian Journal of Chemical Engineering*. 1977, doi: 10.1002/cjce.5450550420.

[22] "V. Similarity of motion in relation to the surface friction of fluids," *Philos. Trans. R. Soc. London. Ser. A, Contain. Pap. a Math. or Phys. Character*, 1914, doi: 10.1098/rsta.1914.0016.

[23] H. Müller-Steinhagen, "Cooling-Water Fouling in Heat Exchangers," *Adv. Heat Transf.*, 1999, doi: 10.1016/S0065-2717(08)70307-1.

[24] L. D. Chambers, K. R. Stokes, F. C. Walsh, and R. J. K. Wood, "Modern approaches to marine antifouling coatings," *Surf. Coatings Technol.*, vol. 201, no. 6, pp. 3642–3652, Dec. 2006, doi: 10.1016/J.SURFCOAT.2006.08.129.

[25] T. E. Cloete, D. Westaard, and S. J. Van Vuuren, "Dynamic response of biofilm to pipe surface and fluid velocity," *Water Sci. Technol.*, vol. 47, no. 5, pp. 57–59, Mar. 2003, doi: 10.2166/WST.2003.0280.

[26] M. Krsmanovic, D. Biswas, H. Ali, A. Kumar, R. Ghosh, and A. K. Dickerson, "Hydrodynamics and surface properties influence biofilm proliferation," *Adv. Colloid Interface Sci.*, vol. 288, p. 102336, Feb. 2021, doi: 10.1016/J.CIS.2020.102336.

[27] D. Taherzadeh, C. Picioreanu, and H. Horn, "Mass Transfer Enhancement in Moving Biofilm Structures," *Biophys. J.*, vol. 102, no. 7, p. 1483, Apr. 2012, doi:

10.1016/J.BPJ.2012.02.033.

[28] H. A. Videla, “Manual of Biocorrosion,” *Man. Biocorrosion*, Apr. 2018, doi: 10.1201/9780203748190.

[29] L. H. G. Morton, D. L. A. Greenway, C. C. Gaylarde, and S. B. Surman, “Consideration of some implications of the resistance of biofilms to biocides,” *Int. Biodeterior. Biodegradation*, vol. 41, no. 3–4, pp. 247–259, Jan. 1998, doi: 10.1016/S0964-8305(98)00026-2.

[30] M. J. Chen, Z. Zhang, and T. R. Bott, “Effects of operating conditions on the adhesive strength of Pseudomonas fluorescens biofilms in tubes,” *Colloids Surfaces B Biointerfaces*, 2005, doi: 10.1016/j.colsurfb.2005.04.004.

[31] R.N. Nesaratnam, “Biofilm formation and destruction on simulated heat transfer surfaces.” Ph.D. dissertation, University of Birmingham, Birmingham, UK, 1984.

[32] T. R. Bott and P. C. Miller, “Mechanisms of biofilm formation on aluminium tubes,” *J. Chem. Technol. Biotechnol. Biotechnol.*, 2008, doi: 10.1002/jctb.280330307.

[33] P. Stoodley, J. Wefel, A. Gleseke, D. DeBeer, and C. Von Ohle, “Biofilm plaque and hydrodynamic effects on mass transfer, fluoride delivery and caries,” *J. Am. Dent. Assoc.*, 2008, doi: 10.14219/jada.archive.2008.0333.

[34] M. G. Trulear and W. G. Characklis, “Dynamics of Biofilm Processes.” *Journal of Water Pollution Control Federation, pp. 1288-1301*, 1982, Available: https://www.jstor.org/stable/25041684 (accessed Jan. 16, 2023).

[35] J. R. Kim et al., “Porous anodes with helical flow pathways in bioelectrochemical systems: The effects of fluid dynamics and operating regimes,” J. Power Sources, vol. 213, pp. 382–390, Sep. 2012, doi: 10.1016/J.JPOWSOUR.2012.03.040.

[36] M. A. Delavar and J. Wang, “Modeling coupled temperature and transport effects on biofilm growth using thermal lattice Boltzmann model,” AIChE J., vol. 67, no. 4, p. e17122, Apr. 2021, doi: 10.1002/AIC.17122.

[37] C. Hellio and D. M. Yebra, “Introduction,” in *Advances in Marine Antifouling Coatings and Technologies*, 2009.

[38] C. G. Munger, “Corrosion prevention by protective coatings.,” 1984.

[39] L. D. Chambers, K. R. Stokes, F. C. Walsh, and R. J. K. Wood, “Modern approaches to marine antifouling coatings,” 2006, doi: 10.1016/j.surfcoat.2006.08.129.

[40] G. Jones, “The battle against marine biofouling: A historical review,” in *Advances in Marine Antifouling Coatings and Technologies*, 2009.

[41] T. R. Bott, “Industrial Biofouling,” in *Industrial Biofouling*, Elsevier, 2011, pp. 1–5.

[42] C. Hellio and D. M. Yebra, “Introduction,” in *Advances in Marine Antifouling Coatings and Technologies*, Elsevier Ltd, 2009, pp. 1–15.

[43] I. Banerjee, R. C. Pangule, and R. S. Kane, “Antifouling coatings: Recent developments in the design of surfaces that prevent fouling by proteins, bacteria, and marine organisms,” *Advanced Materials*. 2011, doi: 10.1002/adma.201001215.

[44] D. M. Yebra, S. Kiil, K. Dam-Johansen, and C. Weinell, “Reaction rate estimation of controlled-release antifouling paint binders: Rosin-based systems,” *Prog. Org. Coatings*, vol. 53, no. 4, pp. 256–275, Aug. 2005, doi: 10.1016/J.PORGCOAT.2005.03.008.

[45] M. H. Martin and J. O. Nriagu, “Copper in the Environment, Part 1: Ecological Cycling. Part 2: Health Effects.,” *J. Ecol.*, 1981, doi: 10.2307/2259704.

[46] D. M. Yebra, S. Kiil, and K. Dam-Johansen, “Antifouling technology—past, present and future steps towards efficient and environmentally friendly antifouling coatings,” *Prog. Org. Coatings*, vol. 50, no. 2, pp. 75–104, Jul. 2004, doi: 10.1016/J.PORGCOAT.2003.06.001.

[47] W. Höland and G. H. Beall, *Glass-ceramic technology*. 2019.

[48] S. Rossi, F. Deflorian, L. Fontanari, A. Cambruzzi, and P. L. Bonora, “Electrochemical measurements to evaluate the damage due to abrasion on organic protective system,” 2005, doi: 10.1016/j.porgcoat.2004.09.005.

[49] T. J. HEADLEY and R. E. LOEHMAN, “Crystallization of a Glass-Ceramic by Epitaxial Growth,” *J. Am. Ceram. Soc.*, 1984, doi: 10.1111/j.1151-2916.1984.tb19606.x.

[50] J. Shi and X. Feng, “Laser-induced nonlinear crystalline waveguide on glass fiber format and diode-pumped second harmonic generation,” *Opt. Fiber Technol.*, 2018, doi: 10.1016/j.yofte.2018.01.015.

[51] J. Deubener *et al.*, “Updated definition of glass-ceramics,” *J. Non. Cryst. Solids*, 2018, doi: 10.1016/j.jnoncrysol.2018.01.033.

[52] S. Fujita and S. Tanabe, “Fabrication, microstructure and optical properties of Er3+:YAG glass-ceramics,” *Opt. Mater. (Amst).*, 2010, doi: 10.1016/j.optmat.2010.01.014.

[53] M. Kamnoy, U. Intatha, A. Munpakdee, S. Eitssayeam, and T. Tunkasiri, “Mechanical Properties and Microstructure of Li_2O-SiO_2-P_2O_5-Al_2O_3-K_2O-CaO Glass-Ceramics,” *Key Eng. Mater.*, 2018, doi: 10.4028/www.scientific.net/kem.766.164.

[54] İ. Ceylan, “SUSTAINABLE WASTE UTILIZATION IN GLASS-CERAMIC COATING PRODUCTION,” Yıldız Technical University, 2022.

[55] V. Günay and Ş. Yılmaz, *Glass Ceramics: Science and Technology (Cam Seramikler: Bilim ve Teknolojisi)*. Kocaeli, 2010.

[56] L. Samiee, H. Sarpoolaky, and A. Mirhabibi, “Microstructure and adherence of cobalt containing and cobalt free enamels to low carbon steel,” *Mater. Sci. Eng. A*, 2007, doi: 10.1016/j.msea.2006.12.108.

[57] X. Fu, C. H. Zhang, C. Q. Li, K. J. Li, and Y. B. Zuo, “Design and processing of

temperature resistant enamel coating materials," 2014, doi: 10.4028/www.scientific.net/AMM.457-458.168.

[58] N. Çöpoğlu, "DEVELOPMENT OF NANO PARTICLE REINFORCED ABRASION RESISTANT GLASS-CERAMICS," Yıldız Technical University, 2020.

[59] E. Yılmaz, "Taban Malzemeye Emaye Arayüz İlişkilerinin Emaye Kalitesine Etkisi," İstanbul Teknik Üniversitesi, 2014.

[60] E. Güngör, "Termik Santrallerin Döner Tip Hava Isıtıcılarında Kullanılan Isı Değiştirici Plakalar İçin Emaye Kaplama Optimizasyonu," İstanbul Teknik Üniversitesi, 2015.

[61] F. Russo, S. Rossi, and A. M. Compagnoni, "Porcelain Enamel Coatings," *Encyclopedia*, 2021, doi: 10.3390/encyclopedia1020032.

[62] B. Karasu, İ. Saçkan, and M. C. Tapli, "Enamel from past to present time," *El-Cezeri J. Sci. Eng.*, 2020, doi: 10.31202/ecjse.660254.

[63] W. D. Andrews, Andrew Irving and Pagliuca, Silvano and Faust, *Porcelain (vitreous) Enamels and Industrial Enamelling Processes: The Preparation, Application and Properties of Enamels*. Tipografia commerciale Mantova, Italy, 2011.

[64] R. A. Eppler and E. D., *Glazes and glass coatings*. Ohio: The American Ceramic Society, Ohio, 2000.

[65] W. D. Faust, *Porcelain (Vitreous) Enamels and Industrial Enamelling Processes*. Ohio, 2012.

[66] K. Karaman, Y. Bozkurt Yılmaz, T. Cengiz, B. Çiçek, S. Yazar, and C. Author, "Examination of Enamel Different CaO-P2O5 Sources-Karaman at al. SERAMİK Examination of Vitreous Enamel Coating Properties Prepared from Different CaO-P2O5 Raw Material Sources," *Seramik-Journal Turkish Ceram. Soc.*, vol. 1, no. 3, pp. 19–25, 2021, Accessed: Jan. 30, 2023. [Online]. Available: https://orcid.org/0000-0001-8195-4153.

[67] A. A. Andrews, S. Pagliuce, and W. D. Faust, "Porcelain Enamels: The Preparation, Application and Properties of Enamels," no. Raw Materials for Enamels, 2011.

[68] K. Benzeşik, M. İpekçi, A. Yeşilçubuk, F.Ç. Şahin, O. Yücel, "Optimizing the Migration Behavior of Enamel Coatings Used as Food Contact Materials.", IMMC 2018, 19th International Metallurgy & Materials Congress, page: 437-440. Available: https://www.researchgate.net/profile/Meltem-Ipekci-Terzioglu/publication/329327438_Optimizing_the_Migration_Behavior_of_Enamel_Coatings_Used_as_Food_Contact_Materials/links/5c3ec29492851c22a37869d3/Optimizing-the-Migration-Behavior-of-Enamel-Coatings-Used-as-Food-Contact-Materials.pdf

[69] A. P. Tomsia and J. A. Pask, "Chemical reactions and adherence at glass/metal interfaces: an analysis," Dent. Mater., 1986, doi: 10.1016/S0109-5641(86)80063-X.

[70] A. I. Andrews, P. S., and W. D. Faust, Fundamentals and Cosiderations, Porcelain

(Vitreous) Enamels and Industrial Enamelling Processes The Preparation, Application and Properties of Enamels. Mantova, 2011.

[71] A. I. Andrews, S. Pagliuca, and W. D. Faust, Enamel Properties and Tests, Porcelain (Vitreous) Enamels and Industrial Enamelling Processes The Preparation, Application and Properties of Enamels. Mantova, 2011.

[72] Standard Test Method for Thermal Shock Resistance of Porcelain-Enameled Utensils, ASTM C385-58, 2018.

[73] M. Garcia-Valles et al., "Calculation of viscosity-temperature curves for glass obtained from four wastewater treatment plants in Egypt," J. Therm. Anal. Calorim., 2013, doi: 10.1007/s10973-012-2232-7.

[74] A. I. Andrews, S. Pagliuca, and W. D. Faust, "Chemical and Electrical Properties," in Porcelain (Vitreous) Enamels and Industrial Enamelling Processes The Preparation, Application and Properties of Enamels, Montava, 2011.

[75] M. Shu, H. Yin, Q. Zhong, X. Shi, and H. Han, "Effect of glass powder on acid resistance of enamel coating," Surf. Rev. Lett., 2017, doi: 10.1142/S0218625X17500366.

[76] P. W. McMillan, "The crystallisation of glasses," J. Non. Cryst. Solids, 1982, doi: 10.1016/0022-3093(82)90281-2.

[77] E. Scrinzi and S. Rossi, "The aesthetic and functional properties of enamel coatings on steel," Mater. Des., 2010, doi: 10.1016/j.matdes.2010.04.030.

[78] S. Baycık, "Granüle Yüksek Fırın Cüruflarının Karo Sektöründe Kullanılabilirliğinin Araştırılması," İstanbul Technical University, 2003

[79] Enamelled Steel: A traditional material for modern living, Arcelor Mittal, 2015. Available: https://industry.arcelormittal.com/flipbook/fce/Brochures/Enamelledsteel_brochure_EN/#page/4

[80] A. Davran, "Enamelling Applications On Metal From Past to Future," İzmir University, 2011.

[81] L. Besra and M. Liu, "A review on fundamentals and applications of electrophoretic deposition (EPD)," Progress in Materials Science. 2007, doi: 10.1016/j.pmatsci.2006.07.001.

[82] P. Amrollahi, J. S. Krasinski, R. Vaidyanathan, L. Tayebi, and D. Vashaee, "Electrophoretic Deposition (EPD): Fundamentals and Applications from Nano- to Micro-Scale Structures," in Handbook of Nanoelectrochemistry, 2015.

[83] M. R. Dorfman, "Thermal spray coatings," in Handbook of Environmental Degradation Of Materials: Third Edition, 2018.

[84] P. Fauchais and A. Vardelle, "Thermal Sprayed Coatings Used Against Corrosion and Corrosive Wear," in Advanced Plasma Spray Applications, 2012.

[85] T. Zhang, Y. Bao, and D. T. Gawne, “Process model of plasma enamelling,” J. Eur. Ceram. Soc., 2003, doi: 10.1016/S0955-2219(02)00235-2.

[86] O. V. Shalygina, L. L. Bragina, G. I. Mironova, and A. P. Odintsova, “Single-Frit Nickel-Free Glass-Enamel Coatings Obtained by the Poesta Technology,” Glas. Ceram. (English Transl. Steklo i Keramika), 2014, doi: 10.1007/s10717-014-9656-4.

[87] B. Daehne, B. T. Wattermen, and C. Fürle, “LimnoMar’s RotoMarin® - a new opportunity for dynamic field testing. 18th International Congress on Marine Corrosinon and Fouling ICMCF.,” 2016.

[88] K. Gall, C. Fürle, and Watermann, “Increased settlement rates of field caught barnacle larvae in settlement assays adding metamorphosed juveniles. 18th International Congress on Marine Corrosion ans Fouling ICMCF,” 2016.

[89] Y. Tian, W. Liu, and S. Sun, “Effect of TiO2/Na2O on the crystallisation behaviour of SiO2-Al2O3-B2O3-P2O5 glass-ceramics,” Glas. Technol. Eur. J. Glas. Sci. Technol. Part A, 2016, doi: 10.13036/1753-3546.56.6.191.

[90] H. Zhao, C. Peng, M. Wu, M. Lv, and J. Wu, “A crystallization method for preparation of anatase-based glass-ceramic glaze,” J. Eur. Ceram. Soc., 2019, doi: 10.1016/j.jeurceramsoc.2018.11.027.

[91] I. K. Abdulrahman, I. A. Mahmood, and A. S. Jabor, “Effects of heat treatment, quartz additions and particle size on the properties of enamel with low-alloy steel substrate,” 2020, doi: 10.1088/1757-899X/671/1/012136.

[92] S. Rossi, F. Russo, and M. Calovi, “Durability of vitreous enamel coatings and their resistance to abrasion, chemicals, and corrosion: a review,” Journal of Coatings Technology and Research. 2021, doi: 10.1007/s11998-020-00415-3.

[93] A. V. DeCeanne, L. R. Rodrigues, C. J. Wilkinson, J. C. Mauro, and E. D. Zanotto, “Examining the role of nucleating agents within glass-ceramic systems,” J. Non. Cryst. Solids, vol. 591, p. 121714, Sep. 2022, doi: 10.1016/J.JNONCRYSOL.2022.121714.

[94] O. R. K. Montedo, F. J. Floriano, J. de Oliveira Filho, E. Angoletto, and A. M. Bernardin, “Sintering behavior of LZSA glass-ceramics,” Mater. Res., 2009, doi: 10.1590/S1516-14392009000200014.

[95] C. Venturelli, “Heating Microscopy and its Applications,” Micros. Today, 2011, doi: 10.1017/s1551929510001185.

[96] S. Rossi et al., “Microstructural Analysis and Surface Modification of a Vitreous Enamel Modified with Corundum Particles,” Adv. Eng. Mater., 2019, doi: 10.1002/adem.201900231.

[97] S. Rossi, N. Parziani, and C. Zanella, “Abrasion resistance of vitreous enamel coatings in function of frit composition and particles presence,” Wear, vol. 332–333, pp. 702–709, May 2015, doi: 10.1016/J.WEAR.2015.01.058.

[98] A. Tunali, E. Ozel, and S. Turan, “Production and characterisation of granulated frit to achieve anorthite based glass-ceramic glaze,” J. Eur. Ceram. Soc., 2015, doi: 10.1016/j.jeurceramsoc.2014.09.039.

[99] K. Hrabovská, J. Podjuklová, K. Barčová, L. Dobrovodská, and K. Pelikánová, “Vitreous enamel coating on steel substrates,” 2009, doi: 10.4028/www.scientific.net/SSP.147-149.856.

[100] Ö. Işiksaçan, A. Yeşilçubuk, and O. Yücel, “Substrate-Enamel Interface Relation and Impact on Quality of Enamel,” in TMS 2015 144th Annual Meeting & Exhibition, 2015.

[101] M. Hunkel, H. Surm, and M. Steinbacher, “Dilatometry,” in Handbook of Thermal Analysis and Calorimetry, 2018.

[102] M. G. Rasteiro, T. Gassman, R. Santos, and E. Antunes, “Crystalline phase characterization of glass-ceramic glazes,” Ceram. Int., 2007, doi: 10.1016/j.ceramint.2005.10.002.

[103] M. S. H. Akash and K. Rehman, “Thermo Gravimetric Analysis,” in Essentials of Pharmaceutical Analysis, 2020.

[104] M. J. Vold, “Differential thermal analysis,” Anal. Chem., 1949, doi: 10.1021/ac60030a011.

[105] A. Marotta, A. Buri, and F. Branda, “Nucleation in glass and differential thermal analysis,” J. Mater. Sci., 1981, doi: 10.1007/BF00738622.

[106] A. H. Dietzel, Emaillierung: Wissenschaftliche Grundlagen und Grundzüge der Technologie, Scientific principles and fundamentals of technology. Berlin, 1981.

[107] B. W. King, H. P. Tripp, and D. W.H., Nature of Adherence of Porcelain Enamels to Metals. 1959.

[108] S. Rossi, C. Zanella, and R. Sommerhuber, “Influence of mill additives on vitreous enamel properties,” Mater. Des., 2014, doi: 10.1016/j.matdes.2013.10.059.

[109] M. Bodaghi and A. Davarpanah, “The influence of cobalt on the microstructure and adherence characteristics of enamel on steel sheet,” Process. Appl. Ceram., 2011, doi: 10.2298/pac1104215b.

[110] B. K. Sun and T. J. O’Keefe, “Growth of electrolytic copper dendrites and their adhesion to an epoxy resin,” Surf. Coatings Technol., 1998, doi: 10.1016/S0257-8972(98)00488-5.

[111] A. W. Y. Tan et al., “Microstructure, mechanical and tribological properties of cold sprayed Ti6Al4V–CoCr composite coatings,” Compos. Part B Eng., 2020, doi: 10.1016/j.compositesb.2020.108280.

[112] J. G. Li, T. Ishigaki, and X. Sun, “Anatase, brookite, and rutile nanocrystals via redox reactions under mild hydrothermal conditions: Phase-selective synthesis and physicochemical properties,” J. Phys. Chem. C, 2007, doi: 10.1021/jp0673258.

[113] D. T. Cromer and K. Herrington, “The Structures of Anatase and Rutile,” J. Am. Chem. Soc., 1955, doi: 10.1021/ja01623a004.

[114] W. H. Baur, “ Atomabstände und Bindungswinkel im Brookit, TiO 2 ,” Acta Crystallogr., 1961, doi: 10.1107/s0365110x61000747.

[115] F. Scarpelli, T. F. Mastropietro, T. Poerio, and N. Godbert, “Mesoporous TiO2 Thin Films: State of the Art,” in Titanium Dioxide - Material for a Sustainable Environment, 2018.

[116] X. Chen and S. S. Mao, “Titanium dioxide nanomaterials: Synthesis, properties, modifications and applications,” Chemical Reviews. 2007, doi: 10.1021/cr0500535.

[117] S. Dong et al., “Recent developments in heterogeneous photocatalytic water treatment using visible light-responsive photocatalysts: A review,” RSC Advances. 2015, doi: 10.1039/c4ra13734e.

[118] T. Ohno, M. Akiyoshi, T. Umebayashi, K. Asai, T. Mitsui, and M. Matsumura, “Preparation of S-doped TiO2 photocatalysts and their photocatalytic activities under visible light,” Appl. Catal. A Gen., 2004, doi: 10.1016/j.apcata.2004.01.007.

[119] P. Pichat, J. Disdier, C. Hoang-Van, D. Mas, G. Goutailler, and C. Gaysse, “Purification/deodorization of indoor air and gaseous effluents by TiO2 photocatalysis,” Catal. Today, 2000, doi: 10.1016/S0920-5861(00)00480-6.

[120] M. Ni, M. K. H. Leung, D. Y. C. Leung, and K. Sumathy, “A review and recent developments in photocatalytic water-splitting using TiO2 for hydrogen production,” Renewable and Sustainable Energy Reviews. 2007, doi: 10.1016/j.rser.2005.01.009.

[121] K. Zhu, N. R. Neale, A. Miedaner, and A. J. Frank, “Enhanced charge-collection efficiencies and light scattering in dye-sensitized solar cells using oriented TiO2 nanotubes arrays,” Nano Lett., 2007, doi: 10.1021/nl062000o.

[122] J. H. Shim, I. T. Bae, and J. Cho, “Microstructure development of hydrothermally grown TiO2 thin films with vertically aligned nanorods,” J. Am. Ceram. Soc., 2018, doi: 10.1111/jace.15110.

[123] D. P. Mukherjee and S. K. Das, “SiO 2-Al 2O 3-CaO glass-ceramics: Effects of CaF 2 on crystallization, microstructure and properties,” Ceram. Int., 2013, doi: 10.1016/j.ceramint.2012.06.066.

[124] R. C. Ropp, “Group 17 (H, F, Cl, Br, I) Alkaline Earth Compounds,” in Encyclopedia of the Alkaline Earth Compounds, 2013.

[125] D. U. Tulyaganov, S. Agathopoulos, J. M. Ventura, M. A. Karakassides, O. Fabrichnaya, and J. M. F. Ferreira, “Synthesis of glass-ceramics in the CaO-MgO-SiO2 system with B2O3, P2O5, Na2O and CaF2 additives,” J. Eur. Ceram. Soc., 2006, doi: 10.1016/j.jeurceramsoc.2005.02.009.

[126] T. B. Reed, “Free Energy of Formation of Binary Compounds” The MIT Press,March

15,1972, ISBN: 9780262180511.

[127] D. R. Gaskell, D. E. Laughlin “Introduction to the Thermodynamics of Materials”6th Edition, CRC Press , 2017, ISBN: 1498757030

[128] Y. Xiang, J. Du, M. M. Smedskjaer, and J. C. Mauro, “Structure and properties of sodium aluminosilicate glasses from molecular dynamics simulations,” J. Chem. Phys., vol. 139, no. 4, p. 044507, Jul. 2013, doi: 10.1063/1.4816378.

[129] A. S. Tomar et al., “Progress in fabrication and manufacturing of sodium aluminosilicate materials (geopolymers) as protective coating materials: A review,” J. Polym. Res., vol. 29, no. 6, pp. 1–18, Jun. 2022, doi: 10.1007/S10965-022-03078-3/TABLES/1.

[130] D. M. Zirl and S. H. Garofalini, “Structure of Sodium Aluminosilicate Glasses,” J. Am. Ceram. Soc., vol. 73, no. 10, pp. 2848–2856, Oct. 1990, doi: 10.1111/J.1151-2916.1990.TB06685.X.

[131] T. K. Bechgaard et al., “Structure and mechanical properties of compressed sodium aluminosilicate glasses: Role of non-bridging oxygens,” J. Non. Cryst. Solids, 2016, doi: 10.1016/j.jnoncrysol.2016.03.011.

[132] D. M. Zirl and S. H. Garofalini, “Structure of Sodium Aluminosilicate Glasses,” J. Am. Ceram. Soc., 1990, doi: 10.1111/j.1151-2916.1990.tb06685.x.

[133] H. Peng, D. Seneviratne, and J. Vaughan, “Role of the Amorphous Phase during Sodium Aluminosilicate Precipitation,” Ind. Eng. Chem. Res., 2018, doi: 10.1021/acs.iecr.7b04538.

[134] E. M. A. Khalil, M. Aouf, “Effect of heat treatment on the infrared absorption spectra of stronium-sodium-borosilicate glass” Indian Journal of Engineering and Materials Sciences, India, p. 155-162, 1997.

[135] J. H. Shin et al., “Fabrication of silica nanostructures with a microwave assisted direct patterning process,” Nanotechnology, vol. 25, no. 22, p. 225301, 2014, doi: 10.1088/0957-4484/25/22/225301.

[136] T. Moskalewicz, F. Smeacetto, G. Cempura, L. C. Ajitdoss, M. Salvo, and A. Czyrska-Filemonowicz, “Microstructure and properties characterisation of the double layered glass-ceramic coating on near-α titanium alloy,” Surf. Coatings Technol., 2010, doi: 10.1016/j.surfcoat.2010.04.008.

[137] L. Stoch and M. Środa, “Infrared spectroscopy in the investigation of oxide glasses structure,” 1999, doi: 10.1016/S0022-2860(99)00146-5.

[138] C. Khee Chung Hui, N. Dhanapalan, A. Cahya Khayrani, T. Imanto, N. Soraya Sambudi, and K. Chung Hui, “The synthesis of amino-functionalized carbon quantum dots-decorated hydroxyapatite as drug delivery agent,” Comptes Rendus. Chim., vol. 25, no. G1, pp. 295–306, Oct. 2022, doi: 10.5802/CRCHIM.206.

[139] “Non-magnetic coatings on magnetic substrates — Measurement of coating thickness

— Magnetic method.”, ISO 2178:2016, 2016. ISBN: 978 0 580 82783 9

[140] “Cold rolled low carbon steel flat products for vitreous enameling. Technical delivery conditions.”, EN 10209:2013, 2013. Available: https://standards.iteh.ai/catalog/standards/cen/0b7889d5-6b60-43ff-be01-b7eb2a3e0d26/en-10209-2013

[141] “Vitreous and porcelain enamels — Determination of resistance to chemical corrosion — Part 2: Determination of resistance to chemical corrosion by boiling acids, boiling neutral liquids, alkaline liquids and/or their vapours”, ISO 28706-2:2017, 2017. Available: https://www.iso.org/standard/63869.html

[142] “Textiles — Tests for colour fastness — Part J03: Calculation of colour differences.”, ISO 105-J03:2009, 2019. Available: https://www.iso.org/standard/51385.html

[143] “Paints and varnishes. Determination of gloss value at 20 degrees, 60 degrees and 85 degrees.”, ISO 2813: 2014, 2014 (reviewed and confirmed in 2019.). Available: https://www.iso.org/standard/56807.html

[144] F. Wan, Q. Ye, and F. Zhou, “Antifouling of micro-/nanostructural surfaces,” Antifouling Surfaces Mater., pp. 83–103, Jan. 2015, doi: 10.1007/978-3-662-45204-2_4/FIGURES/13.

[145] R. Basheer, G. Ganga, R. K. Chandran, G. M. Nair, M. B. Nair, and S. M. A. Shibli, “Effect of W-TiO2 composite to control microbiologically influenced corrosion on galvanized steel,” Appl. Microbiol. Biotechnol., 2013, doi: 10.1007/s00253-012-4389-1.

[146] C. A. Damon et al., “The performance of hybrid titania/silica-derived xerogels as active antifouling/fouling-release surfaces against the marine alga Ulva linza: in situ generation of hypohalous acids,” Biofouling, 2016, doi: 10.1080/08927014.2016.1203420.

[147] D. Zhao, Y. Lu, Z. Wang, X. Zeng, S. Liu, and T. Wang, “Antifouling properties of micro arc oxidation coatings containing Cu2O/ZnO nanoparticles on Ti6Al4V,” Int. J. Refract. Met. Hard Mater., 2016, doi: 10.1016/j.ijrmhm.2015.10.003.

[148] B. Xia, B. Chen, X. Sun, K. Qu, F. Ma, and M. Du, “Interaction of TiO2 nanoparticles with the marine microalga Nitzschia closterium: Growth inhibition, oxidative stress and internalization,” Sci. Total Environ., 2015, doi: 10.1016/j.scitotenv.2014.11.066.

[149] J. Ji, Z. Long, and D. Lin, “Toxicity of oxide nanoparticles to the green algae Chlorella sp.,” Chem. Eng. J., 2011, doi: 10.1016/j.cej.2010.11.026.

[150] X. Zhu, J. Zhou, and Z. Cai, “TiO2 nanoparticles in the marine environment: Impact on the toxicity of tributyltin to abalone (Haliotis diversicolor supertexta) embryos,” Environ. Sci. Technol., 2011, doi: 10.1021/es103779h.

[151] M. C. M. van Loosdrecht, J. Lyklema, W. Norde, and A. J. B. Zehnder, “Bacterial adhesion: A physicochemical approach,” Microb. Ecol., 1989, doi: 10.1007/BF02025589.

[152] R. Bos, H. C. van der Mei, and H. J. Busscher, “Physico-chemistry of initial microbial adhesive interactions – its mechanisms and methods for study,” FEMS Microbiol. Rev., 1999, doi: 10.1111/j.1574-6976.1999.tb00396.x.

[153] B. Li and B. E. Logan, “Bacterial adhesion to glass and metal-oxide surfaces,” Colloids Surfaces B Biointerfaces, 2004, doi: 10.1016/j.colsurfb.2004.05.006.

[154] D. R. Absolom, F. V. Lamberti, Z. Policova, W. Zingg, C. J. van Oss, and A. W. Neumann, “Surface thermodynamics of bacterial adhesion,” Appl. Environ. Microbiol., 1983, doi: 10.1128/aem.46.1.90-97.1983.

[155] C. J. Van Oss, R. J. Good, and M. K. Chaudhury, “The role of van der Waals forces and hydrogen bonds in ‘hydrophobic interactions’ between biopolymers and low energy surfaces,” J. Colloid Interface Sci., 1986, doi: 10.1016/0021-9797(86)90041-X.

[156] I. Pignatelli, A. Kumar, M. Bauchy, and G. Sant, “Topological control on silicates’ dissolution kinetics,” Langmuir, 2016, doi: 10.1021/acs.langmuir.6b00359.

[157] G. O’Toole, B. Kaplan, and R. Kolter, “Biofilm formation as microbial development.” Annual Review of Microbiology, vol. 54, p. 49-79, 2000. Doi: 10.1146/annurev.micro.54.1.49.

[158] E. S. Gloag, S. Fabbri, D. J. Wozniak, and P. Stoodley, “Biofilm mechanics: Implications in infection and survival,” Biofilm. 2020, doi: 10.1016/j.bioflm.2019.100017.

[159] H. H. Tuson and D. B. Weibel, “Bacteria-surface interactions,” Soft Matter. 2013, doi: 10.1039/c3sm27705d.

[160] T. R. Garrett, M. Bhakoo, and Z. Zhang, “Bacterial adhesion and biofilms on surfaces,” Progress in Natural Science. 2008, doi: 10.1016/j.pnsc.2008.04.001.

[161] J. Yan, C. D. Nadell, H. A. Stone, N. S. Wingreen, and B. L. Bassler, “Extracellular-matrix-mediated osmotic pressure drives Vibrio cholerae biofilm expansion and cheater exclusion,” Nat. Commun., 2017, doi: 10.1038/s41467-017-00401-1.

[162] B. W. Peterson et al., “Viscoelasticity of biofilms and their recalcitrance to mechanical and chemical challenges,” FEMS Microbiology Reviews. 2015, doi: 10.1093/femsre/fuu008.

[163] L. Samiee, H. Sarpoolaky, and A. Mirhabibi, “Influence of bubble structure on adherence and chemical durability of porcelain enamel,” http://dx.doi.org/10.1179/174367607X202654, vol. 107, no. 1, pp. 27–33, Feb. 2013, doi: 10.1179/174367607X202654.

PUBLICATIONS FROM THE THESIS

Conference Papers

1. Daloğlu S., Çöpoğlu N., Kaya M., Cengiz T., Çiçek B. (2021) Investigation Of Antifouling Properties of Borosilicate, Anatase-Based, and Alkali Borosilicate Glass-Ceramic Systems for Water Contact Applications. V. International Ceramic, Glass, Enamel, Glaze and Paint Congress (SERES'21), Eskisehir, Türkiye, 13 - 15 October 2021, pp. 40.

2. Daloğlu S., Kaya M., Cengiz T., Çiçek B. (2021) Development of Steam-Resistant Glass Ceramic Coatings for Self-Cleaning Ovens. 14th ECerS Conference for Young Scientists in Ceramics, CYSC-2021, Novi Sad, Serbia, October 20-23, 2021 pp. 134.